Assessing Structural Integrity of Concrete Half-joints Using Sensor Data

A Case Study of the Naardertrekvaart Bridge

Amco de Jong

Delft University of Technology

TU Delft

Assessing Structural Integrity of Concrete Half-joints Using Sensor Data

A Case Study of the Naardertrekvaart Bridge

by

Amco de Jong

to obtain the degree of Master of Science
at the Delft University of Technology,
to be defended publicly on Friday October 4, 2024 at 15:45 AM.

Student number:	4942094	
Project duration:	February 12, 2024 – October 4, 2024	
Chair:	Dr. ir. Y. Yang,	TU Delft
Supervisors:	Dr. I.B.C.M. Rocha,	TU Delft
	Dr. ir. S.A.A.M. Fennis,	Rijkswaterstaat
	Ing. A. Gorter,	CT deBoer
	Ing. G.E. Knoppers	Somni Solutions
	Dr. ir. M. Poliotti,	Witteveen+Bos

Cover: Street view of a support of the Naardertrekvaart bridge with sensors (Google Maps)

TU Delft Rijkswaterstaat deBoer Civiele technieken deBoer bv Somni

Preface

This master thesis presents research on the assessment of the structural integrity of concrete half-joints using sensor data. The journey of completing this work has been both challenging and rewarding, and it would not have been possible without the guidance and support of several individuals and organisations.

First and foremost, I would like to express my gratitude to my supervisors at TU Delft for their invaluable expertise and occasional encouragement throughout this process. Their insights and feedback have been critical in shaping the direction and quality of this research.

I am also grateful of the support from Rijkswaterstaat, CT deBoer, and Somni. Their assistance and provision of data and resources were essential for the successful completion of this project. They have given me the exciting opportunity to visit and inspect the half-joints of the bridge myself, and also pay a visit to the traffic control centre to monitor traffic during high-frequency data acquisition.

Additionally, I would like to thank my study mates, who provided not only constructive advice but also a listening ear during the more difficult moments. Their companionship during my thesis has strengthened our friendship, which I hope to continue for many years to come.

This work stands as a testament to the collective effort of all those who contributed along the way, and I am sincerely grateful for their support.

Amco de Jong
Delft, September 2024

Abstract

Bridges are instrumented with joints to facilitate free thermal expansion of separate structural elements and prevent development of internal stresses due to differential settlements of the supports. In the past, mostly between the years 1960 and 1970, joints were frequently designed as half-joints, which were easy to construct and automatically maintained a level-running surface on the bridge. Additionally, half-joints can be implemented outside of the supports, which minimises the magnitude of the sagging bending moment caused by traffic loads. However, half-joints quickly started displaying signs of degradation, caused by development of a crack in one of the re-entrant corners in combination with water leakage into the joint. This crack, often buried deep inside the joint, is difficult to inspect, causing the exact state of the half-joints to often remain unknown. Another way of assessing the structural integrity of the half-joints of a bridge, is to monitor it using a structural health monitoring (SHM) system.

In this research, the measurement data of the SHM system on the Naardertrekvaart bridge is used to to evaluate its current state and serve as an early warning system for detecting damage. The SHM system, which has been collecting measurement data since 2022, includes inclinometers, displacement sensors, and temperature sensors. The research consists of an extensive data analysis procedure on two datasets of the SHM system. The first dataset contains two years of measurement data, obtained at a low measurement frequency. The second dataset contains one day of high-frequency measurement data. Next, the structural integrity of the half-joints is inferred from the measurement data using multiple custom-built FEM models in combination with manual calculations. Based on the outcome of this research, recommendations are provided on SHM systems on other half-joint bridges and improvements of the SHM system of the Naardertrekvaart bridge are proposed.

Analysis of the deformation of the bridge revealed a distinct dependence on seasonal temperature changes, presumably caused by hindered thermal contraction of the half-joints. Analysis of high-frequency measurement data showed that traffic loads significantly affect bridge deformation, with a substantial portion of rotations occurring from the support platforms' movement. Differences in rotational behaviour can be observed along the width of the bridge and a stiffness parameter is used to identify potential damage. A significant variation in stiffness can be observed at specific support locations, particularly on the east and west sides of support 6. The study highlights difficulties in using the SHM system to determine the bridge's state, suggesting improvements such as understanding traffic load magnitudes, modelling damage effects, and increasing measurement frequency. These adaptations may require cloud storage solutions. Oscillatory measurement approaches on half-joint bridges can reduce thermal influence sensitivity, mitigate the need for development of a digital twin, and enable broader monitoring with fewer sensors.

Contents

Abbreviations

Abbreviation	Definition
DAF	Dynamic Amplification Factor
EPS	Expanded Polystyrene
FEM	Finite Element Method
HSC	High Strength Concrete
PSD	Power Spectral Density
SHM	Structural Health Monitoring
WIM	Weigh-in-Motion

1

Introduction

1.1. Research Context

The Naardertrekvaart bridge is a bridge on the A1 highway, located near Naarden. As visible in Figure 1.1, the A1 forms an important link in the transportation network of the Netherlands, connecting Amsterdam to Enschede, through Amersfoort, Apeldoorn and Deventer [1]. The Naardertrekvaart bridge was constructed in 1969 and uses spans consisting of longitudinal girders with a compression layer, which are connected to the supports using half-joints.

Figure 1.1: A1 highway, with the location of the Naardertrekvaart bridge [1]

The half-joint was first introduced by Heinrich Gottfried Gerber, a German engineer, which is why it is regularly referred to as a Gerber saddle or a Gerber joint [2, 3]. This type of joint uses a nib on the abutments to support the nib of the spanning beams. A schematisation of a half-joint in a bridge can be seen in Figure 1.2. The application of half-joints in bridges gained a lot of popularity, mainly in Italy, because of several advantages [4]. Firstly, a half-joint forms a hinge connection between the support and the bridge deck. Implementation of a hinge into the structure prevents the development of internal stresses resulting from differential settlement of the supports [4]. Also, the implementation of a hinge reduces the size of the structural elements, benefiting prefabrication of longitudinal members, which helps to improve their quality while reducing construction costs and time [5, 6]. Secondly, the use of half-joints automatically causes a level-running surface on top of the bridge [2, 6]. Between 1960 and 1990, the half-joint construction system was applied in many bridges in Europe [3, 6]. Currently, over 100 of the bridges in possession of Rijkswaterstaat contain half-joints.

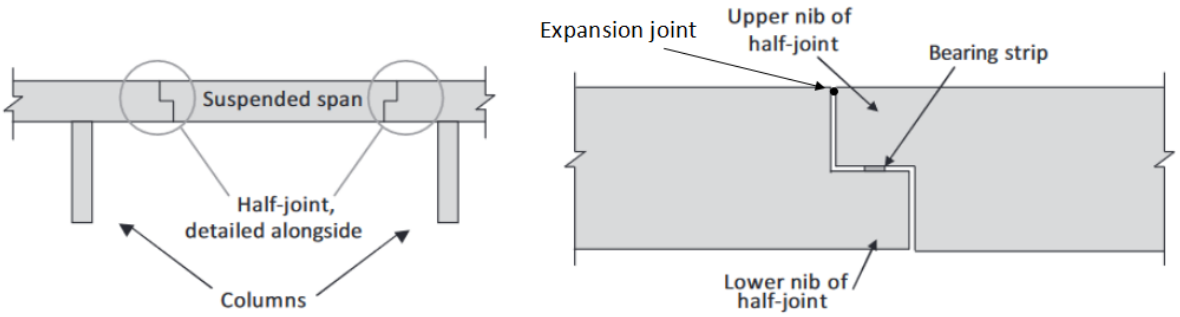

Figure 1.2: Half-joint principle for reinforced concrete bridges, edited [6]

In the first years of construction of half-joint bridges, engineers had no code provisions to rely on. As a result, the reinforcement near half-joints was generally detailed similarly to corbels, despite significant differences in load transfer mechanism, as visible in Figure 1.3. The first investigations on the reinforcement detailing of half-joints in literature indicating these differences and showing the importance of proper reinforcement detailing, date back to the 1970s [7, 8, 9, 10]. These studies mainly indicated the importance of sufficient anchorage of the longitudinal reinforcement and the need for sufficient hanger reinforcement (Figure 1.4b) [6]. Research also showed the effectiveness of the application of diagonal reinforcement bars close to the re-entrant corner (Figure 1.4a) in reducing crack width opening [6]. Although the effectiveness of these types of reinforcement were only documented in literature after 1970, multiple examples of half-joint bridges from before 1970 can be found where hanger reinforcement and diagonal reinforcement was applied [11, 12], indicating that the importance of proper reinforcement detailing in half-joints was already recognised. Nevertheless, the provided reinforcement in half-joints often turned out to be insufficient. Research performed after 2000 even showed that the reinforcement detailing prescribed by NEN 6720 until 2004 in the Netherlands provided insufficient resistance [13, 14, 15, 16].

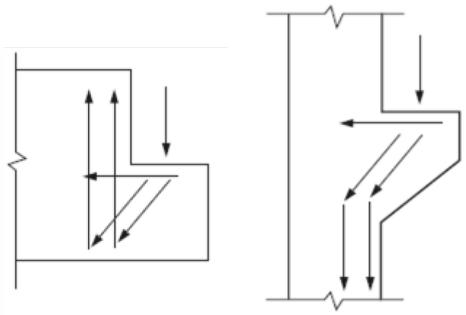

Figure 1.3: Load transfer in a (a) half-joint and a (b) corbel [17]

As a result of insufficient reinforcement detailing, crack widths at the location of the re-entrant corner of the half-joins exceed their design value, causing the reinforcement to be more prone to corrosion. In addition, the expansion joints, installed at the top of the connection to prevent leakage of fluids into the half-joints, as visible in Figure 1.2, often showed premature breakage. As a result of this, seepage of rainwater stimulated corrosion of concrete reinforcement even more, mainly at the lower nib of the half-joint.

The phenomena mentioned above caused many bridges to show signs of premature degradation. [18, 19]. However, the exact level of degradation of the half-joint often remained unknown, as the inside of the joint is difficult to inspect and maintain due to its shape. As a result of this lack of maintainability, several collapses of half-joint bridges have occurred, causing multiple casualties [11, 12].

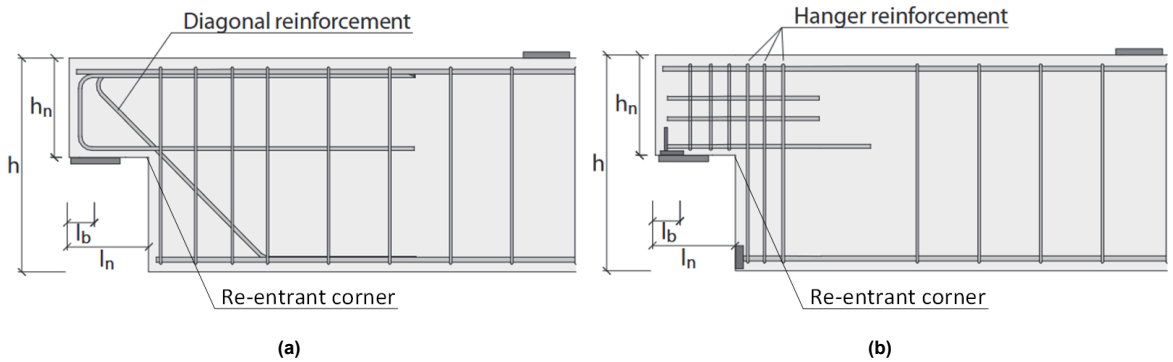

Figure 1.4: Different reinforcement layout approaches for the design of half-joints, edited [6]

In the case of the Naardertrekvaart bridge, damage as a result of water leakage in the joint was first observed in 1988. From this point on, multiple inspections and repairs have been performed on the half-joints of the bridge. However, as the spaces in the half-joints are difficult to inspect, there is a lot of uncertainty about the condition of the concrete and its reinforcement at the location of the joints. To gain more insight into the structural integrity of the half-joints, in 2021 several types of sensors were placed at different locations on two of the supports of the bridge. The goal of placing these sensors was two-fold. Firstly, sensor observations would serve to detect the occurrence of failure mechanisms right at the time of occurrence. Secondly, as more and more half-joint bridges are at the end of their life time, findings from the analysis of the sensor data would be used to determine the optimal placement of sensors on other bridges in the future.

1.2. Research Problem

The monitoring data of the Naardertrekvaart bridge that has been gathered between 2022 and 2024 shows some unexpected behaviour. Many speculations have arisen from multiple stakeholders to explain the periodic influences and fluctuations, but these speculations can not be confirmed by solely inspecting the measurement data. Additionally, there is uncertainty of the measurement system's ability to detect occurring damage. The early warning system that is active at this moment is mostly data-based, and uses limited knowledge of the behaviour of the bridge. As a result, this system is not suspected to function optimally. Therefore, the measurement data of the bridge is in need of interpretation by means of a digital twin. Additional insight into the behaviour of the Naardertrekvaart bridge can not only boost the effectiveness of its own early warning system, but can also assist the design of similar systems on other half-joint bridges.

Multiple examples of structural health monitoring systems on half-joint bridges can be found in literature. Only some of the researches explain to some extent how the measurement data from the SHM setup is used to develop an early warning system that detects signs of structural degradation. These researches can be found in Table 1.1. Of these researches, only one describes a complete approach on the use of measurement data to establish an early warning system, and contains an extensively documented investigation of the structural mechanisms that occur in half-joint bridges due to different influences in combination with traffic loads. The limited amount of studies in the field of SHM systems on half-joint systems in combination with an early warning system reveals a clear research gap.

Table 1.1: Research Gap Table

Ref	Bridge name/ location	Structure type	Measured variables	Sensor locations	Data analysis approach	Main conclusions
[20]	Three-span highway bridge in Australia	Concrete girder bridge, central span supported on half-joints	Strain, acceleration, video	Strain gauges at bottom of flanges of longitudinal girders in the middle of the central span. Strain gauges on the vertical strengthening tie rods. Accelerometers at the bottom of some longitudinal girders.	Data-driven	Promising parameters to indicate structural damage in strain/acceleration SHM are the maximum strain response distribution under specific loading, as well as neutral axis location. To estimate the location and degree of degradation, a finite element model is needed.
[21]	Six-span bridge in Northern Italy	Concrete girder bridge, partly simply supported and partly supported with half-joints	Inclination, acceleration	Inclinometers and accelerometers on both sides of the bridge, on several locations across the spans as well as on the piers.	Short-term data-driven, long-term hybrid	The standard deviation of the acceleration data is continuously checked for anomalies, based on thresholds determined by commonly occurring values over the first three months of data. Moreover, a long term analysis of natural frequencies and modal shapes is performed through investigation of power spectral densities in combination with a FEM model. A clear seasonal influence was detected in the natural frequencies and eigenmodes, suspectedly caused by joint expansion or contraction due to thermal expansion of the bridge deck.
[22]	GAD bridge in Northern Italy	Concrete deck bridge using half-joints	Inclination, crack opening, accelerometers	Inclinometers on the bottom of both sides of a half-joint. Crackmeters at the location of significant visible cracks on the sides of the half-joint.	Initially data-driven, eventually more hybrid	Continuous data are connected to an automatic notification system, triggering necessary protocols. No data analysis results are documented in available literature. The book section by Alovisi et al. [23] possibly contains more information, but is unavailable.
[24]	Merone bridge in Italy	Concrete girder bridge using half-joints	Inclination, displacement, temperature	Inclinometers on upper nibs of half-joints on both sides of the bridge, and on piers and abutments. Displacement sensors in the middle of the spans and on both upper and lower nibs of half-joints.	Data-driven	The monitoring data of a limited sized dataset of 30 days indicated significant correlation between temperature and displacement measurements. No early warning system was installed.

1.3. Research Aim and Objectives

This research aims to explain the structural phenomena that seem to govern the measurement data of the SHM system on the Naardertrekvaart bridge. This knowledge can then be used to provide recommendations on the early warning system, raising an alarm in occurrence of damage. Furthermore, the findings can be used to provide recommendations on SHM systems on other half-joint bridges. To do this, the research will combine the development of multiple numerical models and the application of data analysis techniques. As part of the aim of this research, several objectives can be defined.

1. Capture hypothesised behaviour of the real structure in one or more numerical FEM models.
2. Estimate their significance through comparison of their effect on the deformation of the bridge with the measurement data.
3. Estimate the degree of damage of the support platform.
4. Provide a review of the SHM system.
5. Provide recommendations on early warning systems on other half-joint bridges.

1.4. Research Scope

This research aims to explain the measurements of the Naardertrekvaart bridge using multiple tools, which, due to its distinct shape, might not explain the behaviour of other half-joint bridges. The tools developed to assess the structural integrity of the half-joints might not be directly applicable on other half-joint bridges.

The knowledge gained from this investigation is used to provide recommendations on the monitoring approach and early warning system of the bridge. The results of this case study are used to provide a general recommendation on the possible SHM approach on other half-joint bridges. This recommendation is purely based on the experiences of this research.

1.5. Research Questions

Main research question:

> *How can measurements from the active SHM system on the Naardertrekvaart bridge be used as an indication for the occurrence of degradation?*

Subquestions:

1. What are common failure modes of half-joint bridges?
2. What are the causes of occurrence of half-joint bridge failure?
3. Which degradation mechanisms are occurring in the Naardertrekvaart bridge?
4. What other properties of the Naardertrekvaart bridge might differ from its design?
5. How can the differences between the Naardertrekvaart bridge as designed and the bridge in reality be incorporated by one or more linear-elastic FEM models?
6. How does the Naardertrekvaart bridge as it was designed respond to regular loading?
7. How does the Naardertrekvaart bridge as it is now respond to regular loading?
8. How can the current measurement system be used to raise a warning at the onset of damage?
9. What is the best approach to set up an SHM system on other half-joint bridges?

2

Literature Review

This chapter contains the literature review performed for this research. Section 2.1 contains a review of literature regarding the degradation of half-joint bridges. Section 2.2 contains a review of existing literature regarding the loads on concrete bridges. Section 2.3 contains a review of existing literature regarding structural health monitoring of bridges.

2.1. Degradation of Half-joint Bridges

The half-joint system manages to implement a hinge in the bridge deck while maintaining a level-running surface [2, 6]. This internal hinge prevents the occurrence of internal stressed due to differential settlement of the supports [4]. However, half-joint bridges exhibit significant cracking at the location of the half-joint, which in some cases can lead to global failure. Section 2.1.1 describes the different possible failure modes of half-joints. Section 2.1.2 describes the factors that can cause the formation of cracks at the location of the half-joint. Section 2.1.3 describes the structural degradation mechanisms that can accelerate the occurrence of failure.

2.1.1. Failure Modes of Half-joints

The load that is exerted on the bridge deck of a half-joint bridge, is transferred to the supports through the half-joint. When looking far away from the half-joint, the structure can be accurately modelled as an undisturbed region. However, close to the half-joint, the structure should be considered a disturbed region, as stress trajectories follow a discontinuous pattern [6, 25]. This can be seen in Figure 2.1. The stress trajectories show the tensile stresses close to the re-entrant corner, indicating a weak point for concrete cracking [17].

This weak point can lead to several crack patterns, which can ultimately lead to a failure mode. The different possible failure modes can be found in Figure 2.2 and Table 2.1. Which failure mode occurs depends on different factors like dimensions of the half-joint, material properties and reinforcement detailing [17]. Failure mode 3 and 4 occur most commonly [6].

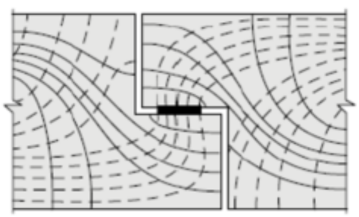

Figure 2.1: Stress trajectories of uncracked concrete half-joint [17]

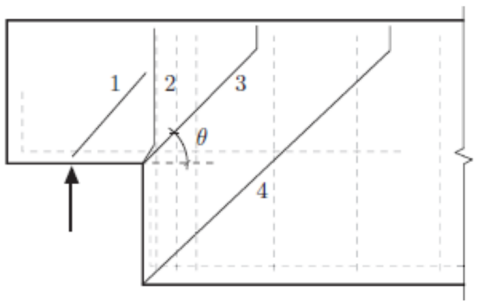

Figure 2.2: Failure modes of concrete half-joints [17]

Table 2.1: Potential failure modes with corresponding mechanisms [17]

	Failure mode	**Failure mechanism**
1.	Diagonal crack in nib	Concrete compressive or tensile strength is exceeded
2.	Direct shear crack	Rupture of horizontal rebar in nib
3.	Diagonal crack in re-entrant corner	Rupture of horizontal rebar, hanger-reinforcement and/or diagonal rebar
4.	Diagonal crack over full depth	Rupture of hanger-reinforcement or inadequate detailing of reinforcement

2.1.2. Underlying Causes of Structural Degradation of Half-joints

The eventual occurrence of one of the half-joint failure modes described above can be caused by multiple degradation mechanisms. At the root of these degradation mechanisms often lies an accumulation of underlying problems. The most common underlying problems with half-joints, accelerating the occurrence of degradation mechanisms, are described in the following sections.

Improper Vertical Reinforcement Detailing

Improper shear reinforcement detailing can reduce the bearing capacity of the half-joint nibs, causing the formation of large shear cracks, generally starting at the location of a re-entrant corner [5]. To prevent this, vertical reinforcement must be placed sufficiently close to the re-entrant corner [13, 14, 15, 16]. This vertical reinforcement could be provided as stirrups, or as so-called hanger-reinforcement, connecting the top and bottom longitudinal reinforcement. To provide the best support for the compression strut at the location of the support reaction, this hanger reinforcement should be bent into the nib, forming a Z-bar. Formation of a diagonal crack starting from the re-entrant corner can also be prevented or reduced by diagonal reinforcement close to the re-entrant corner [6, 26]. Vertical and diagonal reinforcement should be combined for optimal performance.

Improper Longitudinal Reinforcement Detailing

As mentioned in Section 2.1.1, parts of the structure that lie close to the location of the half-joint should be regarded as a disturbed region, and therefore the reinforcement should be detailed accordingly in both sides of a half-joint. In this design, proper anchorage is extremely important [10]. However, most of the half-joints constructed in the last century had no code provisions to rely on regarding the reinforcement design of disturbed regions [11]. As a result, anchoring of the longitudinal reinforcement was often insufficient, consisting of solely straight rebars running to the edge of the half-joint. This was also the case for the La Concorde overpass, visible in Figure 2.3.

Deviation from Design Reinforcement

Following from the importance of proper reinforcement detailing close to the nibs of the half-joint, deviation from this design can hinder its ability to minimise crack formation at the location of the re-entrant corner. In several investigations of collapsed half-joint bridges, forensic analysis showed that the constructed reinforcement differed from the designed reinforcement [11, 27].

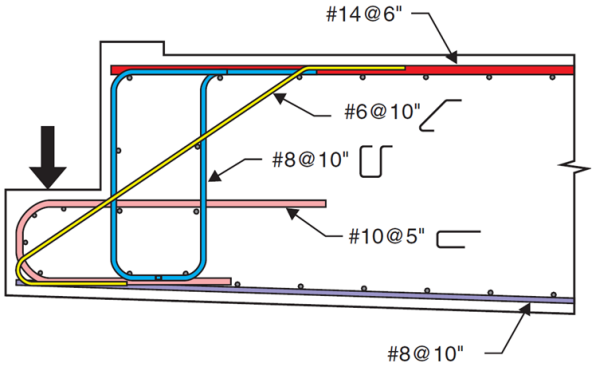

Figure 2.3: Design reinforcement of the La Concorde overpass [11].

Insufficient Inspection and Maintenance

Due to water accumulation at the location of the re-entrant corner of lower nibs of half-joints, these nibs suffer the most from deterioration. Due to the small gap inside the joints, sometimes even filled with filling material, inspection of the lower nib is very difficult. As a result, the exact degree of deterioration of the half-joints often remained unknown during their lifetime, causing insufficient maintenance to be carried out [2, 3, 4, 5, 28].

Filling Material in Half-joint Gap

In some cases, the gap inside a half-joint is filled with a filling material, meant to reduce intrusion of water or other substances. This material not only negatively affects the ability to perform inspections inside the half joint, but might also affect the behaviour and rotational capacity of the joint [3], possibly speeding deterioration mechanisms.

Breakage of Expansion Joint

To prevent intrusion of water or other material into the half-joint gap, they are usually instrumented with expansion joints. Breakage of these joints can occur due to dynamic traffic loads [11, 17, 28, 29]. Additionally, bituminous expansion joints can exhibit breakage due to their increased stiffness during periods of low temperatures, when the joints need to facilitate thermal contraction of the structural elements. Breakage of the expansion joints can facilitate intrusion of water into the half-joint, favouring degradation mechanisms.

2.1.3. Structural Degradation Mechanisms in Half-joint Bridges

In half-joint bridges, several degradation mechanisms can, in combination with the crack formation mechanisms described above, lead to structural failure. These degradation mechanisms are described below.

Corrosion of Reinforcement Steel

Corrosion of reinforcement steel is the result of an electromechanical process, which uses iron, water and oxygen. Initially, the reinforcement bars in concrete are protected against corrosion by a passive layer, formed due to the high alkalinity of concrete pore water. This layer can be broken either by carbonation or due to presence of chloride. Carbonation generally causes a very widespread form of corrosion, resulting in early cracking of concrete and spalling, further exposing the concrete and favouring the corrosion process. Chloride induced corrosion generally causes a very local attack on the reinforcement (pitting corrosion), resulting in a very local, significant reduction of effective reinforcement cross section [30]. As a result, corrosion of reinforcement bars has a significant negative effect on the strength of a reinforced concrete element [31].

Research shows that corrosion of the hangup and diagonal reinforcement bars close to the re-entrant corner of the half-joint has great impact on half-joint capacity [5]. This re-entrant corner is also the location where cracks often initiate due to the localisation of tensile stresses, favouring water and oxygen ingress.

Freeze-thaw Deterioration

Another cause of structural deterioration are freeze-thaw cycles. In this process, freezing of capillary water increases capillary pressure, causing exceedance of tensile strength of the concrete and formation of cracks [32, 33]. Moreover, half-joints in bridges generally have to endure seepage of water dissolved with de-icing salts. Although the presence of dissolved de-icing salts mitigates the deterioration due to freezing of the capillary water by lowering the freezing point of water, it does cause crack formation due to generation of crystallisation pressure [34].

2.2. Loads on Concrete Bridges

Bridges on highways have to endure multiple loads, consisting of permanent and variable loads. Permanent loads are the self-weight of the bridge and installations, which are briefly described in Section 2.2.1. Variable loads on bridges are predominantly caused by traffic and temperature, and are described in Section 2.2.2 and 2.2.3 respectively.

2.2.1. Self-weight

The self-weight of the bridge members and installations can greatly influence the behaviour of a bridge. Initially, the self-weight causes deformations in an unloaded state. Moreover, an increasing self-weight reduces the natural frequencies of a structure, affecting the dynamic behaviour of the bridge [35]. The self-weight of the bridge should be determined based on construction drawings along with material properties.

2.2.2. Traffic Loads

Vertical loads of road traffic in the Netherlands can be estimated using weigh-in-motion (WIM) measurements. These measurements are gathered by WIM-stations, implemented into the pavement of highways, continuously measuring the weight of heavy vehicles. Measurements of a WIM-station located in Woerden in the Netherlands, measured an average gross vehicle weight of approximately 20 tons over a time span of 20 weeks in 2005 [36].

The force exerted on a surface by a moving vehicle does not only have a static component, equal to its self-weight, but also has a dynamic component. This dynamic component causes a fluctuating magnitude of the exerted force over time. The dynamic component causes the maximum force exerted by the vehicle to be larger than its self-weight. The dynamic component of the vehicle load can be caused by multiple phenomena like road surface irregularities, horizontal acceleration, or unbalanced loading [37]. When estimating traffic loads, a dynamic amplification factor (DAF) should be used to take into account the additional dynamic component of the vehicle load. Eurocode 1 [38] prescribes the use of a DAF of almost 1.40, which is a conservative value. Studies show that the actual magnitude of the DAF depends on the gross vehicle weight, and can take values of close to 1.05 for heavyweight vehicles [39].

2.2.3. Thermal Loads

Solar radiation and ambient temperature can cause significant variations in average temperature and temperature gradients along a concrete bridge, especially along the depth of the bridge deck. This effect is highly non-linear, due to factors like material type, bridge orientation and shading [40]. The average material temperature is mostly dependent on annual temperature cycles, while temperature gradient shows similar dependence on both diurnal and annual temperature cycles [41]. Temperature gradient can impose significant bearing displacement on a bridge [42] and can induce longitudinal strains larger than those induced by traffic loads [43].

Thermal loads can also influence the dynamic behaviour of bridges, through the shift of natural frequencies. This shift can reach from 0% to 15%, affecting the natural frequencies corresponding to bending modes more than those corresponding to torsional modes [40]. This frequency shift can be partly accredited to the reduction of elastic modulus of concrete with increasing temperature, which influences the stiffness of a structure [44]. Another cause of frequency shift could be bridge joint expansion due to thermal expansion of the bridge deck [21].

2.3. Structural Health Monitoring of Bridges

With many bridges all over the world reaching the end of their service life, road operators are faced with the challenge of assessment of their structural safety. This assessment can be performed instantly in a non-destructive manner, for instance by visual inspections, or in a destructive manner, for instance by lab-testing of part of the structure. As a non-destructive method, the application of Structural Health Monitoring (SHM) could be considered, which gives more insight into the behaviour of structures over time. This method can be particularly useful when visual inspections are difficult to perform. However, SHM systems are generally expensive to install and maintain, which is why road operators often only install them on bridges that have a high priority [45].

SHM systems are specifically interesting for half-joint bridges, as visual inspection inside of the half-joint is immensely difficult. Therefore, SHM systems can provide valuable insights into the behaviour of the bridge, mitigating the need for destructive measures to assess the condition of the joint.

When a road operator decides that a SHM system will be installed, also decisions should be made regarding the types of sensors, their location and how to analyse the measured data. Section 2.3.1 describes the options regarding sensor placement. Section 2.3.2 describes the different data analysis approaches that can be used to interpret the data and devise an early warning system.

2.3.1. Sensor Type and Placement

Upon acknowledging the need for placement of a SHM system on a bridge, there are multiple choices regarding the types of sensors to place. These sensor types can be placed alongside each other to create an extensive SHM system that can capture multiple structural phenomena and can provide redundancy, which enables the assessment of sensor accuracy. The most used SHM sensors can be divided into three categories [46]:

- Kinematic sensors
  - Acceleration
  - Velocity
  - Displacement
- Mechanical sensors
  - Material fatigue
  - Local forcing
  - Strain
  - Corrosion
  - Crack detection
- Ambiental sensors
  - Wind
  - Temperature

The types of sensors to be placed in an SHM system and their locations are highly dependent on the structural system that needs to be analysed and the structural phenomena that need to be investigated. As part of a large monitoring and maintenance initiative, a flow-chart to guide decision making regarding the safety assessment of transportation infrastructure was developed, for which the lessons of multiple SHM systems were used [45, 47]. After decision of placement of a SHM system, the flow-chart advises placement of sensors across the whole structural system in case of a complex structural scheme, and placement of local sensors on key components in case of a simple structural scheme.

2.3.2. Data Analysis Approaches

The measurement data acquired by the SHM system can be analysed in two ways: using a data-driven approach or a model-driven approach. A data-driven method involves the use of data analysis techniques to find patterns in the measurement data, for instance by applying data-mining, clustering or artificial intelligence. Contrarily, a model-driven method uses a digital twin in the form of a FEM model

to simulate the behaviour of the structure that drove the measured data [22]. A third approach is a so-called hybrid approach, combining a data-driven with a model-driven approach [48]. Different data analysis approaches can be rated on how much insight they offer into the degradation process of the structural system. This can be done following the Rytter's hierarchy, visible in Table 2.2.

Table 2.2: Rytter's hierarchy, describing the level of damage diagnosis of a model [49]

Level	Description
Level 1: Detection	The method gives a qualitative indication that damage might be present in the structure.
Level 2: Localization	The method gives information about the probable position of the damage.
Level 3: Assessment	The method gives an estimate of the extent of the damage.
Level 4: Prediction	The method offers information about the safety of the structure, e.g. estimates a residual life.

Data-driven Approach

The data-driven approach makes use of statistical models, identifying damage purely based upon the measurement data. This identification can be done through either statistical pattern recognition or machine learning. Statistical pattern recognition can be conducted in a supervised manner, where the dataset contains measurement data of both the undamaged and the damaged structure, or in an unsupervised manner, where the dataset contains only data of the undamaged structure. Generally, unsupervised pattern recognition methods are restricted to providing a level 1 damage diagnosis.

Machine learning can deliver damage detection in an unsupervised learning approach, using techniques like outlier analysis and control chart methods. In a supervised learning approach, techniques using artificial neural networks, support vector machines and kernel discriminant analysis can be applied.

The data-driven approach offers a lot of functionality in damage detection, theoretically being able to simulate the behaviour of structures of any complexity, as long as it has enough trainable features. Moreover, this approach automatically takes into account uncertainties. However, as data of the investigated structure in a damaged state are often unavailable, machine learning is generally performed in an unsupervised manner. This method limits the ability of the model to predict the behaviour of the structure in its damaged state. Moreover, as the number of trainable parameters in a machine learning model increases, so does the amount of training data needed for proper training of the model. Lastly, the use of a data-driven approach generally involves the creation of a (partly) "black box model". This type of model does not take into account any physical laws, but aims to simulate the output data based on the input in a purely mathematical manner. As a result, a black box model offers limited insight into the physical behaviour of the structure under investigation [48].

Model-driven Approach

The model-driven approach generally involves the development of a FEM model that represents the structural system. The model parameters, like mass, stiffness and damping coefficients, are calibrated using the measurement data by means of model updating methods, in order for it to be able to replicate the behaviour of the actual structure. When a sufficiently representative model has been developed, model updating is performed using incoming data, in order to detect, locate and quantify any occurring damage. This approach can be described as solving an inverse problem.

The model-driven approach offers much functionality in describing the behaviour of the investigated structure when data of the damaged structure are unavailable, delivering up to a level 4 damage diagnosis. A drawback of this approach is its inability to account for uncertainties. Also, this approach might not be able to exactly simulate the actual behaviour of the investigated structure, due to inevitable simplifications implemented into the model in order to minimise the need for computation power [48].

Hybrid Approach

The data-driven and model-driven approaches can also be combined into a hybrid approach, which can complement each other. This approach generally involves the development of a FEM model, similar

to the model-driven approach. When this model is unable to completely explain the measurement data, due to any implemented modelling simplifications, a data-driven approach is used to explain the residuals between the FEM model output and the measurement data.

This approach, making use of the qualities of both approaches and mitigating most of the drawbacks, can be a very effective approach to SHM data analysis [48]. However, combining both approaches also involves the development of both a FEM model and a statistical model, complicating the researching methodology.

2.3.3. Structural Health Monitoring of Half-joint Bridges

Due to the difficulty of inspecting the condition of the concrete inside a half-joint, SHM systems can prove a helpful tool to assess structural safety. Several examples of SHM systems on half-joint bridges can be found in literature. Four of these publications give a clear description of the sensor placement and describe to some extent how the measurement data are used to interpret the behaviour of the structure. The corresponding SHM systems are described below.

Three-span Bridge, Australia

In western Australia, a three-span bridge was constructed following the half-joint system. In this bridge, eight longitudinal girders are supported by eight longitudinal cantilevers by a half-joint. The half-joints were strengthened externally after construction in longitudinal connection by a horizontal bar running through the joint, as well as in vertical direction by a diagonal bar running close to the re-entrant corner [50]. A schematic figure of the bridge, along with a cross section of the half joint can be found in Figure 2.4. An SHM system was installed in 2014, measuring horizontal strain at the bottom and the top of the centre of the girders, measuring acceleration at the bottom of the outer girders, and measuring strain of the diagonal external strengthening rods at one of the half-joints, on the outer two girders [50].

The measurement data were analysed following the data-driven method. The system was instructed to record data in a time-window of two minutes, only when exceedance of a predefined threshold was recorded. In that case, all data between one minute before and one minute after the exceedance would be recorded, including images taken from a fixed elevated camera to show the vehicle that caused the exceedance [50]. The data were analysed to investigate what measurable parameters could be used to indicate structural damage. The maximum strain response under certain specific vehicle types with the same loading, travelling in the same lane, was estimated to be a reliable parameter [20]. A change of this response over time would indicate structural damage. Another reliable parameter would be the neutral axis locations of the girder beams, as they show no dependence on vehicle type and travelling lane [20, 51, 52].

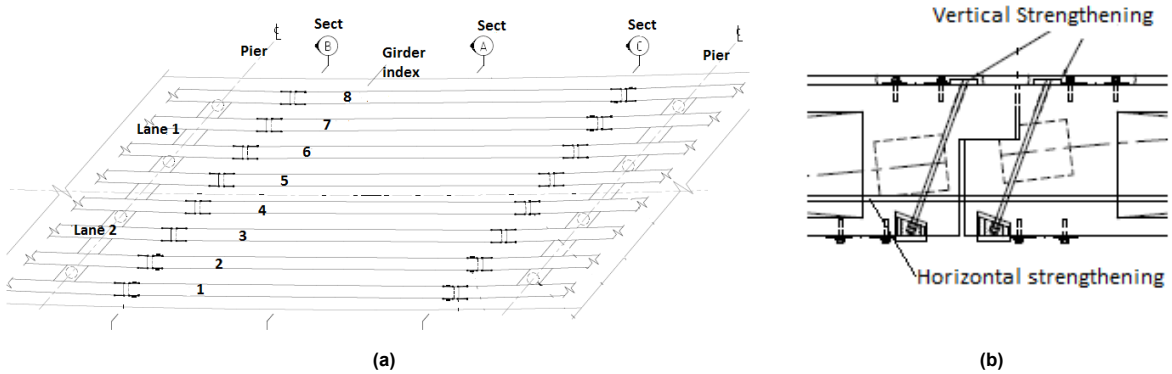

Figure 2.4: Schematic arrangement of the central span of the three-span bridge with (a) a top-view and (b) a cross section of the half-joint [50].

Six-span Bridge, Italy

This bridge, consisting of six spans of 15 to 20 meters, was constructed in the late 1960's in Northern Italy. It is a concrete girder bridge with five longitudinal girders and three transversal beams per span. A top and side view of the bridge is visible in Figure 2.6. Span C1 is simply supported on the north

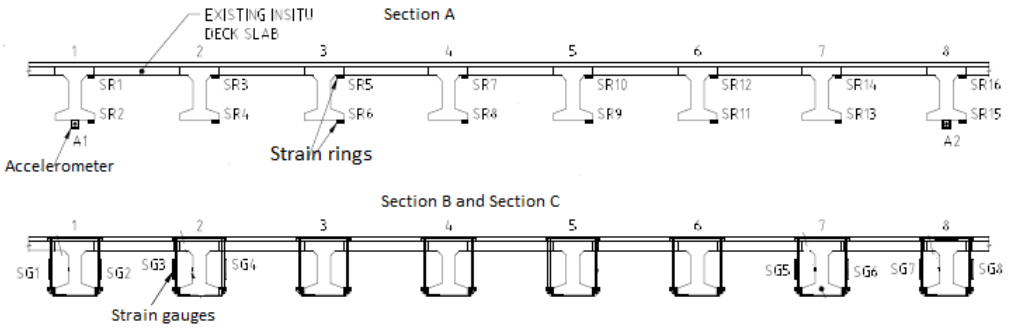

Figure 2.5: Locations of the sensors on the three-span bridge in Australia [50].

abutment and the first pier, while span C3 and C5 are supported on their neighbouring bridge decks using half-joints. In 2019, the bridge was instrumented with 72 bi-axial inclinometers and 42 tri-axial accelerometers, all equipped with humidity and temperature sensors. The SHM system setup can be found in Figure 2.6 [21].

The inclinometers gather data at a measuring frequency of 208 Hz, where once per second statistical parameters like mean value, standard deviation, maximum and minimum rotation, internal temperature and relative humidity are stored. The accelerometers gather data at a measuring frequency of 25.6 kHz, which is filtered and down-sampled at the microcontroller level to store data with a sampling frequency of 100 Hz. To save memory of the cloud storage, the gateway only uploads data at time intervals that contain significant vibrational response.

The analysis of the measurement data is split into two parts. The first part consists of real-time anomaly detection based on the standard deviation of the acceleration data. This system proved to be useful in detecting and localising damage to the bridge, as previous indications of damage were confirmed by visual inspections and were followed up by appropriate maintenance interventions, which reduced the standard deviation back to normal values. This process can be seen in Figure 2.7.

The second part consists of a long-term diagnostic analysis of the modal response of the structure. Natural frequencies of the structure are found through analysis of the power spectral density diagram of the accelerometers. The outcome is used to calibrate a FEM model, which gives insight into the modal shapes. The analysis showed that the dynamic configuration changed between summer and winter time. In summer time, the structure displayed stiff behaviour with only one lateral mode and one flexural mode. In winter time, the structure displayed less stiff behaviour, with two lateral modes and one flexural mode. The two modes that occur in summer time seem to correspond to two of the modes that occur in winter time, while exhibiting a slight, but significant, frequency. The additional lateral mode that occurs in winter time, disappears during summer time. The difference in natural frequencies between the seasons, along with the increased stiffness of the structure during summer time, indicates closure of the joints during summer due to thermal expansion of the bridge decks.

GAD Bridge, Italy

The GAD bridge is a prestressed reinforced concrete plate bridge in northern Italy constructed in 1983, which uses the half-joint system. It was constructed in 1983 and it facilitates highway traffic. As the half-joints showed insufficient resistance to shear, due to insufficient shear reinforcement, the half-joint was strengthened using prestressed transversal bars [47]. To monitor the behaviour of the half-joints until scheduled deck replacement, an SHM system was installed in 2019. As part of the SHM system, multiple half-joints were equipped with clinometers, measuring the rotation at each side of the half-joint, crack meters, measuring the crack opening of of the visible cracks, and temperature sensors. The SHM system can be found in Figure 2.8. The measured data are continuously analysed by algorithms measuring sudden variations exceeding predefined thresholds, which have been pre-defined based on regular variations of the measured variables. Thereby, this system is mostly data-driven. If no anomalies are found, the data are uploaded to the cloud to be used for long-term data analysis [22].

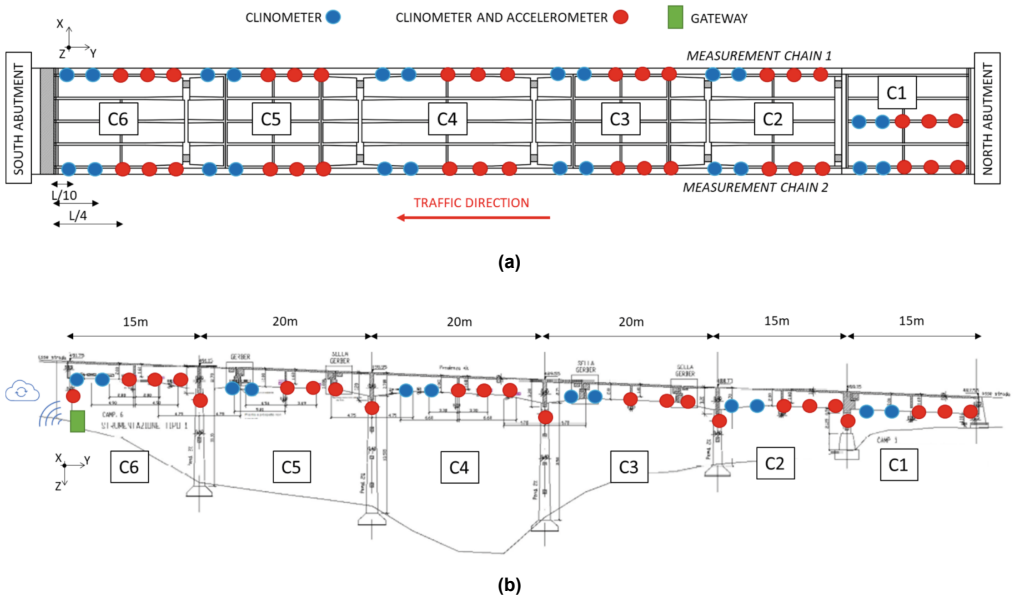

Figure 2.6: Schematic of the six-span bridge and the location of the sensors with (a) a top-view and (b) a side-view [21]

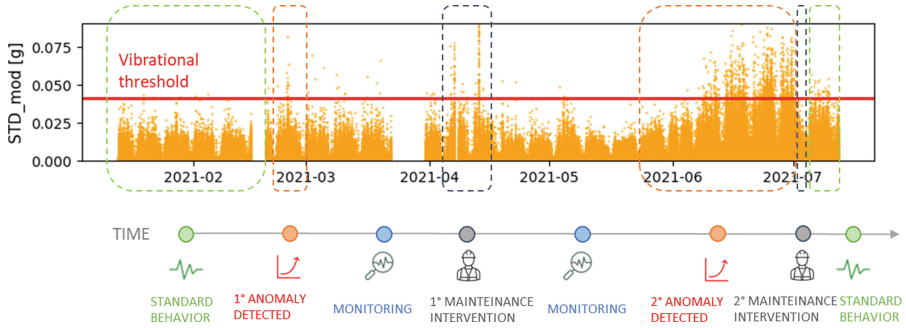

Figure 2.7: Timeline of the standard deviation values of a single accelerometer [21]

Merone Bridge, Italy

The Merone bridge, built in 1969 in Merone, is a viaduct with nine spans with lengths of 26 to 29 meters. The spans are supported by cantilever beams using half-joints, and are composed of seven longitudinal prefabricated prestressed concrete I-beams and several transversal stiffening beams [24]. A schematic top-view and deck cross section of the bridge can be found in Figure 2.9. After the inspection of localised damage, including at the location of the half-joints, an SHM system was installed in 2018. The system consists of tiltmeters and displacement meters along the width of the bridge, in span S1 and span S5, along with a weather station measuring the ambient temperature [24, 53].

Until now, the data were analysed following a data-driven approach, looking for correlation of displacement measurements with temperature. From analysis of a limited sized dataset spanning 30 days, there appeared to be significant correlation between temperature and displacement measurements [24].

(a) (b)

Figure 2.8: SHM system on the GAD bridge with (a) a deck view of the overpass and (b) the installed tiltmeters and crackmeters [22].

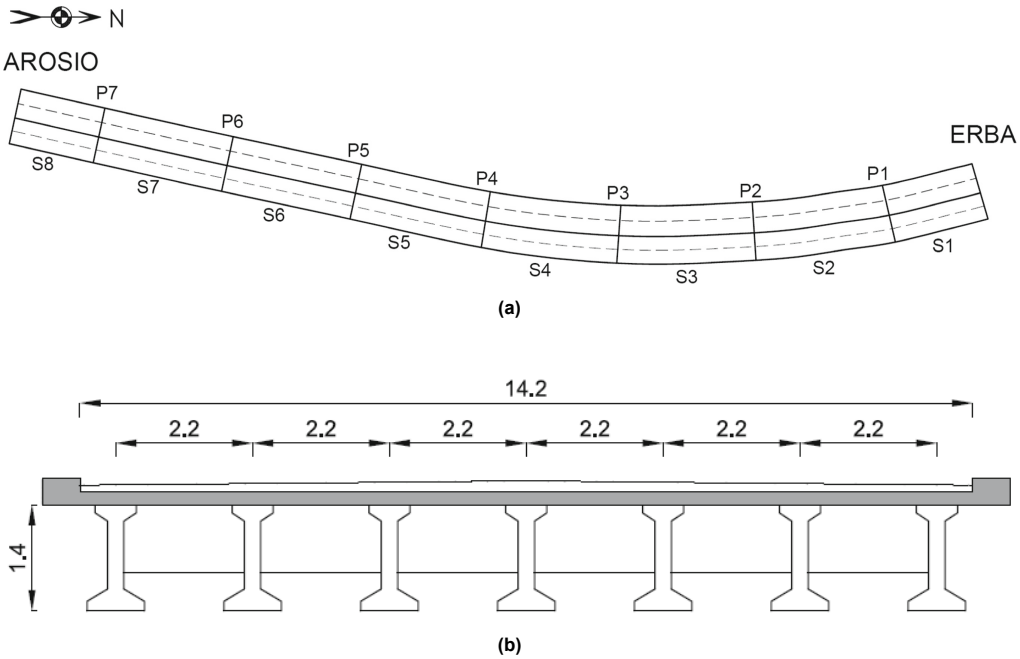

Figure 2.9: Schematic of the Merone bridge with (a) a top-view and (b) a cross section of the deck [24].

3

Naardertrekvaart Bridge

In this chapter, the relevant characteristics of the Naardertrekvaart bridge are described. In section 3.1, the structure of the Naardertrekvaart bridge is described. In section 3.2, the current state of the Naardertrekvaart bridge is described. In section 3.3, the SHM system of the Naardertrekvaart bridge is explained.

3.1. Structure of the Bridge

The Naardertrekvaart bridge consists of two separate bridges, a northern and a southern bridge, both containing 11 supports and 10 spans, of which 9 standard spans and 1 divergent span between support 3 and 4. The bridge is slightly slanted along its width to account for the curvature of the road. A top view of the bridge can be found in Figure 3.1. The relevant design drawings of the bridge can be found in Appendix A.

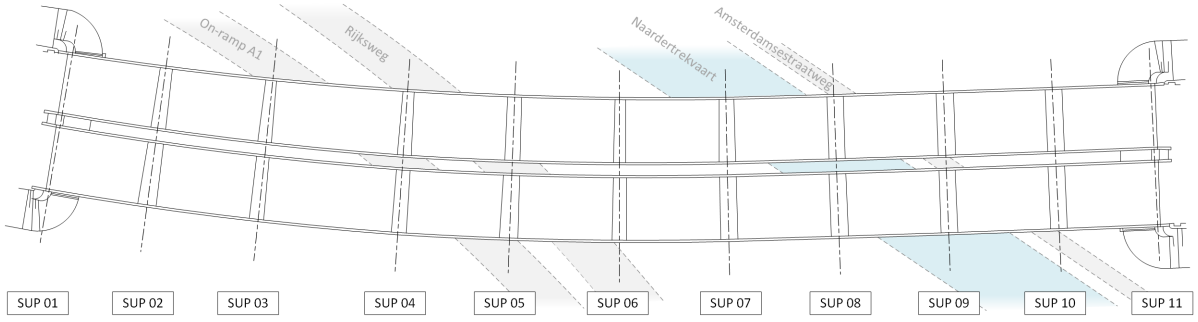

Figure 3.1: Top view of the Naardertrekvaart bridge

Each spanning bridge deck consists of 11 prefabricated, prestressed longitudinal girders with a T-shaped cross section, connected to a concrete compression layer that spans the full width of the bridge. While the standard spans use HIP girders, which are inverted T-beams of reinforced concrete, the divergent span has a longer span and uses Preflex girders, which have a composite cross section consisting of a steel HEB1000 profile surrounded by a reinforced concrete cross section. Supports 1 and 11 are abutment supports, while supports 2 to 10 are concrete platforms supported by concrete columns, often called bearing tables. Figure 3.2 shows a street view image of support 5 of the southern bridge. Figure 3.3 shows the composition of the standard spans and that of the divergent span.

The longitudinal girders are supported by supports 2 to 10 using half-joints. The longitudinal girders are connected to each other at both ends using in-situ casted transversal beams. In addition, some transversal connection beams are present between the longitudinal girders, which serve to keep the girders at constant spacing and do not play a significant role in load transfer. The web of the longitudinal girders is supported on the nib of the support platform by rubber bearing plates, at locations where the

Figure 3.2: Street view image of support 5 of the southern Naardertrekvaart bridge (Google Maps)

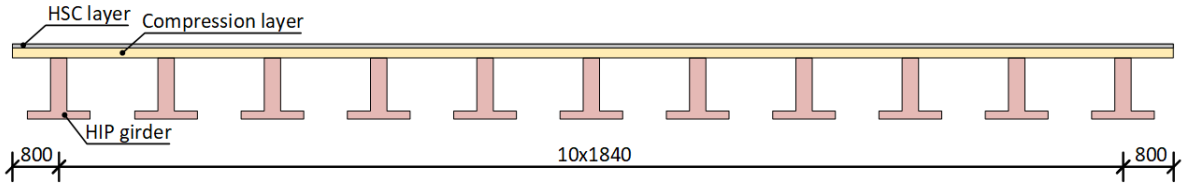

(a) Cross section of a standard span of the Naardertrekvaart bridge

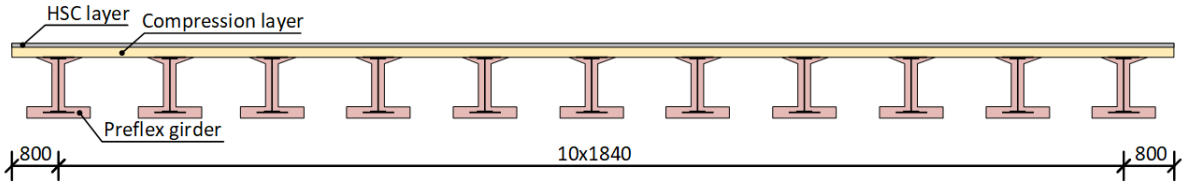

(b) Cross section of the divergent span between support 3 and 4 of the Naardertrekvaart bridge

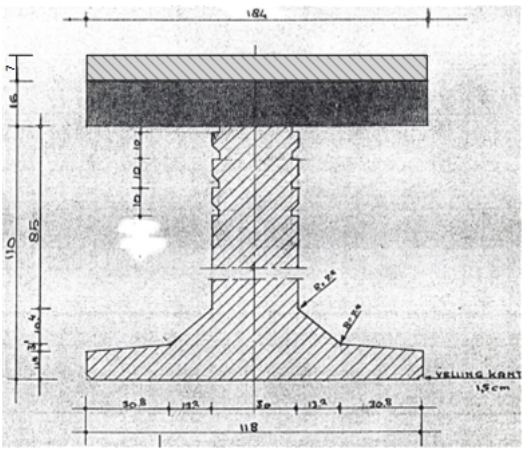

(c) Composition of the HIP girder with compression layer. Dimensions in cm.

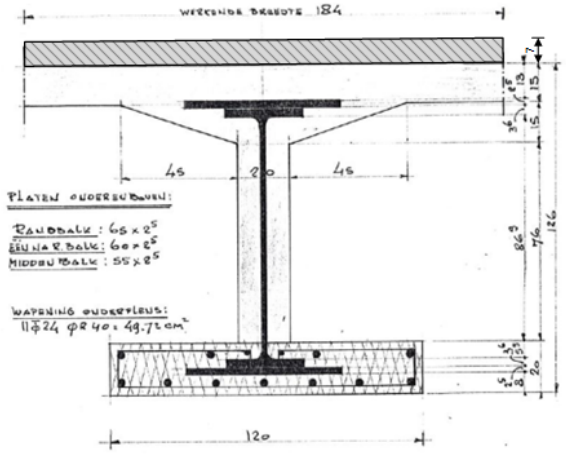

(d) Composition of the Preflex girder with compression layer. Dimensions in cm.

Figure 3.3: Composition of the spans of the Naardertrekvaart bridge

lower nib has a reduced thickness. A schematic side view of the half-joint of a regular span can be found in Figure 3.4. The reinforcement of the platform varies slightly across its width, due to the reduction in the thickness of the nib at the location of the supports of the longitudinal girders. The two types of design reinforcement of the support platforms next to a standard span can be found in Figure 3.5. This figure also contains the annotations of the different reinforcement bars that will be used in the rest of this thesis.

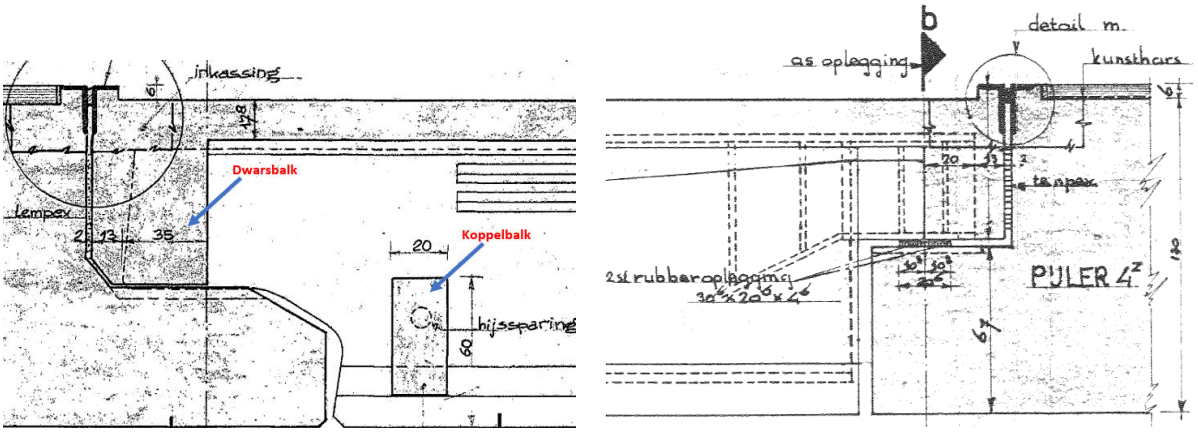

(a) Half-joint of a regular span

(b) Half-joint of the divergent span

Figure 3.4: Side view of the half-joints of the Naardertrekvaart bridge

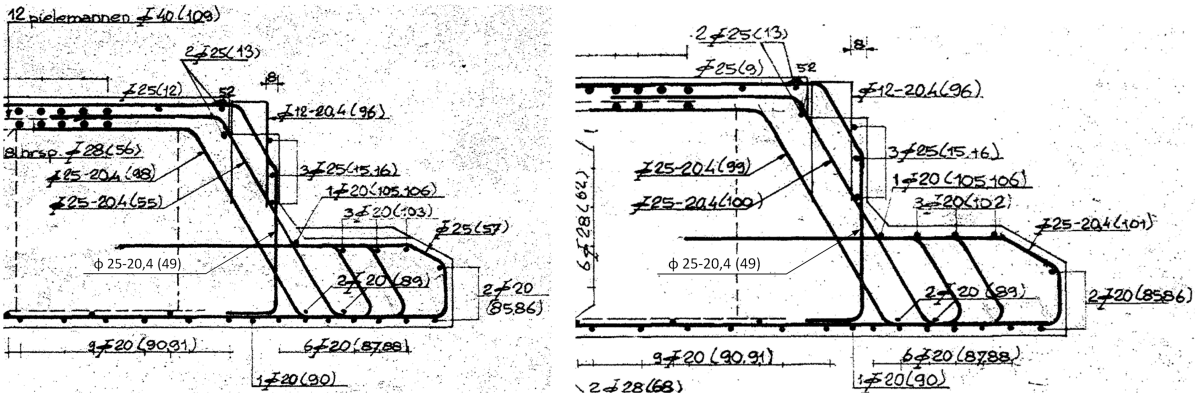

(a) Reinforcement at the location of a longitudinal girder

(b) Reinforcement between the longitudinal girders

Figure 3.5: Reinforcement of the support platform of a standard span of the Naardertrekvaart bridge

The dimensions of the supports of the Naardertrekvaart bridge differ along its length due to the slope, slant, and curve of the road. Resulting from its curve, the support platforms of the bridge are longer on the southern side of the bridge than they are on the northern side.

The rubber bearing plates of the standard spans have dimensions $356 \times 256 \times 46$ mm, while the bearing plates of the divergent span have dimensions $206 \times 306 \times 46$ mm, with two plates supporting one longitudinal girder. The bearing plates are comprised of steel plates alternated with rubber layers. The exact composition of the bearing plates is not visible in the design drawings, but based on the dimensions they are expected to have been manufactured by Vredestein, having the composition shown in Figure 3.6.

3.2. Current State of the Bridge

During its lifetime, the Naardertrekvaart bridge exhibited several different types of damage. Consequently, multiple restoration procedures were carried out. A complete overview of damage inspections and restoration procedures can be found in Appendix B. As some of the damages and restorations, specifically at the location of the half-joints, could influence the behaviour of the bridge, the state of

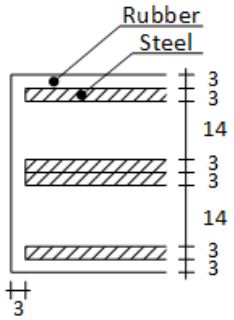

Figure 3.6: Composition of the bearing plates of the Naardertrekvaart bridge. Dimensions in millimetres.

several key components of the bridge are described in the following sections.

3.2.1. Current State of the Reinforced Concrete Elements

At multiple of the inspections performed at several stages in the lifetime of the bridge, leakage of the expansion joints was observed. These expansion joints, intended to prevent the seepage of water into the half-joints, tend to exhibit premature breakage, as described in Section 2.1.2. Moreover, insufficient reinforcement close to the re-entrant corner possibly led to the formation of a diagonal crack in the lower nib of the half-joint, originating from the re-entrant corner. As a result, water could seep into the diagonal crack and reach the reinforcement bars, possibly causing corrosion. This hypothesis is in line with the observation of concrete spalling at multiple locations on the support platform close to the half-joint, possibly caused by reinforcement corrosion. Furthermore, in 2015 and 2019, at several locations close to the half-joint, the electric potential of the support platform reinforcement bars was measured to detect the occurrence of corrosion. These investigations were carried out only at four locations along the bridge, three of them being on the northern bridge. Some of the measured electric potential values indicated the occurrence of corrosion, but the results were inconclusive.

Inspections in 2015 and 2017 showed that in some cases the reinforcement of the support platforms differs from the design reinforcement. At several locations for instance, stirrup 89 seemed to lay underneath the diagonal reinforcement bars 99, 100 and 101, reducing their effectiveness in transferring vertical forces to the top of the element. Inspections also indicated a large variation in the concrete cover, reaching values as low as 19 millimetres with a design concrete cover of 30 millimetres.

As the inspections did not establish a direct relation between water ingress or divergent reinforcement and the occurrence of corrosion, the exact state of the reinforcement bars of the support platforms remains unknown.

3.2.2. Current State of the Joint Gaps

During inspections, the presence of Expanded Polystyrene (EPS) inside of the half-joint gaps was confirmed, which was originally used as formwork for the in-situ casted transversal end beams and compression layer. EPS should be removed after hardening of the concrete, but is regularly left inside of the structure [3]. This material in the half-joint gaps not only complicates inspection of the half-joint, but might also affect the behaviour of the structure. Although this material is generally assumed to have a negligible stiffness in practice, with a maximum stiffness of around 5 MPa [54, 55, 56], it could exert a significant stress when compressed. The total resisting force could reach significant values as the thickness of the gap reduces. It is unknown if the EPS material fills the gap completely, as the size of the bridge deck and girder is influenced by creep and relaxation along with thermal expansion. Therefore, it is unknown at which instance the stress development of the EPS initiates.

Inspection of the connection between the lower half-joint nib and the transversal beam reveals no clear gap between the elements, which would serve to allow free horizontal expansion of the half-joints. As a result, significant horizontal stress could develop due to hindered thermal expansion or contraction of the structural elements. Furthermore, during inspection in 2015, a bituminous seal was discovered in some locations between the transversal end beams and the support platforms, presumably intended

to increase the concrete cover. This seal could increase the stiffness of the connection even more.

Following from these remarks, it can be concluded that the fully isostatic behaviour of the bridge, which a healthy half-joint should facilitate, can not be guaranteed.

3.2.3. Current State of the Expansion Joints

The expansion joints, intended to facilitate a smooth transition for crossing traffic while allowing free expansion of the bridge components, initially consisted of simple steel grills. There is no sign that they were also instrumented with gutters to provide rainwater drainage. As a result, presumably the initial expansion joint fully enabled the seepage of rainwater into the joints. Following the discovery of water damage in 1988, the vertical surfaces of the half-joint gap were conserved using Latexfalt and the expansion joints were replaced by a bituminous joint in 1994. The bituminous expansion joints were replaced in 2007 and 2016 after the joints were again found to be leaking. In addition, between 2018 and 2019 the bituminous expansion joints have been repaired with a bituminous seal.

Bituminous expansion joints have a significant variation in stiffness depending on their temperature. At high temperatures, they facilitate a relatively free expansion of the joints, but with a decreasing temperature, their stiffness increases exponentially and the thermal contraction of the bridge deck components could be hindered. In extreme winter, the adhesive layer between the bituminous material and asphalt and concrete can break, once again facilitating the seepage of water into the half-joint gap. A broken bituminous expansion joint can be resealed with a bituminous seal between the joint and the asphalt layer, but this repairing measure often proves to be insufficiently effective. Therefore, it is reasonable to assume that some of issues with the repaired expansion joints in the Naardertrekvaart have recurred.

3.2.4. Current State of the Bearing Plates

The steel plates of the rubber bearing plates, which are the most prone to degradation, are shielded by the outer layers of rubber. As a result, the degradation of the bearing plates is expected to be negligible and should not have an effect on their stiffness.

3.3. SHM System

As described above, the expected damage of the half-joints, reinforcement corrosion caused by formation of a crack in combination with water ingress, occurs deep inside the half-joints. This location is very difficult to inspect. In case of the Naardertrekvaart bridge, support 5 and 6 of the southern bridge showed the most signs of water damage, indicating being prone to structural degradation. To gain insight into the structural integrity of the half-joints of these supports without the need for inspection inside the half-joint gap, it was instrumented with an SHM system at the end of 2021. This system was installed to measure the deformation of the lower nib of the half-joint, and should thereby detect the initiation of a failure mode of this nib. The fibre-optic SHM system consists of 44 inclinometers, 16 displacement sensors, and 24 thermometers, located at support 5 and 6 of the southern bridge. All sensors are located at the bottom of the lower nibs of the half-joints, below the longitudinal girders. The exact locations of the sensors can be found in Figure 3.7.

Figure 3.8 shows the placement of the measurement sensors at a location where all three sensor types are present. As can be seen, the inclinometers are mounted directly to the concrete surface at the location of the nib. The displacement sensors are mounted onto a steel rod that extends to the column. In order to account for the temperature effects that might affect the displacement data as a result of thermal expansion of the mounting construction, temperature sensors have been installed on the steel rods. The temperature sensors located below the outer longitudinal girders, where no displacement sensors were installed, are installed directly on the concrete. The sensor layout on supports 5 and 6 of the southern Naardertrekvaart bridge, together with their annotations, can be found in Figure 3.9. The estimated accuracy of the measurement sensors can be found in Table 3.1.

The SHM system takes measurements at a frequency of $10\mathrm{Hz}$, which are temporarily stored. For every $30\mathrm{s}$ of data, the measurements are averaged before uploading to the cloud to reduce memory usage and mitigate the effects of traffic loads on the measurement data. This results in a measurement storage frequency of $\frac{1}{30}\mathrm{Hz}$. With such a low frequency, the data that are stored in the cloud captures mostly the static behaviour of the bridge.

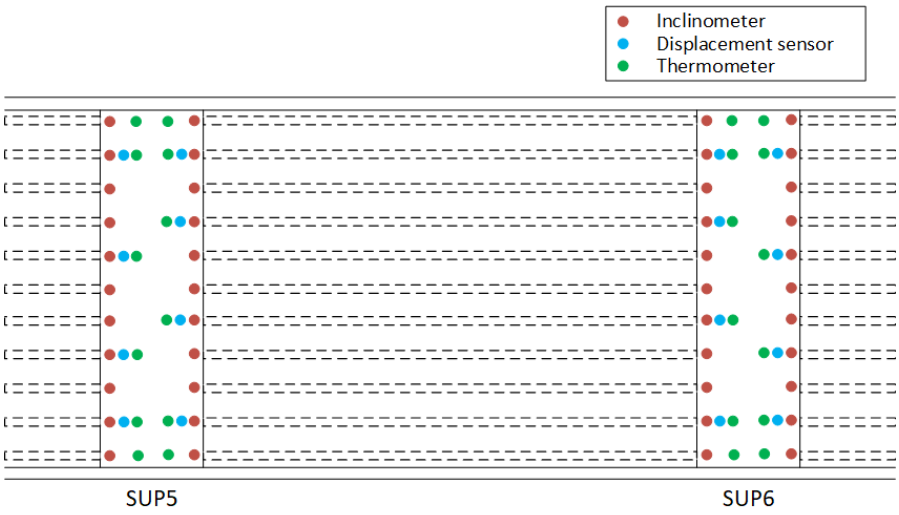

Figure 3.7: Sensor locations of the SHM system on the southern bridge

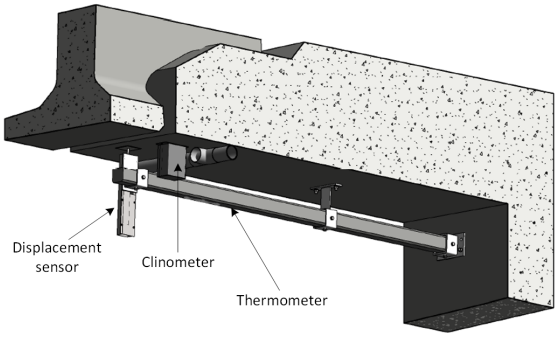

Figure 3.8: Sensor placement of the SHM system [57]

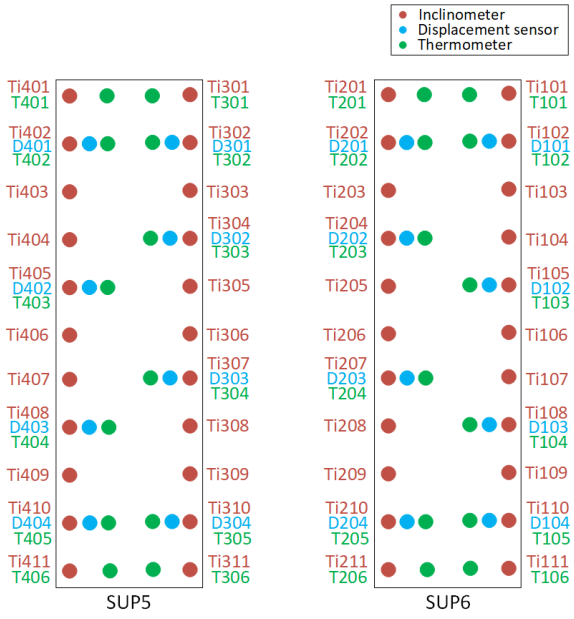

Figure 3.9: Layout and annotation of the SHM system of the Naardertrekvaart

Table 3.1: Estimated accuracy of the measurement data

Sensor	Accuracy
Inclinometer	0.035 mrad
Displacement sensor	0.15 mm
Thermometer	0.5 °C

Analysis of the response of the inclinometers to manual excitation has revealed no natural frequency, indicating that the inclinometers on the bridge can be classified as overdamped.

Based on analysis of the measurement data of the individual inclinometers, an early warning system was implemented, which scans the data that are uploaded to the cloud. This system is intended to capture the occurrence of damage in the lower nib of the half-joint, and is based on the results of a nonlinear plane stress model of a cross section of a support platform. The early warning system has two components.

1. A dynamic component, which checks the data of the inclinometers for deviation from a running average of 10 minutes, with a value of more than $0.087\mathrm{mrad}$. After an initial exceedance, the deviation is again checked at a 30 second delay and at a 30 minute delay. If all deviations exceed the deviation threshold, an alarm is raised. This component should indicate the increase in crack opening width of a diagonal crack at the location of the re-entrant corner.
2. A static component, which checks the data of both the inclinometers and displacement sensors for values outside of their previously measured measuring range.

In the following chapter, over two years of measurement data captured by the SHM system are analysed with the goal of inferring the state of the half-joints.

4

Analysis of the Long-Term Measurement Data

Before the start of this research, the SHM system on the Naardertrekvaart bridge has been gathering measurement data for two years. Due to set-up of this measurement system, which only stores 30s-averages of the measurements, the system captures only the quasi-static behaviour of the bridge. Analysis of this behaviour could indicate the effect could reveal local occurrence of damage. In this chapter, the long-term measurement data is analysed. Additionally, an inference of the structural integrity of the half-joints is performed using numerical modelling and manual calculation, comparing the observed behaviour of the half-joints with predicted behaviour.

4.1. Analysis of Measurement Data

The long-term measurement data of the SHM system on the Naardertrekvaart bridge is prepared for analysis using the preparation procedure described in Appendix C.1.

4.1.1. Analysis of Measurement Data of Individual Sensors

Figure 4.1 shows the behaviour of the measurement sensors at the eastern and western nib of supports 5 and 6. It shows high variability of behaviour between different inclinometers and displacement sensors located on the same nib. The inclinometer data indicates a notable dependence of the rotation of the nibs on a seasonal cycle, measuring larger rotation of the nibs during summer and lower values during winter.

Analysis of the measurement data of the inclinometers and displacement sensors reveals the presence of a significant linear trend in multiple sensors. The magnitude and direction of the trends is depicted in Figure 4.2 for the measurement sensors at different locations along the support platforms.

The variance of the measurement data of the different sensors can be quantified using box plots of the sensors' deviation from their linear trend. Figure 4.3 shows box plots of all measurement sensors, showing the locations of the quantiles of individual sensors. This figure confirms the significant variability in behaviour of individual sensors at different locations along the support platforms. Additionally, sensors that experience a large variation, indicated by a large distance between quantiles depicted in Figure 4.3, tend to exhibit a relatively large downward linear trend. Remarkably, sensor Ti404 seems experiences little variance, while exhibiting a significant downward linear trend. Also, it can be noted that the outer temperature sensors, which are mounted directly onto the concrete, exhibit fewer outliers than the sensors that are mounted on the steel bars and the KNMI temperature sensor. This observation indicates that the sensors mounted on steel bars are more dependent on outside temperature than the sensors mounted on concrete.

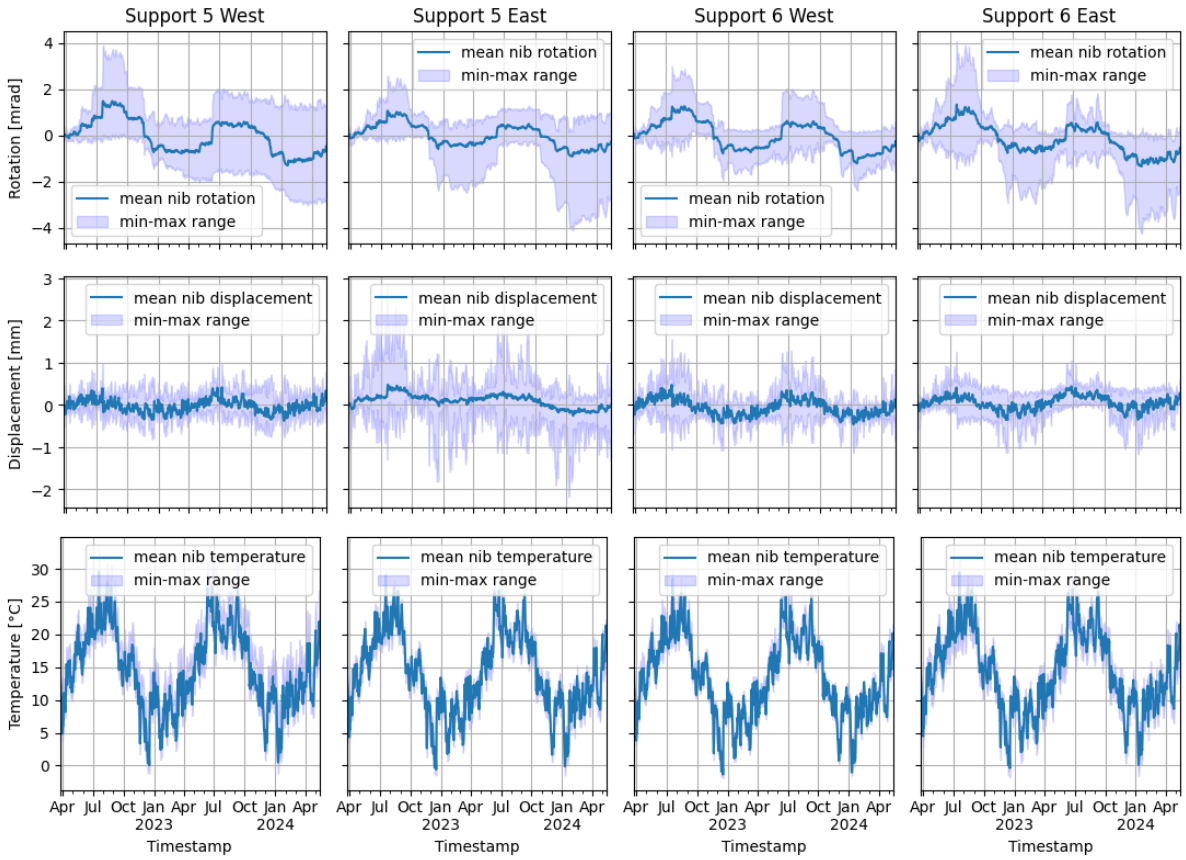

Figure 4.1: Behaviour of the measurement sensors per support side

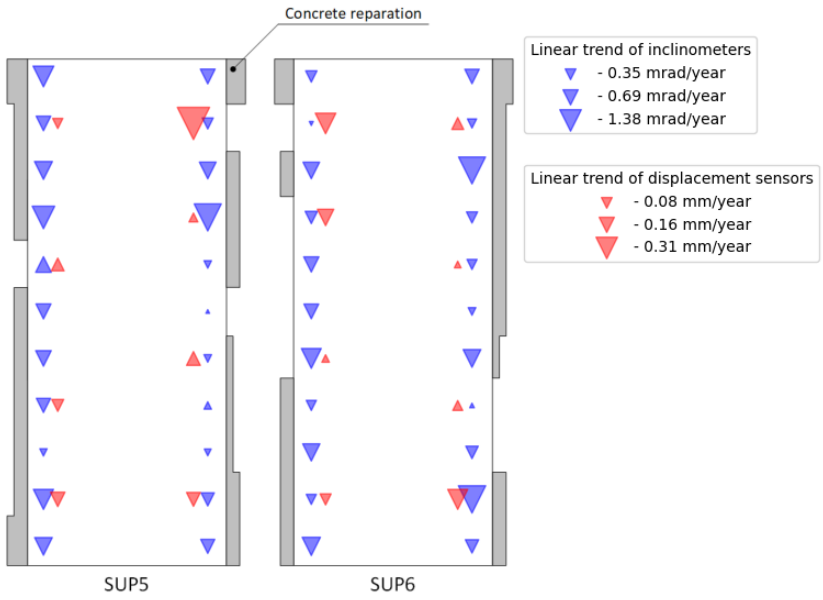

Figure 4.2: Linear trend observed by the measurement sensors, plotted on different locations along the support platforms. The linear trends are calculated using a least squared estimate of a straight line between 01-04-2022 and 01-04-2024.

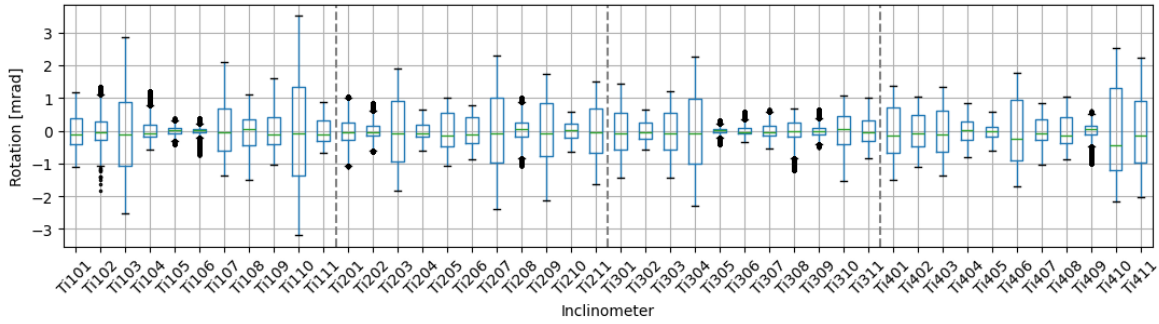

(a) Box plots of inclinometers' deviation from their linear trend

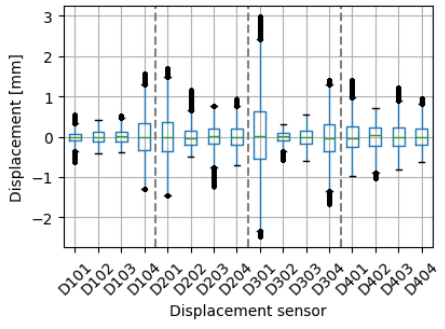

(b) Box plots of displacement sensors' deviation from their linear trend

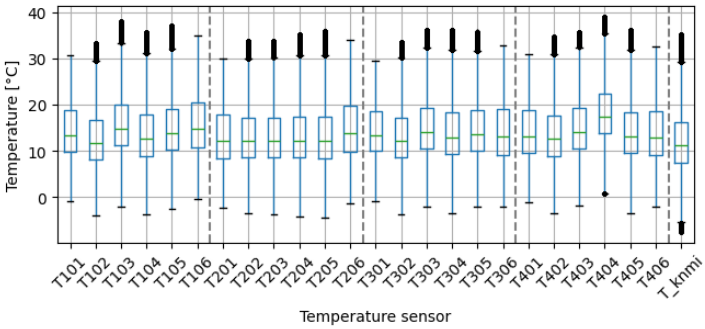

(c) Box plots of temperature sensors

Figure 4.3: Box plots of the measurement sensors

The dependence of the measurement data on periodic influences can be analysed with the power spectral density (PSD). Analysis of the PSD of the different types of sensors, shown in Figure 4.4, reveals a clear dependence on periodic influences. The most significant peak lies at a frequency of approximately $3 \cdot 10^{-8}\mathrm{Hz}$, which corresponds to a period of around 365 days. This peak indicates a considerable dependence of the measurement data on seasonal variations, presumably caused by an annual temperature cycle. A second peak can be observed in the measurement data of the displacement sensors and temperature sensors at a frequency of $1.2 \cdot 10^{-5}\mathrm{Hz}$, which corresponds to a period of around 24 hours. This peak indicates the dependence of the measurements on a daily cycle, possibly caused by the daily traffic cycle or the daily temperature cycle.

Following from the presence of daily cyclic influences on the measurement data, daily fluctuations of the measurement data are analysed. Figure 4.5 shows the mean of the daily behaviour of the measurement sensors per nib. The shape of the minimum-maximum range as plotted in this figure, shows great variance of time and direction of peaks in typical daily measurements of the inclinometers and displacement sensors. The measured fluctuations in rotation and displacement are, at least partly, caused by a combination of daily meteorological cycles and the daily traffic intensity fluctuations. Due to the complexity of the bridge's behaviour under this combined influence, and the unknown effect of damage on this behaviour, daily fluctuations of the deformation measurements are not further investigated.

As described in Section 3.3, an early warning system was implemented in the SHM system, which checks the measurement data for threshold exceedances on multiple levels. The dynamic component of this system gives a warning when the measurement data from an inclinometer contains an exceptional deviation from its running average for multiple measurements in a row. This component is released on the long-term measurement data, with a threshold value of $0.07\mathrm{mrad}$, to find exceptional events that occurred in the past. Figure 4.6 shows all exceedances in the full dataset, with the corresponding temperature and displacement measurements. Analysis of the threshold exceedances reveals most of the sudden rotation changes of the support platform to be associated with a sudden temperature decrease. In most cases, this sudden temperature decrease is only visible in the bridge's

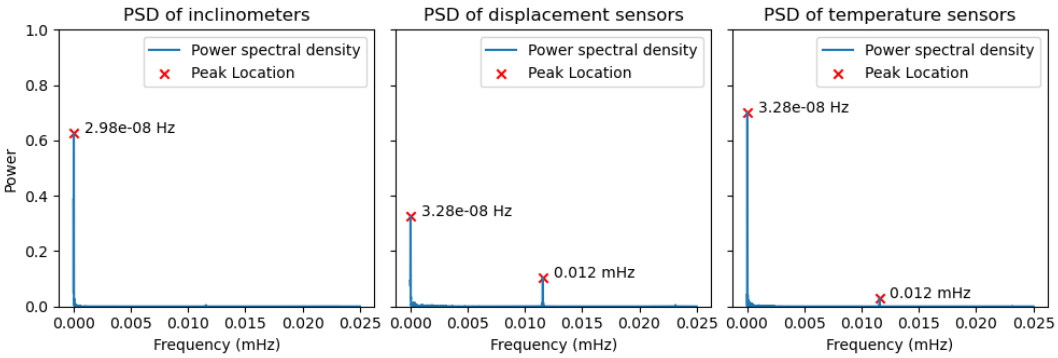

Figure 4.4: Average power spectral density of the different sensor types. Peaks are indicated with red marks.

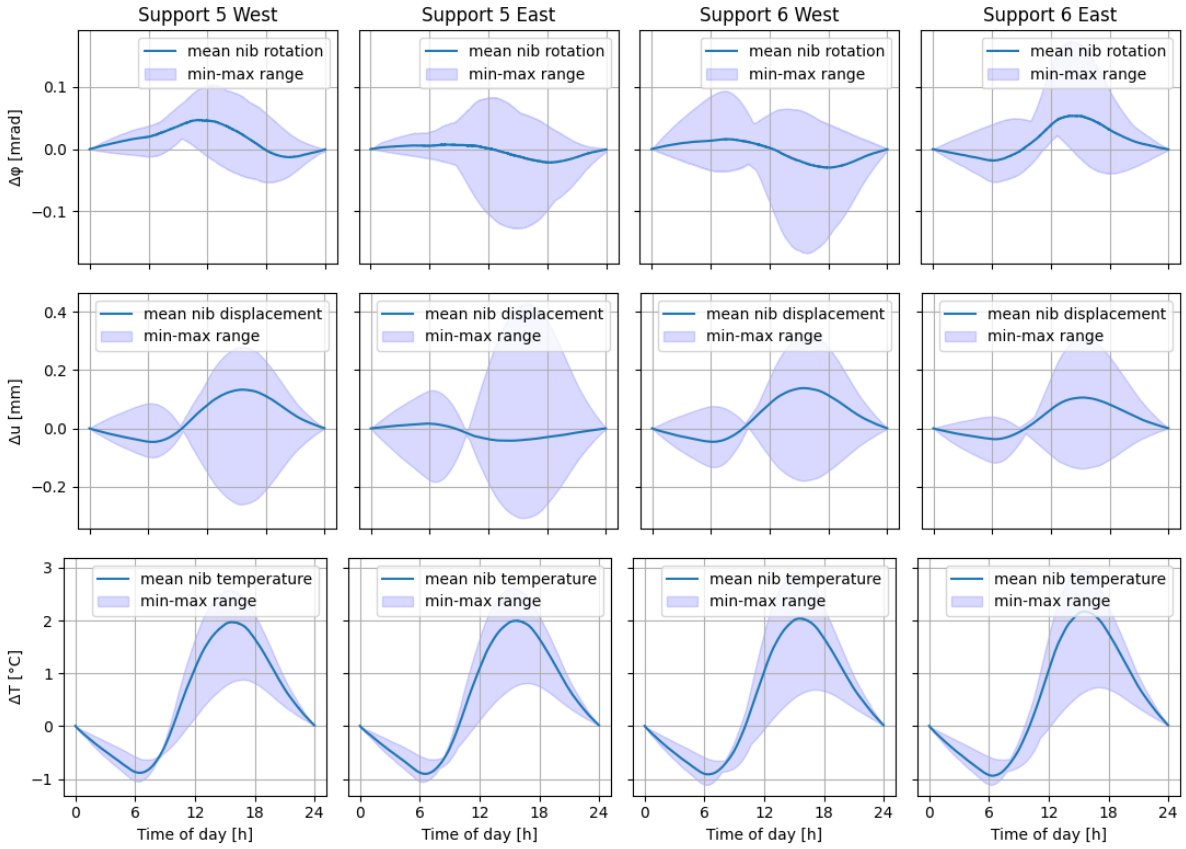

Figure 4.5: Behaviour of the measurement sensors per support side

temperature sensor data, while KNMI measurements remain constant, indicating that the sudden temperature decrease is caused by a local rain shower. One of the threshold exceedances, shown in Figure 4.7, shows no simultaneous temperature change. It occurred on a Tuesday afternoon, close to rush hour, at a temperature close to $0°\mathrm{C}$. The sawtooth pattern observed in the measurement data of multiple sensors could be attributed to the propagation of damage. The location of this possible damage is difficult to determine, as the threshold exceedances occur in inclinometers installed on different nibs and at different locations along the width of the bridge.

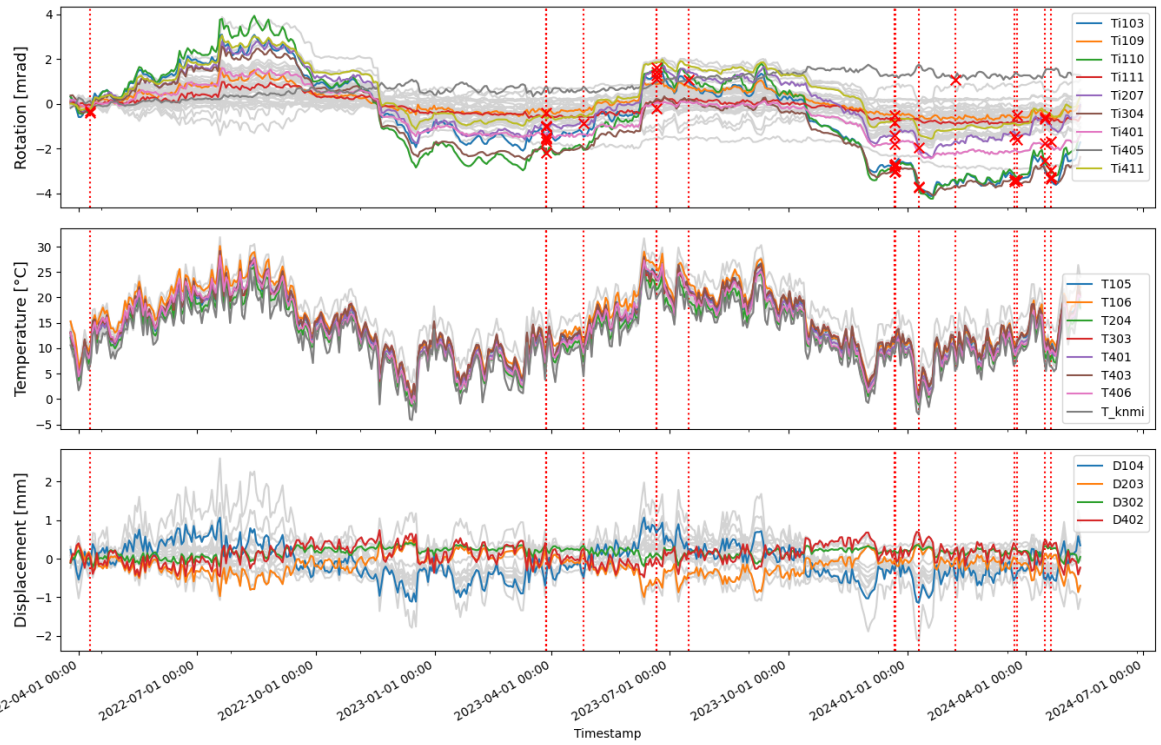

Figure 4.6: Dynamic threshold exceedances in historic data. Times of exceedance are depicted with a red dotted line, and the sensors corresponding to the exceedances are marked with a red cross.

4.1.2. Analysis of Collective Behaviour of the Measurement System

Inter-sensor behaviour is characterised by their correlation. The correlation coefficient indicates the magnitude and sign of the correlation between the measurements of two sensors. It reaches a value close to 1 when sensors seem to behave similarly, reaches a value close to -1 when sensors exhibit inverted behaviour, and is close to 0 when sensors exhibit neither of these characteristics. The correlation coefficients between the measurement sensors on the Naardertrekvaart bridge can be visualised using a correlation matrix. The correlation matrix of the inclinometers is shown in Figure 4.8. Appendix C.4 shows the same correlation matrix for all measurement sensors. The dominantly positive correlation between the inclinometers proves that all instrumented nibs show similar behaviour when analysed globally. Sensors Ti108, Ti201 and Ti305 show exceptional behaviour, having inverse correlation with most other sensors. This odd behaviour can not be explained through data analysis. The structural phenomena causing the seasonal fluctuations, which are discussed in Section 4.2

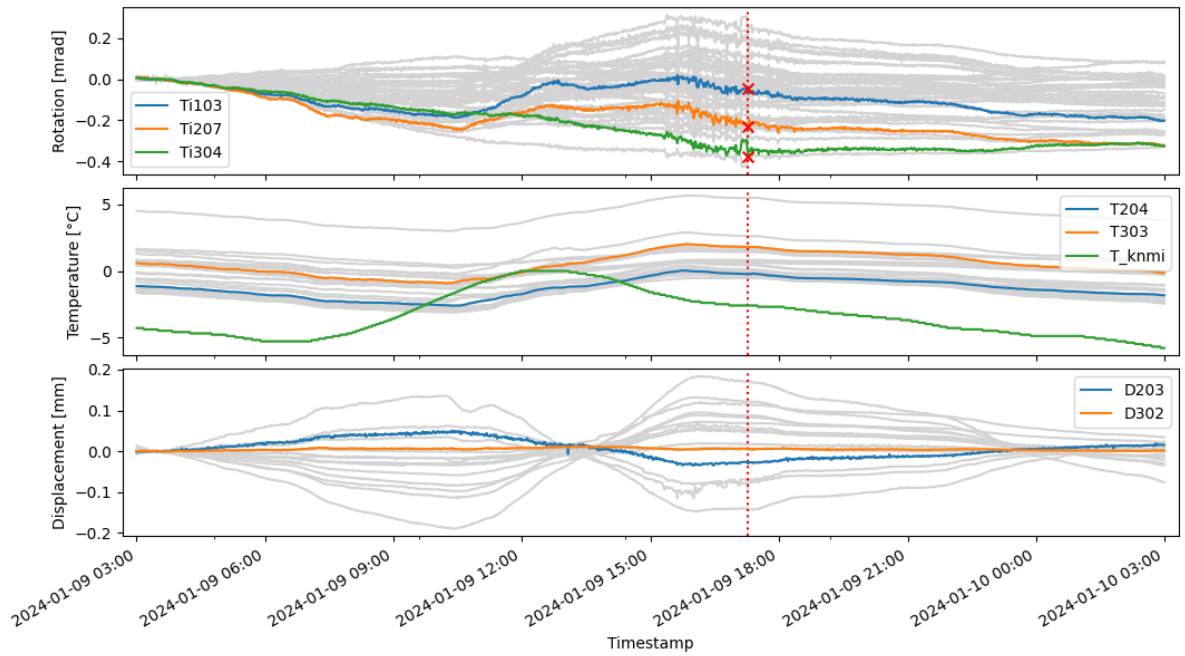

Figure 4.7: Threshold exceedance on 09-01-24. Times of exceedance are depicted with a red dotted line, and the sensors corresponding to the exceedances are marked with a red cross.

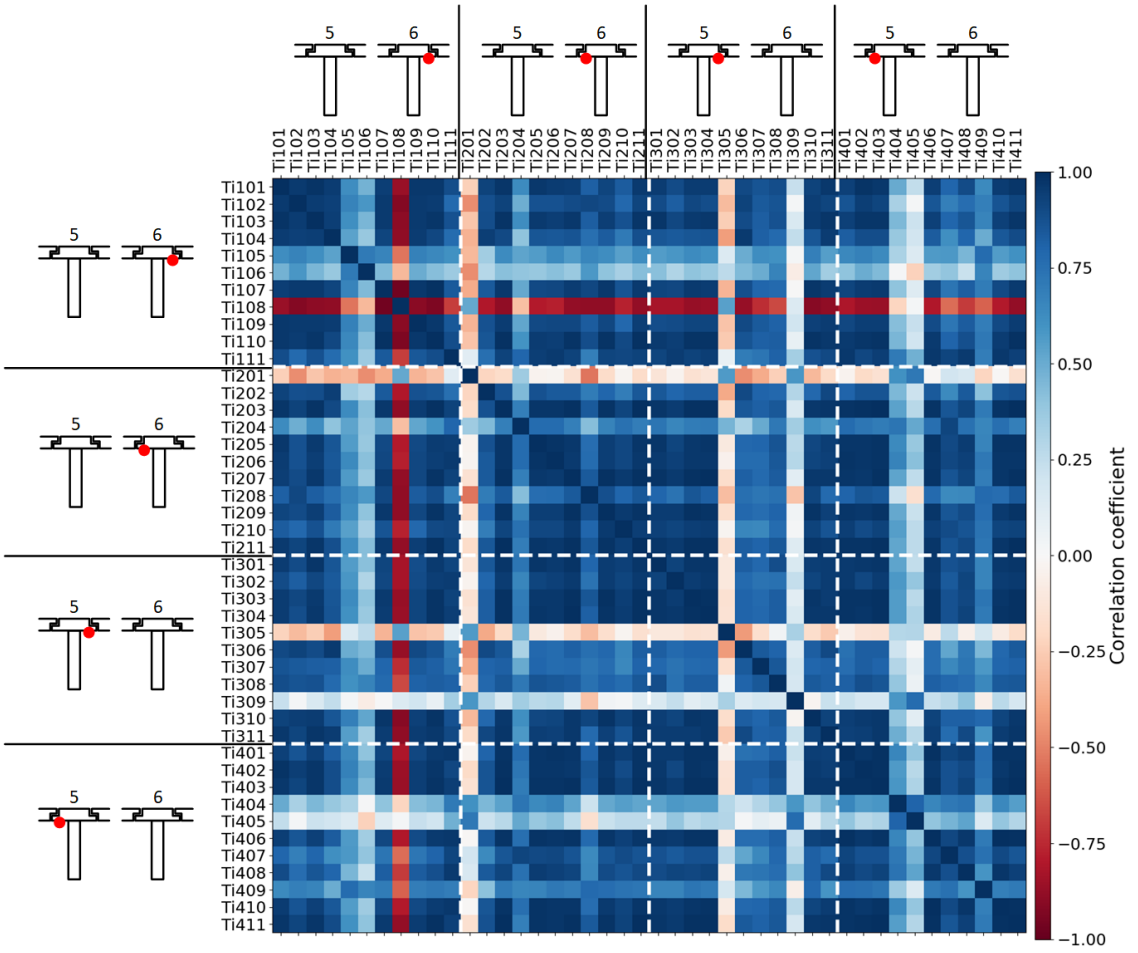

Figure 4.8: Correlation matrix of the inclinometers, showing the calculated values for the Pearson correlation coefficient of the long-term measurement data

4.2. Inference of the State of the Half-joints from the Measurement Data

To infer the structural integrity of the half-joints from the measurement data, the structural behaviour causing the measured deformation needs to be determined. The following sections introduce a possible cause for the measured deformation of the Naardertrekvaart bridge. For each hypothesis, its estimated effect on the deformation of the bridge is compared to the deformation measured by the measurement sensors of the SHM system. This comparison gives an indication of the significance of the hypothesised behaviour in the physical structure. If the hypothesised behaviour seems to be able to explain the measured deformation, the effect of damage to the half-joint on the deformation of the bridge is investigated. By comparison with the observed deformation of the bridge, this last step could offer an indication of the structural integrity of the half-joints.

4.2.1. Bending of the Support Columns due to Gap Congestion in combination with Thermal Expansion

Despite the tendency of joint implementation to cause isostatic behaviour of the spans, congestion of the half-joint gaps is known to cause linked behaviour of the spans [21]. In case of the Naardertrekvaart bridge, a differing degree of gap congestion between the different half-joints could cause the support columns to bend under a horizontal load. This phenomenon is depicted in Figure 4.9. The magnitude of this effect increases as multiple half-joint gaps in a row are congested, but decreases when the horizontal load can be countered by an opposing force from the other side. As a result, the effect is most extreme when gap congestion occurs in one side of the bridge, while the other side allows free expansion of the spans.

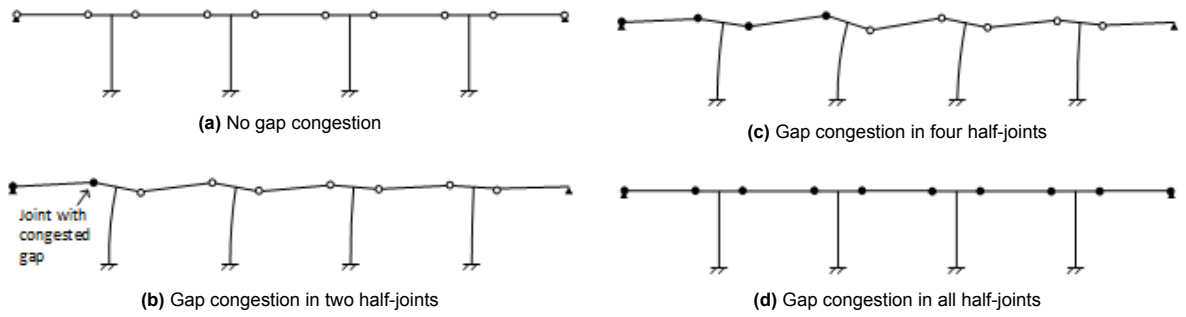

(a) No gap congestion

(c) Gap congestion in four half-joints

(b) Gap congestion in two half-joints

(d) Gap congestion in all half-joints

Figure 4.9: Effect of asymmetric half-joint gap congestion on bridge response to thermal expansion of the structural elements

The linked behaviour of the spans of the Naardertrekvaart bridge is analysed through a numerical model of the full bridge, using 2D plane stress elements, shown in Figure 4.10. Appendix D.2 contains a full description of this numerical model. The model, in its standard condition, has EPS in the top half of the half-joint gaps. In steps, the elastic modulus of the material in the half-joint gaps is increased from the western side of the bridge to the east to a value ten times larger than EPS, while the rest of the material in the half-joint gaps is kept at a standard stiffness. Through this simulation, the stiffness configuration that causes the most extreme bending of the support columns is found. The most extreme bending of the support columns, the ”worst-case scenario”, occurs when all half-joints between the western abutment and support 7 are congested, while the half-joints between support 7 and the eastern abutment contain standard EPS stiffness.

By iteratively increasing the stiffness values of the congested joints of the worst-case scenario, the magnitude of the effect of asymmetric half-joint gap congestion can be found. The expected effect of asymmetric joint gap congestion on the measurement data of the inclinometers, based on the results of the numerical model, can be found in Figure 4.11. The actual measurement data, averaged over the

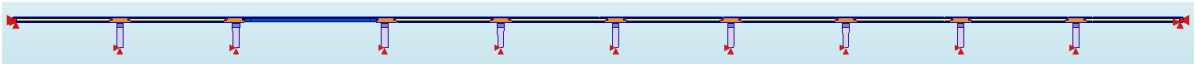

Figure 4.10: 2D plane stress model of the full Naardertrekvaart bridge

width of the bridge, is also shown. Comparison of the simulated and measured rotational data shows that bending of the support column causes realistic rotations at the locations of the inclinometers on one side of support 5 and 6, but does not capture the rotational behaviour on the other side simultaneously. As a result, bending of the support columns does not seem to be a significant cause of the seasonal variations that are visible in the data.

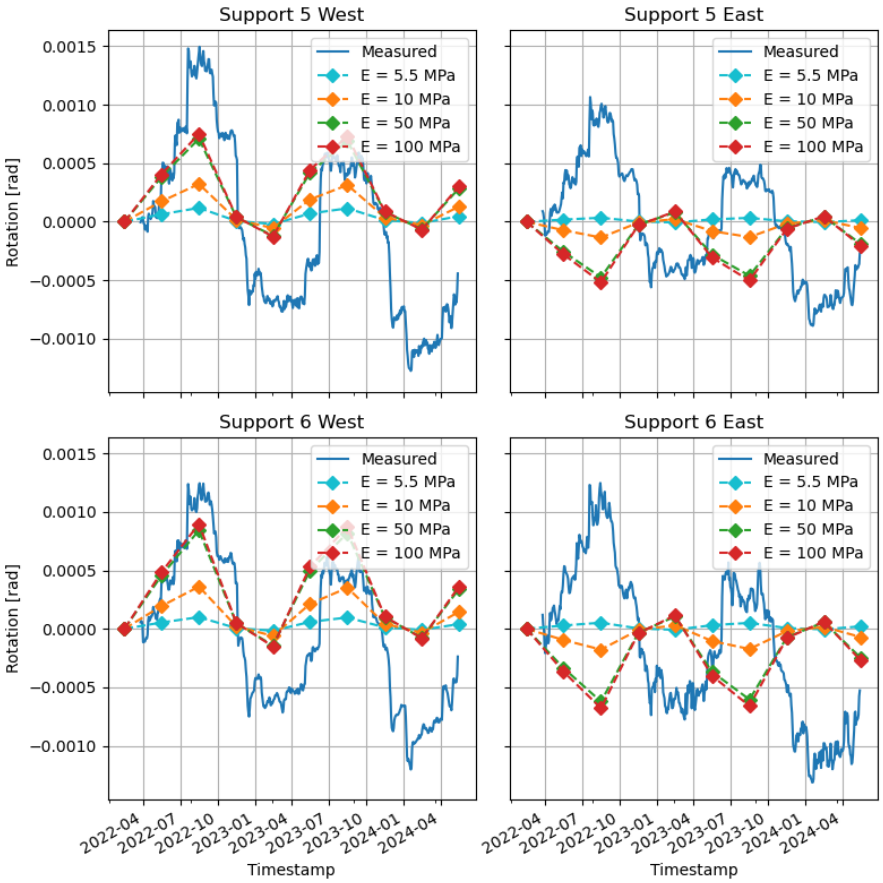

Figure 4.11: Effect of asymmetric joint gap congestion on the rotation of the lower half-joint nib at different elastic modulus values for the joint gap material

4.2.2. Bending of the Support Platforms due to Gap Congestion in combination with Thermal Expansion

Analysis of the seasonal behaviour of inclinometers installed on opposite sides of the support columns reveals that their responses are mainly antithetical, measuring upward rotation of the nibs during periods of high temperatures and downward rotation during periods of lower temperatures. This observation is supported by an analysis of the correlation between the sensors, which shows a mostly positive correlation between all inclinometers.

As inspections indicated the presence of EPS and possibly other materials inside the half-joint gaps, upward bending of the support platforms during periods of higher temperatures could be caused by an eccentric normal force due to hindered thermal expansion inside of the structure. During periods of high temperatures, the compression layers, longitudinal girders, and support platforms are subject to thermal expansion. As EPS is only present in the top half of the half-joint, being used as formwork for the transversal beams, thermal expansion is mostly hindered in the top half of the half-joint. This causes an eccentricity of the resisting force and an upward bending moment inside of the support platform. This phenomenon is depicted in Figure 4.12.

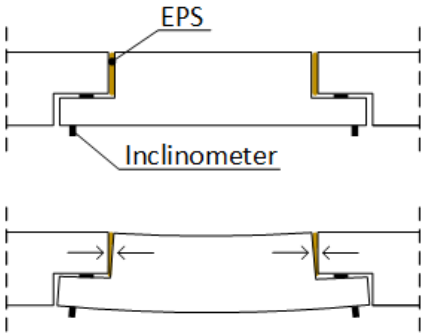

Figure 4.12: Bending of the support platform as a result of thermal expansion

To obtain a reliable estimate of the effect of the eccentric thermal expansion force on the upward bending of the support platforms, a FEM calculation is performed using a numerical model of half a standard span. This model is shown in Figure 4.14. An extensive description of this numerical model can be found in Appendix D.1. Iterating through different values for the elastic modulus of the material present in the half-joint gap yields a better understanding of the behaviour of the bridge under thermal expansion. The magnitude of upward bending of the support is larger when the resultant force of thermal expansion has a higher eccentricity. This eccentricity increases when the gap congestion is more extreme in the top of the half-joint gap than it is in the bottom. To simulate this behaviour, an additional FEM calculation is performed where only the stiffness of the upper half of the half-joint gap is increased. The rotation at the location of the inclinometer due to a temperature difference of 20 °C is shown in Figure 4.13. The results show that congestion occurring only in the top of the half-joint gap has a much larger effect on the rotation at the location of the inclinometers. However, comparison with the measured rotations by the inclinometers in Figure 4.15 shows that upward bending of the support platforms is insufficient to fully explain the seasonal variations of the rotations.

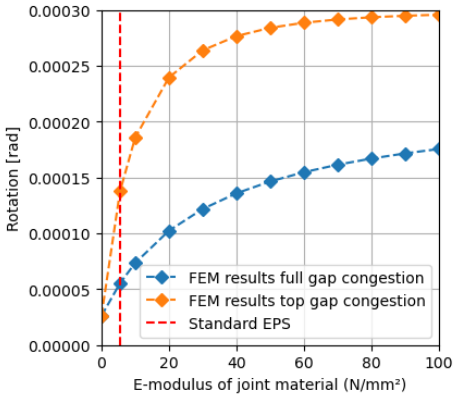

Figure 4.13: Effect of E-modulus of the joint gap material on rotation of at the location of the inclinometer due to upward bending of the support platform, at a temperature increase of 20 °C.

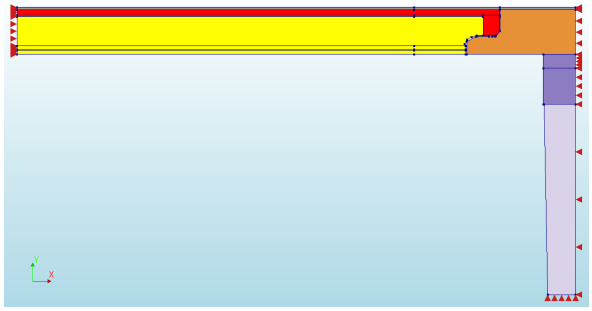

Figure 4.14: 2D model of half a standard span of the Naardertrekvaart bridge

4.2.3. Opening of Cracks in the Re-entrant Corner of the Support Platforms due to Thermal Contraction in combination with Friction Development

Due to thermal contraction of the structural elements of the Naardertrekvaart, the half-joints of the structure have a tendency to expand. In the structure as it was designed, the bearing plates should allow expansion and contraction of the joints without significant resistance. However, in the physical structure, expansion of the half-joints could be significantly hindered by the development of friction forces between the transversal beams and the lower half-joint nibs. In combination with the occurrence of diagonal cracks originating from the re-entrant corner of the support platforms, these stresses could cause the lower half-joint nibs to exhibit a serious drop, as depicted in Figure 4.16. In case of the Naardertrekvaart

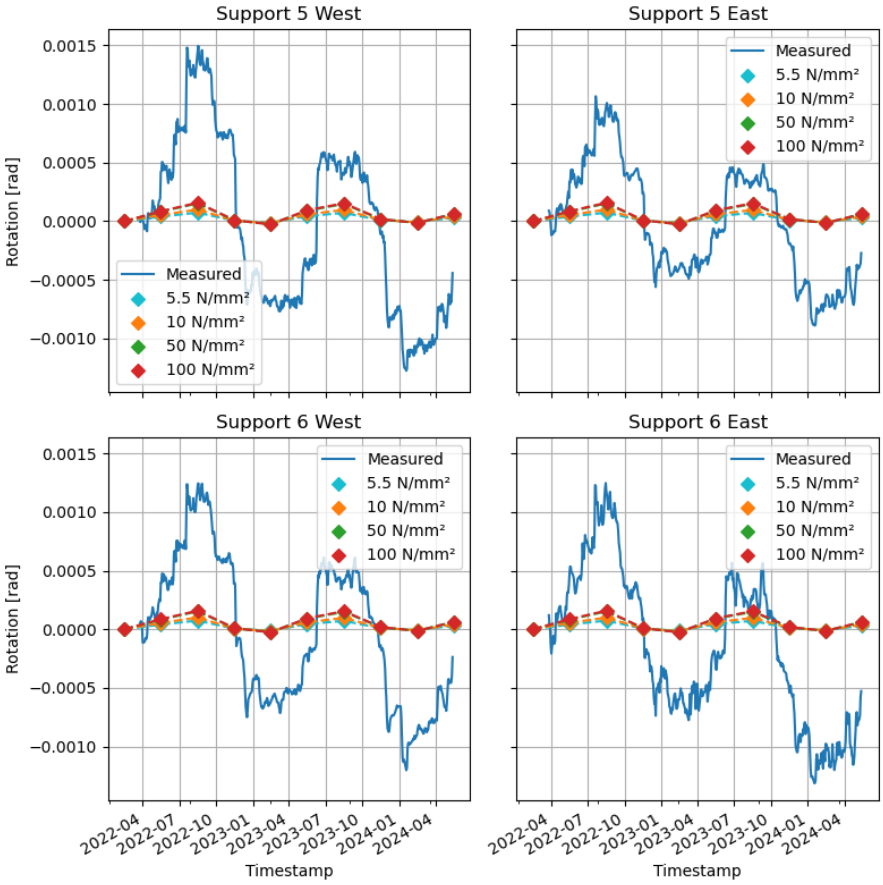

Figure 4.15: Effect of upward bending of the support platforms on the rotation of the lower half-joint nib due to gap congestion, at different values for the stiffness the joint gap material in the top of the upper half-joint gap.

bridge, inspections have indicated corrosion in the reinforcement bars close to the re-entrant corner at several locations along the bridge, presumably caused by exposure of the reinforcement bars due to the occurrence of a crack. Corrosion of the reinforcement bars can reduce their effective diameter, increasing the crack width and further stimulating the drop of the lower half-joint nib. This phenomenon could be the cause of the antithetical behaviour of the sensors installed on opposite sides of the support columns.

The magnitude of nib rotation as a result of a horizontal load due to thermal contraction of the structural elements depends on two main factors. Firstly, it depends on the magnitude of the friction force that can develop between the top face of the lower half-joint nib and the bottom face of the transversal beam. This friction force is influenced by the roughness of the two faces in combination with the perpendicular, vertical stress between them. Secondly, the magnitude of nib rotation depends on the stiffness of the connection between the half-joint nib and the support platform.

The rotational stiffness of the connection between the lower half-joint nib and the platform can be estimated based on a previously performed non-linear FEM calculation by Ingenieursbureau Kok & Van den Heuvel [58]. This calculation investigated the effect of reduction of cross section area of the diagonal reinforcement bars on the deformation of the nib based on a plane stress model of a cross section of the platform. It should be noted that this model takes a very simplified approach to model reality by disregarding any force redistribution ability of the platform over its width. A verification of the model's results has not been achieved. Consequently, the model's results can only be used to give an indication of the magnitude of the friction effect.

By assuming that the cross-section of the FEM model by Ingenieursbureau Kok & Van den Heuvel [58] suffers from formation of a diagonal crack originating from the re-entrant corner and assuming the rotation centre to be at the location depicted in Figure 4.16, the rotational stiffness of the connection can be estimated with Equation 4.1.

$$K_{rot,section} = \frac{M}{\varphi} = \frac{F \cdot e_{load}}{\frac{w_{max}}{e_{max}}} \tag{4.1}$$

where:

$K_{rot,section}$: the rotational stiffness of the nib-platform connection $[\mathrm{Nmm/rad}]$,
M : the bending moment around the rotation centre $[\mathrm{N\,mm}]$,
φ : the nib's rotation around the rotation centre $[\mathrm{rad}]$,
F : the vertical load exerted on the bearing plate of the numerical model $[\mathrm{N}]$,
e_{load} : the eccentricity of the vertical load $[\mathrm{mm}]$,
w_{max} : the resulting vertical displacement at the outer edge of the nib $[\mathrm{mm}]$,
e_{max} : the eccentricity of the outer edge of the nib $[\mathrm{mm}]$.

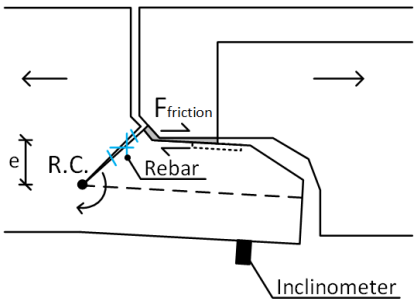

Figure 4.16: Schematic of nib rotation as a result of thermal contraction of the structural elements

The calculated rotational stiffness is valid for a cross section of the platform. The rotational stiffness over the full width of the bridge is necessary for further calculation, and can be obtained with Equation 4.2.

$$K_{rot,full} = K_{rot,section} \cdot \frac{W_{full}}{W_{c/c}} \tag{4.2}$$

where:

W_{full} : the full width of the bridge $(20000\mathrm{mm})$,
$W_{c/c}$: the centre-to-centre distance of the reinforcement $(204\mathrm{mm})$.

The numerical calculations by Ingenieursbureau Kok & Van den Heuvel [58] determine the response of the platform at three different stages of reinforcement corrosion. The effect of corrosion of these reinforcement bars is taken into account by adapting the cross-section area of the embedded bars. The calculated values for the rotational stiffness of the connection between the nib and the support platform for different diameters of the reinforcement bars can be found in Table 4.1.

Table 4.1: Rotational stiffness of the connection between the nib and the support platform at different diameters of the reinforcement bars

ø [mm]	$K_{rot,section}$ [Nmm/rad]
25	$8.420 \cdot 10^9$
20	$5.734 \cdot 10^9$
16	$3.944 \cdot 10^9$

The horizontal friction force that develops between the transversal beam and the lower half-joint nib can be calculated based on horizontal equilibrium. When calculated over the full width of the bridge, elongation of the span and platform can be calculated with Equations 4.3 and 4.4.

$$\Delta L_i = \epsilon_{tot,i} \cdot L_i \tag{4.3}$$

$$\epsilon_{tot,i} = \epsilon_T + \epsilon_{resist,i} = \alpha_c \Delta T + \frac{F_{friction}}{A_i E_c} \tag{4.4}$$

where:

ΔL_i : the elongation of the element $[\mathrm{mm}]$,
$\epsilon_{tot,i}$: the strain of the element $[-]$,
L_i : the length of the element $[\mathrm{mm}]$,
α_c : the thermal expansion coefficient of concrete $[\mathrm{K}^{-1}]$,
ΔT : the temperature difference $[\mathrm{K}]$,
$F_{friction}$: the developed frictional force between the horizontal faces $[\mathrm{N}]$,
A_i : the cross-sectional area of the element $[\mathrm{mm}^2]$,
E_c : the elastic modulus of concrete $[\mathrm{N/mm}^2]$.

The joint expansion can then be calculated with Equation 4.5.

$$\Delta u = -\Delta L_{span} - \Delta L_{platform} \tag{4.5}$$

Assuming there is no slip between the contact faces between the lower half-joint nib and the transversal beams, the joint expansion Δu causes a rotation of $\frac{\Delta u}{e}$ in the connection between the nib and the platform. The resisting moment of this connection can then be calculated with Equation 4.6.

$$M_{rot} = K_{rot,full} \cdot \frac{\Delta u}{e} \tag{4.6}$$

Substituting Equation 4.3-4.5 in Equation 4.6 and calculating moment equilibrium around the rotation centre of the lower half-joint nib, Equation 4.7 is obtained.

$$\frac{K_{rot,full}\left(-\left(\alpha_c \Delta T + \frac{F_{friction}}{A_{span}E_c}\right) L_{span} - \left(\alpha_c \Delta T + \frac{F_{friction}}{A_{platform}E_c}\right) L_{platform}\right)}{e} = F_{friction} \cdot e \tag{4.7}$$

Solving Equation 4.7 for $F_{friction}$, the horizontal friction force is equal to Equation 4.8.

$$F_{friction} = -\frac{K_{rot,full}\alpha_c \Delta T \left(L_{span} + L_{platform}\right) A_{span} E_c A_{platform}}{A_{span}E_c A_{platform} e^2 + A_{span} K_{rot,full} L_{platform} + K_{rot,full} L_{span} A_{platform}} \tag{4.8}$$

The friction resistance between the two faces can be estimated based on the static friction coefficient μ between the two faces and the self-weight load of the span F_{normal}. The maximum friction force can be calculated with Equation 4.9.

$$F_{friction,R} = \mu \cdot F_{normal} \tag{4.9}$$

Eurocode 2 [59] prescribes the assumption of a friction coefficient of 0.60 for a smooth contact surface, while experimental data estimate values closer to 0.80 [60]. This coefficient can rise to values up to 2.00 for roughened surfaces. Comparing the developed friction force over the temperature decrease of the structure, the plot in Figure 4.17 is obtained. The figure shows that the developed friction force in the structure exceeds the friction resistance of the structure at quite low temperature decreases, even with a high friction coefficient in combination with a low reinforcement diameter.

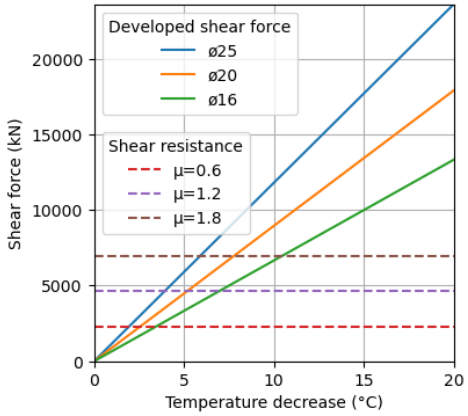

Figure 4.17: Development of friction force due to a temperature decrease at different reinforcement bar diameters

When the horizontal friction force exceeds the maximum friction resistance between the two faces, the faces slip. In case of slip over the full width of the bridge, this slip would cause a sudden jump in the rotation of the lower half-joint nib, in opposite direction of the local trend. Such a jump is not observed in the measurement data of the inclinometers. However, due to local variation of the vertical force and friction between the two surfaces, slip could occur locally and gradually over time. This type of slip would exhibit multiple jumps in the rotation of the nibs that are less significant. Figure 4.18 shows the expected effect of the friction force between the two faces, in case no slip would occur. The used values for every parameter is included in the caption.

The plots in Figure 4.18 indicate that friction between the horizontal faces without slip generates forces that are capable of causing seasonal fluctuations of the nib rotation that exceed the observed rotation. The plots also show that the reduction of cross section area of the reinforcement has little effect on the magnitude of the rotation of the lower half-joint nib. Local and gradual slip would have a diminishing effect on the magnitude of nib rotation, but the magnitude of this reduction depends on many factors and is yet unknown. Possibly, in combination with this local and gradual slip, friction development is able to cause the observed seasonal fluctuations of the nib rotation. However, this phenomenon is not able to explain the divergent behaviour of sensors Ti108, Ti201 and Ti305 described in Section 4.1.2.

As this phenomenon is likely to be one of the causes of the seasonal fluctuations of the rotation of the nibs, it provides an opportunity of inferring the structural integrity of the half-joints. Assuming that this phenomenon is the only cause of the yearly fluctuations in the measured rotation, an estimation of the resulting crack width of a diagonal crack originating from the re-entrant corner can be made at different locations along the width. In this estimation, rotation at the location of the nib is assumed to occur only due to crack opening, and the effect of bending of the support platform is neglected. Assuming the crack in the platform at the location of an inclinometer to be closed during summer when the highest measurement is taken, the maximum rotation taken up by the crack is equal to the inclinometers' largest difference in rotation measurement. Figure 4.19 shows the calculated values for the crack width opening at the location of the re-entrant corner, at the location of each inclinometer. Some

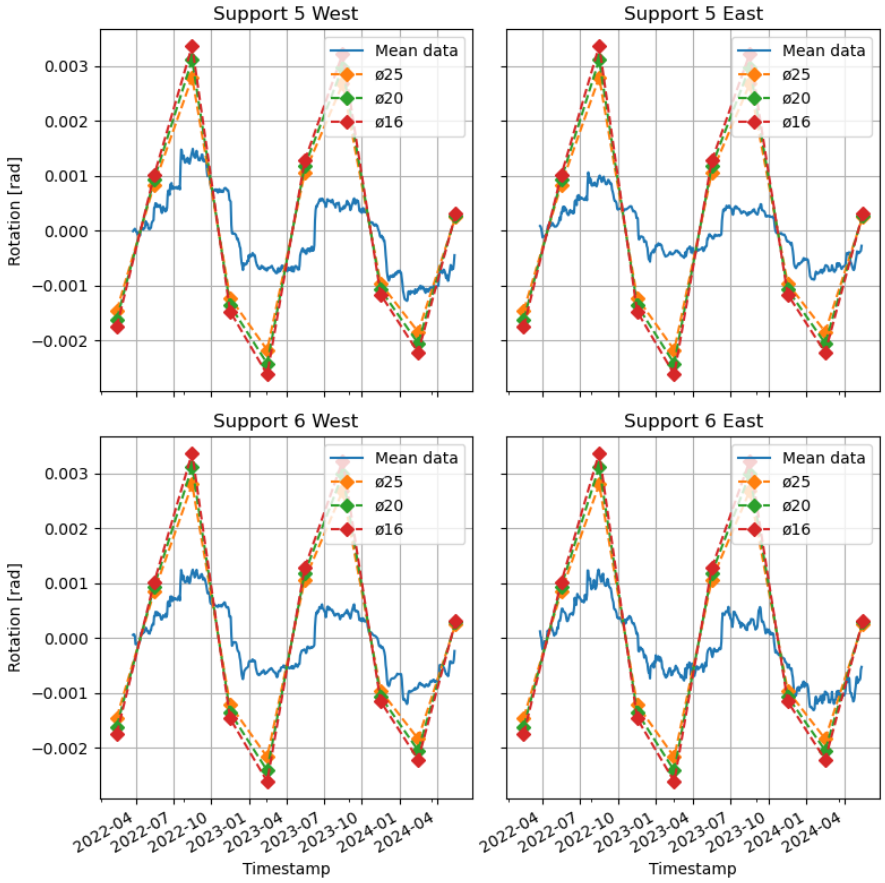

Figure 4.18: Effect of a developed friction force between the contact faces of the transversal beams and the lower half-joint nibs, under the assumption of no friction slip. Used parameters: $\alpha_c = 1 \cdot 10^{-5}\mathrm{K}^{-1}$, $L_{span} = 14000\mathrm{mm}$, $A_{span} = 9599236\mathrm{mm}^2$, $L_{platform} = 2200\mathrm{mm}$, $A_{platform} = 27400000\mathrm{mm}^2$, $E_c = 35000\mathrm{MPa}$, $e = 277.5\mathrm{mm}$.

sensors experienced their maximum downward rotation under a relative temperature increase. As the proposed hypothesis can not explain this behaviour, the crack opening estimation is not accurate, and the corresponding bars are excluded from the figure.

The predicted crack width opening takes extremely large values, exceeding not only the maximum allowed crack width in the Netherlands of $0.2\mathrm{mm}$ [61], but reaching values at which the reinforcement steel would have already fractured. Additionally, friction development is not able to explain the seasonal fluctuations of the measurements of multiple inclinometers. It can be concluded that the analysis of the long-term measurement data does not provide reliable indicators of the structural integrity of the half-joints, caused by the dependence of the data on many unknowns. Analysis of high-frequency measurement data enables the inspection of the oscillatory behaviour of the bridge caused by traffic loads. This behaviour could be more affected by damage to the half-joints, giving more insight into their structural integrity.

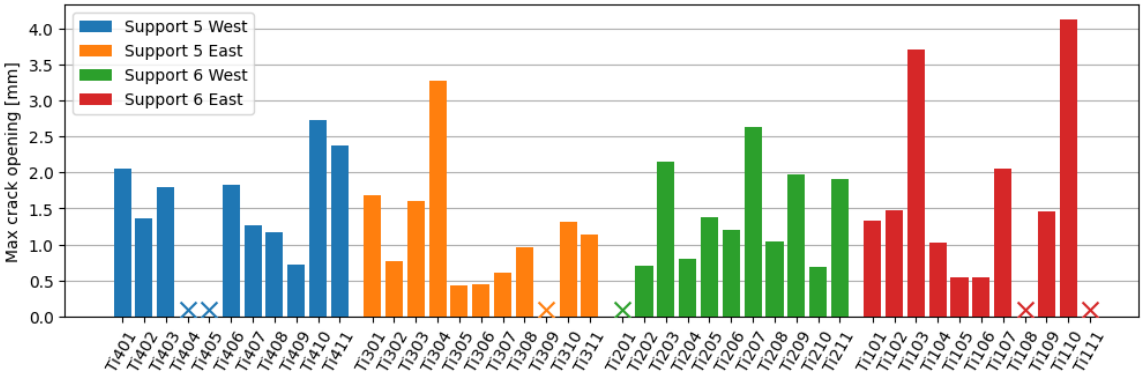

Figure 4.19: Estimated crack width opening due to friction development

5

Analysis of High-Frequency Measurement Data

In the previous chapter, the long-term measurement data of the SHM system on the Naardertrekvaart bridge were analysed and used to make an estimation of the structural integrity of the bridge's half-joints. As this investigation provided unreliable predictions of the state of the joints, in this chapter an investigation on one day of high-frequency measurement data of the SHM system is described. In section 5.1, an extensive analysis of the high-frequency measurement data is described. Next, in Section 5.2, the response of the bridge to traffic loads is used to infer the structural integrity of the half-joints.

5.1. Analysis of Measurement Data

Before analysis, the high-frequency measurement data of the SHM system are prepared for analysis using the preparation procedure described in Appendix C.1. First, the measurement data of individual sensors are analysed as described in Section 5.1.1. Next, in Sections 5.1.2 and 5.1.3, the two separate phenomena causing the observed rotation are extracted from the data.

5.1.1. Analysis of Measurement Data of Individual Sensors

Analysis of the high-frequency measurement data reveals behaviour of the bridge that was averaged out in the long-term measurement data. Figure 5.1 shows the measurement data of sensor Ti101 in both datasets. The figure shows that the measurement range of the high-frequency dataset is much larger than the measurement range of the long-term dataset. Comparison of the standard deviation of the high-frequency measurement data with the measurement range visible in Figure 5.1, shows that the dataset contains many outliers. Analysis of the histograms of the two datasets for every inclinometer, attached in Appendix C.2, confirms that, although the high-frequency measurement dataset has a larger measurement range, its standard deviation is much smaller for most inclinometers.

The power spectral density (PSD) of the high-frequency measurement data is analysed to detect dominant frequencies in the measured vibrations. All PSD plots of the inclinometers exhibit a peak around $2.2\mathrm{Hz}$, which is also visible in the average PSD of all inclinometers, depicted in Figure 5.2. Appendix C.3 contains the PSD plots of all individual inclinometers. Repetitive traffic loading at a constant frequency could cause a peak in the power spectral density, but with a maximum intensity of a maximum of 5000, this would not be able to cause a significant peak above $1.4\mathrm{Hz}$. Therefore, it must originate from vibrations in a natural frequency. The origin of this natural frequency is further investigated in the following sections.

Analysis of the inclinometer correlation of the high-frequency measurement data reveals a similar pattern as the inclinometer correlation of the long-term data. The correlation matrix, visualised in Figure 5.3, shows positive correlation between inclinometers located on the same half-joint nib, indicating collective rotation of these sensors. In addition, the correlation matrix shows negative correlation between

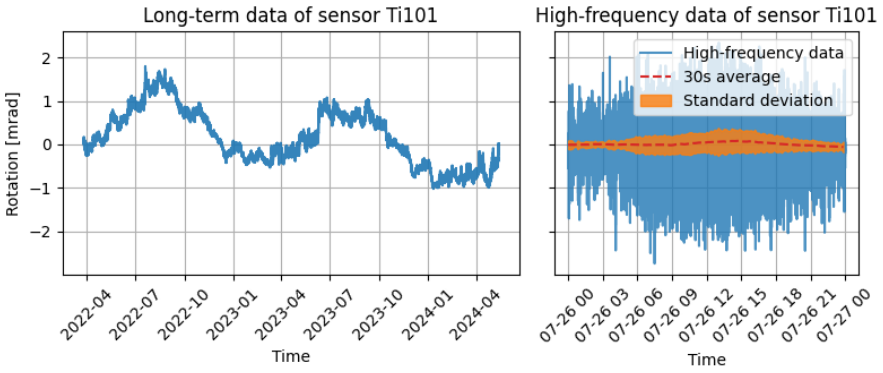

Figure 5.1: Comparison of the measurement data of sensor Ti101 in the long-term dataset and the high-frequency dataset

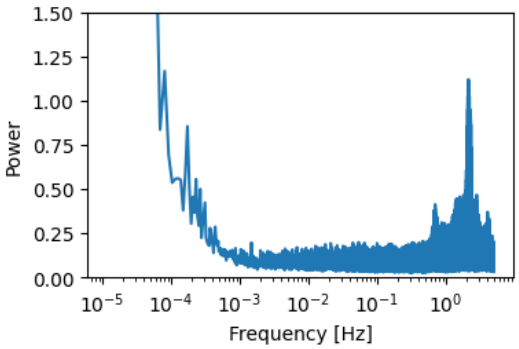

Figure 5.2: Average power spectral density of all inclinometers

inclinometers located on the western and eastern side of a support, indicating that downward rotation of one nib generally corresponds to a simultaneous upward rotation of the nib on the other side of the support. The latter indicates that a significant portion of the measured rotation is caused by rotation of the support platform.

The observed rotation at the location of the nib can arise from the deformation of multiple components of the support, as shown in Figure 5.4. Firstly, the support platforms can rotate entirely under external loads, caused by elastic rotation of the foundation of the platform in combination with bending of the support column. Secondly, external loading can cause torsional rotation of the support platforms around their width axis. Lastly, the inclinometers, located below the lower half-joint nibs, can rotate relative to the support platform, caused by a combination of bending of the support platform and opening of a possible crack in the re-entrant corner. An indication of the structural integrity of the half-joint can only be found in the latter component of the rotation measurements. In pursuit of this indication, the following sections make an estimation of the magnitude of the two components of the measured rotation.

5.1.2. Estimation of Support Platform Rotation

As described above, part of the measured rotation is caused by rotation of the entire support platform in combination with torsional rotation of the support platform. The magnitude of this combined effect is estimated as follows. The average rotation of opposing sensors gives an indication of the local rotation of the support platform. However, this indication is highly dependent on the behaviour of individual sensors. Analysis of this local rotation over the width of the support platform reveals a fairly linear shape over the width of the bridge. Following from this, the local rotation of the support platform is approximated using a least squared estimate of a linear line through the local rotation of the support platform data points. This least squared estimate contains two variables, both containing different information about the origin of the rotation.

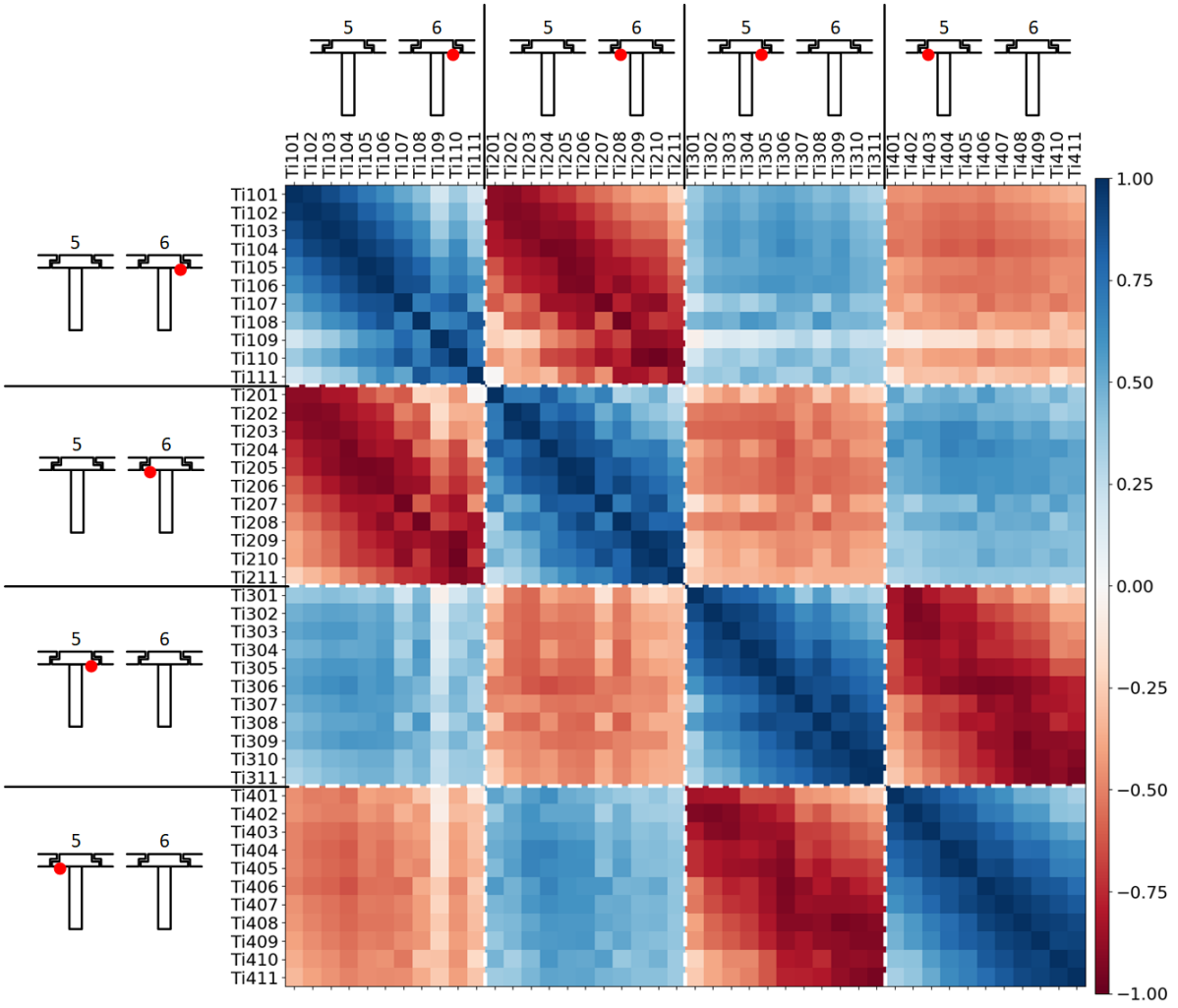

Figure 5.3: Correlation matrix of the inclinometers, showing the calculated values for the Pearson correlation coefficient of the high-frequency measurement data

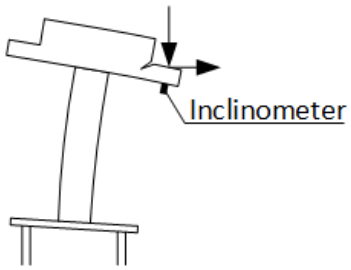

Figure 5.4: Schematic of the effect of deformation of different components of the support on the measurement data of the inclinometers

$$\varphi_{platform} \approx ax + b \tag{5.1}$$

where:

$\varphi_{platform}$: the local rotation of the support platform [rad],
x: the distance of the sensor from the centre of the bridge [m],
b: the rotation of the support platform at the centre of the bridge [rad],
a: the additional local torsional rotation of the support platform [$\mathrm{rad/m}$],
x: the distance of the sensor from the centre of the bridge [m].

Analysis of the PSD of both variables shown in Figure 5.5 reveals that vibrations in the previously observed natural frequency, originate mainly from the rotation of the entire support platform.

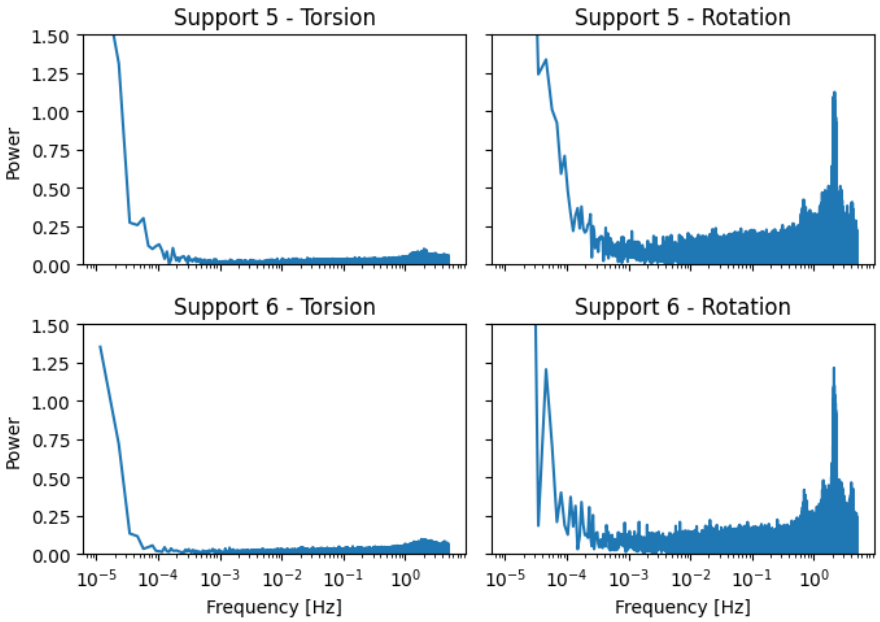

Figure 5.5: Power spectral density of the two components of support platform rotation: rotation at the base of the platform and additional torsional rotation of the platform

5.1.3. Estimation of Rotation of the Nib relative to the Support Platform

Vertical traffic loads exerted on the spanning elements are transferred to the foundation through the half-joints. In undamaged state, the resulting rotation of the lower half-joint nib relative to the support column is solely caused by downward bending of the support platform. The formation of a diagonal crack at the connection between the lower half-joint nib and the support platform, which could have occurred during the lifetime of the bridge, causes additional rotation due to the reduced rotational stiffness of the connection. The magnitude of this rotation could be amplified by reduction of the reinforcement cross section and reduction of bond strength between the reinforcement and the concrete, resulting from corrosion.

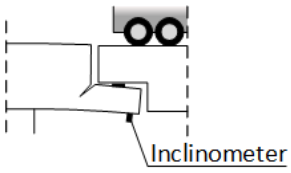

Figure 5.6: Schematic of nib rotation relative to the support column resulting from traffic loads

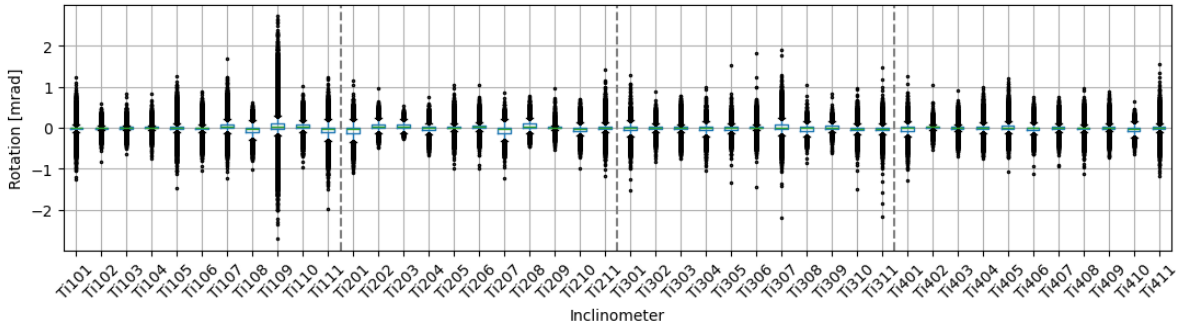

Figure 5.7: Box plots of the rotation of the lower half-joint nib relative to the support platform

By subtracting the estimated effect of rotation of the support platform from the measurement data, an estimation of the rotation of the nib relative to the support platform remains. Figure 5.7 contains box plots of the rotation of the nib by the inclinometers. The box plots show a significant amount of outliers within the measurement data, which can take a variable magnitude across the width of the bridge.

5.2. Inference of the Structural Integrity of the Half-joints from the Measurement Data

The observed high-frequency vibrations of the structure are unaffected by the low-frequency fluctuations of temperature. As a result, analysis of the observed vibrations mitigates the need to quantify the complex effect of thermal expansion or contraction on the measurement data. This simplifies the inference of structural integrity of the half-joints from the measurement data.

The most straightforward approach to estimate the structural integrity of the half-joints of the bridge would be to compare the observed behaviour of the support platform with the behaviour of a numerical model. A non-linear FEM model of a support could be developed, recording the effect of reinforcement corrosion and other degradation mechanisms on the behaviour of the lower half-joint nibs. Due to the complex nature of the support platforms, their behaviour under the progress of damage can only be accurately simulated by a finite element model using solid elements combined with embedded reinforcement. The development of such a model lies outside of the scope of this research. As a result, the effect of progressing damage on the behaviour of the nibs in unknown. This complicates the assessment of the structural integrity of the half-joints.

An indication of the state of the half-joints is achieved with two different methods. The first method uses the response of the nib to daily traffic to generate a stiffness parameter, which could serve as an indicator of the degree of damage. The second method uses the observed response of the nibs to extreme traffic loads to quantify the degree of damage in the structure.

5.2.1. Response of the Nibs to Daily Traffic

The measurement data at different locations across the bridge can be related to each other to find local reductions of stiffness. The local behaviour of the nibs can be characterised by the amplitude of the vibrations ($\hat{\varphi}$) measured by nearby inclinometers. A stiffness indication can be achieved by relating the amplitude of vibrations to the estimated exerted load. The stiffness parameter K is defined as equation 5.2.

$$K = \frac{F}{\hat{\varphi}} \tag{5.2}$$

where:

K : the stiffness parameter [$\mathrm{N/rad}$],
F : the estimated load on the nib [N],
$\hat{\varphi}$: the average amplitude of measured vibrations [rad].

The amplitudes of the rotational vibrations are extracted from the measurement data by subtracting the rotation due to bending of the support columns, and finding peaks in the measurements' deviation from a rolling average of 10 seconds.

The exact loads that are exerted on the bridge are unknown, as the bridge is part of a functioning highway and the weight of passing vehicles is unknown. Hence, an estimation of the load on the lower half-joint nib is estimated using a simulation of a day of traffic. This simulation uses the average traffic intensities per hour of working days in 2023 on the route that crosses the Naardertrekvaart bridge, measured by Rijkswaterstaat. These traffic intensities are split up per vehicle class, and give separate measurements for the main lanes and the exit lane. These intensities are summed to find the estimated total intensity on the bridge, which is depicted in Figure 5.8. The class and their corresponding weight can be found in Table 5.1.

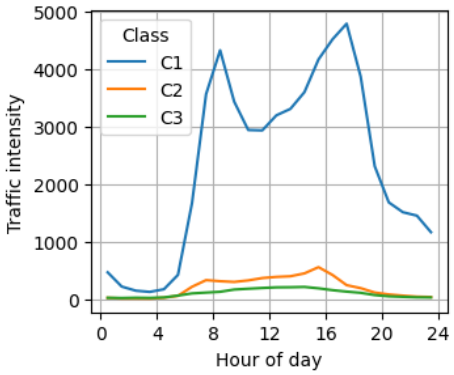

Figure 5.8: Estimated total traffic intensity on the Naardertrekvaart bridge

Table 5.1: Vehicle classes of the traffic intensity measurements

Vehicle class	Weight
C1	Lightweight
C2	Medium-weight
C3	Heavyweight

To estimate the loads that have been exerted on the lower half-joint nib of a span at the time of acquisition of the $10\mathrm{Hz}$ measurement data, a traffic simulation is performed. The Bridge WIM system on the Moerdijkbrug is used to obtain realistic estimations of the characteristics of passing vehicles, like number of axles, axle weight, axle distance and speed. Unrealistic values are filtered from the WIM measurements using the method described in Appendix C.1. Ideally, the vehicles on the Moerdijkbrug would be classified using the same principle as the vehicles on the Naardertrekvaart bridge. However, the traffic intensity estimations by Rijkswaterstaat give no clear description of the classification method. Therefore, the vehicles of the Moerdijkbrug are classified based on the distance between their outer axles, where class C1 has an outer axle distance below $3.5\mathrm{m}$, class C2 has an outer axle distance between $3.5\mathrm{m}$ and $7.5\mathrm{m}$, and class C3 has an outer axle distance above $7.5\mathrm{m}$.

For every hour, for every class, an amount of vehicles equal to the corresponding estimated traffic intensity is sampled from the Bridge WIM measurements. All of these vehicles are given an x-coordinate on the road, which determines its location along the road relative to the middle of a span. The x-coordinates are randomly sampled from a uniform distribution with a lower bound equal to -3600 times the minimum vehicle speed of the corresponding vehicle class in the corresponding hour (in $\mathrm{m/s}$, and an upper bound of 0. This sampling method ensures that all vehicles pass the investigated span within a time span of one hour. Then, the vehicle locations are translated to point loads based on their axle loads and axle distances.

A simulation pushes the point loads over an influence line in time steps of $0.1\mathrm{s}$, which is used to determine which portion of the load goes to one half-joint. This influence is equal to one at the western of end of the span and reduces linearly to zero towards the eastern end of the span, while being zero everywhere else. The influence line is depicted in Figure 5.9.

The relation between the estimated vertical load on the lower half-joint nib and the normalised amplitude of the rotational vibrations of the nib is a measure of the local stiffness of the platform. A locally reduced value for this stiffness parameter is an indicator for damage to the platform. Hourly averaged values of the estimated vertical load and the average amplitude of the rotational vibrations can be plotted against each other to find the relationship between the two parameters. This graph can be found in Appendix

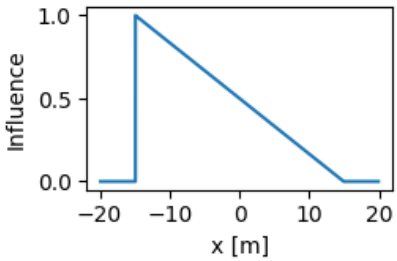

Figure 5.9: Influence line of traffic loads on the vertical load that is exerted on the lower half-joint nib

C.5 for every sensor location. The stiffness parameter is calculated using a least-squares estimate of the slope of a linear line through the data points. Through spatial interpolation of the resulting values for the stiffness parameter over the width of the bridge, the estimated stiffness values along the lower half-joint nibs can be found in Figure 5.10.

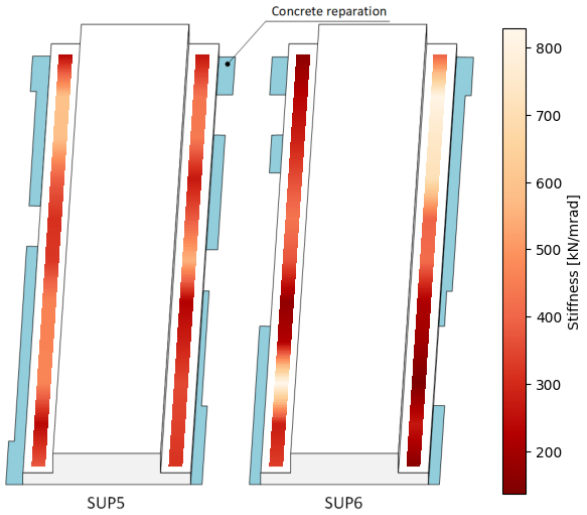

Figure 5.10: Values of the estimated stiffness values of the platform. The blue planes represent the location and degree of reparations that have been done to the concrete of the platform. A locally reduced stiffness is an indication for occurred damage to the platform.

5.2.2. Response of the Nibs to Exceptional Traffic Loads

The structural integrity of the half-joints can also be determined based on the response of the half-joint nibs to exceptional traffic loads. Analysis of the weight data of the WIM system on the Moerdijkbrug shows that on a typical highway in the Netherlands, vehicles with a gross vehicle weight of approximately $50\mathrm{t}$ pass multiple times a day. About 80% of these heavyweight vehicles drive on the right lane.

Multiple exceptional events can be found in the measurement data of the inclinometers. These events caused extreme measured rotations of the nib relative to the support platform, in many different inclinometers. Figures 5.11 to 5.13 show the rotation of the nibs relative to the support platform during three exceptional events. The event displayed on Figure 5.11 was verified to be caused by the passing of a heavyweight dump truck using inspection of the footage of a nearby traffic camera. Consequently, for the purpose of this investigation, it is assumed that the events for which no camera footage was recorded were also caused by the passing of a heavyweight dump truck. This type of vehicle frequently travels on Dutch highways weighing up to $50\mathrm{t}$. The red boxes in the figures indicate the estimated time and location of the passing vehicle. In this estimation, the vehicle was assumed to be travelling at a speed of $23\mathrm{m/s}$ in the right lane. The distance between its outer axles was estimated to be $8\mathrm{m}$, which is typical for dump trucks.

The measurement data show that the passing of a heavyweight vehicle excites vibrations in the nib. As the different events show significantly different behaviour of the half-joint nib, this behaviour seems to be greatly influenced by amplification through resonance by individual axle loads or other vehicles.

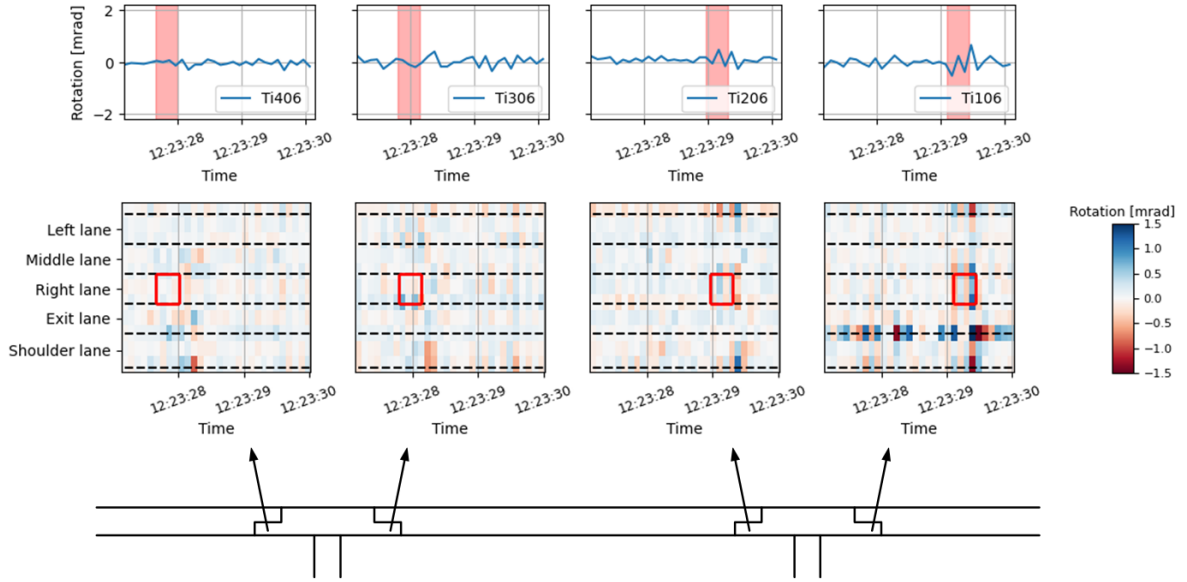

Figure 5.11: The effect of an extreme event at 12:23 on the estimated rotation of the nib relative to the support platform. The red box indicates the estimated time and location of the passing vehicle at each nib.

The rotation of the nibs due to extreme traffic loads indicates that the western nib of support 6 responds more excessively to the same loads, indicating a lower stiffness of the connection between the lower half-joint nib and the platform and thereby a higher degree of damage. Additionally, it can be noted that inclinometer Ti109, located on the eastern side of support 6, observes vibrations with great amplitude, even when neighbouring sensors do not. This vibration sensitivity could indicate local damage of the lower half-joint nib, but could also be caused by inaccurate measurements due to measurement instability of the inclinometer. There is no displacement sensor at the location of this inclinometer to verify the local intensity of vibrations of the nib.

From the extreme events described above, it can be concluded that the passing of heavyweight vehicles of about $50\mathrm{t}$, occurring multiple times a day, can be associated with a rotation of the nib relative to the support platform of approximately $1\mathrm{mrad}$. This is a measure for the remaining stiffness of the half-joint nibs. Comparison of this stiffness to the stiffness of an undamaged support platform gives an indication of the structural integrity of the half-joints.

A numerical model of one support is used to simulate the undamaged behaviour of the support platform. The model is shown in Figure 5.14. An extensive description of the numerical model can be found in Appendix D.3. As can be seen in Figure 5.14, the support is subjected to a vertical force on the lower half-joint nib, at the location of the bearing plate that lies right below the centre of the right traffic lane. A linear analysis is run, recording the rotation at the bottom of the nib right below the vertical load, as well as at the base of the support platform.

The magnitude of the vertical force that a heavyweight vehicle can generate, is determined by multiplying its self-weight with a dynamic amplification factor (DAF). Studies show that for vehicles weighing $50\mathrm{t}$, a realistic value for the DAF is 1.05. This results in a vertical force of $515\mathrm{kN}$.

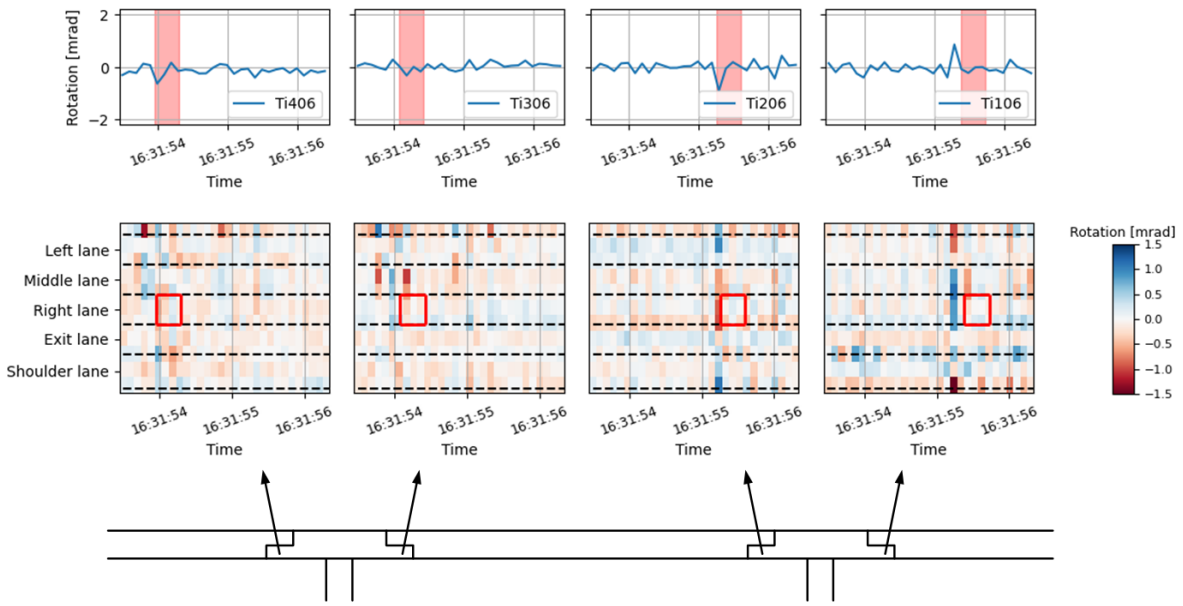

Figure 5.12: The effect of an extreme event at 16:31 on the estimated rotation of the nib relative to the support platform. The red box indicates the estimated time and location of the passing vehicle at each nib.

Figure 5.15 shows the rotation of the half-joint nib relative to the support platform under a progressive vertical load. The figure shows that the measured downward rotation of the lower half-joint nibs is much larger than the simulated rotation. This seemingly lower stiffness could be caused by the existence of a diagonal crack originating from the re-entrant corner of the support platform. However, it could also be caused by multiple other factors. Firstly, the downward force on the nib could be higher than estimated due to resonance caused by individual axle loads or other vehicles. Secondly, by approximation of the torsional rotation of the support platform over the width with a linear line, the rotation of the nib relative to the support platform could be overestimated. Assuming the additional rotation to be fully caused by opening of a crack originating from the re-entrant corner, the maximum width of this crack would be approximately equal to 0.4mm. This crack width would exceed the maximum allowed crack width in the Netherlands of 0.2mm [61]. As the estimation of the crack width of 0.4mm is likely to be an overestimation, it should be considered as an upper bound estimation of the additional crack width due to traffic loads. However, it should be noted that the total width of a possible crack consists not only of the additional crack width due to traffic loads, but also the crack width of a preexisting crack due to static loads, which can not be measured by the current SHM system.

Due to the significant exceedance of the observed rotation of the nib to the predicted rotation by the numerical model, it is reasonable to assume that damage has occurred to the lower half-joint nib at the location of the right lane. The estimated stiffness values shown in Figure 5.10 confirm this conclusion, and indicate that damage could be more severe at locations lying further away from the centre of the bridge.

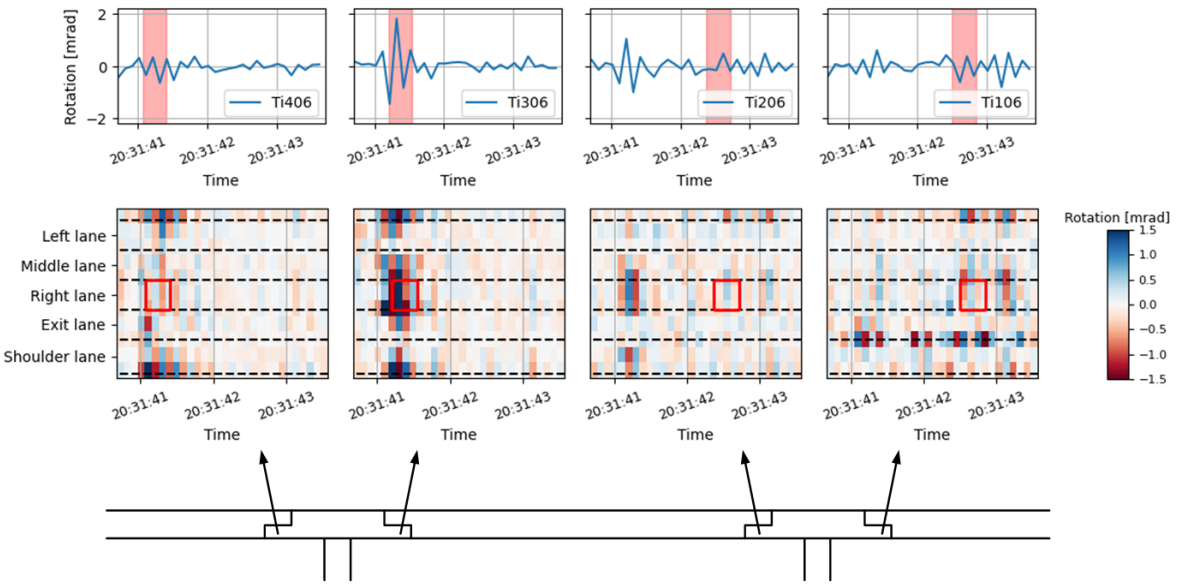

Figure 5.13: The effect of an extreme event at 20:31 on the estimated rotation of the nib relative to the support platform. The red box indicates the estimated time and location of the passing vehicle at each nib.

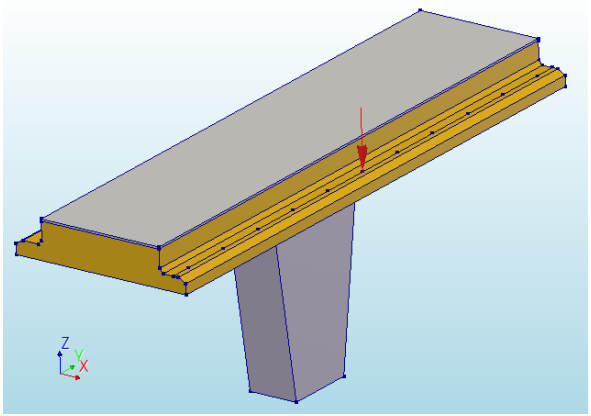

Figure 5.14: 3D solid element model of one support

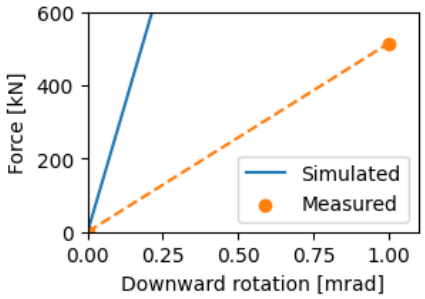

Figure 5.15: Comparison of the measured downward rotation of the nib relative to the support platform with the simulated behaviour

6

Review of the Naardertrekvaart Bridge Monitoring System

This chapter contains a review of the sensor configuration and early warning system that is currently active on the Naardertrekvaart bridge, based on the findings of this research. Section 6.1 gives recommendations on the application of structural health monitoring systems on other half-joint bridges, and Section 6.2 contains a review of the current SHM system and give recommendations on its improvement opportunities.

6.1. Recommendations for SHM Systems on Half-joint Bridges

In this research, the difficulty in identifying the state of half-joint bridges using a structural health monitoring system is indicated. This difficulty evolves from the complex effect of damage on the behaviour of the half-joint nib, along with the strong effect of thermal influences on the deformation behaviour of the bridge. In case of a bridge that contains discontinuous half-joint nibs, the effect of damage on the half-joint's behaviour should prove to be more easily predictable, causing measurement systems based on deformation to be more promising.

Monitoring systems can, however, accurately identify changes in the state of half-joint bridges using changes in oscillatory response. Damage to a structural element can change its natural frequency and magnify the oscillatory amplitudes. This approach needs little understanding of the exact behaviour of the structure and can mitigate the need for development of a digital twin, but is unable to indicate historic occurrence of damage as the oscillatory response of the undamaged structure is difficult to estimate. Changes in the natural frequency of a structure seem to be a good indicator for the occurrence of damage, while for localising this damage, multiple measurement sensors need to be placed at the location of expected damage. Additionally, an increase of oscillatory amplitudes seems to serve well in identifying damage in half-joint bridges, as shown by this research. The measurement of vibrations can be done using many different types of sensors, of which accelerometers are the most conventional. The sensors need to take measurements at a sufficiently high frequency to capture the vibrations of the structure. By using inclinometer sensors to measure the relative rotation of the half-joint nib, the measurement system is not only able to capture changes in oscillatory response, but can also give an indication of the crack width of a possible crack occurring in the re-entrant corner.

Measurements of the oscillatory response of half-joint bridges is well-suited for a data-driven data analysis approach. As a data-driven approach makes the development of a digital twin of the investigated structure unnecessary, it significantly enhances the repeatability of the measurement approach in other half-joint bridges.

Measuring at higher frequencies increases the amount of storage space needed for cloud storage. This problem could be tackled by only periodically storing statistical parameters over a set amount of time, like the mean, standard deviation, minimum and maximum and power spectral density. In addition, the measurement system could store all measurements during a period within which an exceptional measurement was recorded. The measurement data of such an exceptional event could be coupled with a simultaneous image of the road to obtain information on the traffic situation.

6.2. Review of the SHM System of the Naardertrekvaart Bridge

The current monitoring system of the Naardertrekvaart, consisting of inclinometers, displacement sensors and temperature sensors, captures the combined effect of all loads exerted on the bridge. Although the temperature sensors enable estimation of the magnitude of the loads caused by thermal expansion of the structural elements of the bridge, the magnitude of other loads remains unknown. Damage to the half-joint is most easily diagnosed by a local reduction of stiffness, and this stiffness requires a reliable estimation of the exerted load. As a result, the lack of knowledge about the magnitude of individual loads exerted on the bridge complicates the identification of damage. As traffic is the main source of the loads exerted on the bridge, the measurement system would benefit greatly from simultaneous measurements that give a direct indication of the magnitude of traffic loads on the bridge. This could be achieved by installation of a weigh in motion system, or through installation of a camera capturing the highway crossing the bridge. With further investigation, the current sensor configuration might have functionality as a weigh-in-motion system itself.

Damage to the connection between the lower half-joint nib and the support platform is characterised by the rotation of this nib relative to the support. The current set-up of inclinometers captures not only this relative rotation, but also the rotation of the support and the torsional rotation of the support platform along its width. This research displayed the significance of the effect of these additional rotations on the measurement data of the inclinometers, and the difficulty of accurately filtering them out. As a result, the estimated rotation of the lower half-joint nib relative to the support platform remains highly uncertain, causing great uncertainty in the indication of damage. The SHM system would benefit greatly from additional inclinometers at the base of the support platform of the monitored supports at multiple locations across their width, which accurately capture the rotation of the platforms.

The displacement sensors that are part of the monitoring system need to be mounted to a fixed point on the bridge. In case of the Naardertrekvaart bridge, the displacement sensors below the lower half-joint nibs are installed on a metal rod that mounts to the support in two locations. This method of installation presumably caused the extreme dependence on thermal effects along with the large behavioural differences between the sensors. Consequently, the deformation sensors have been disregarded in most parts of this research.

The data acquisition method, which averages the $10\mathrm{Hz}$ data into one data point per $30\mathrm{s}$, could be able to identify a sudden drop of the half-joint nib due to the occurrence of damage to the connection between the nib and the support platform. However, at the time of this research, the effect of damage to this connection on the deformation of the nib is unknown, as it is influenced by complex behavioural factors like the interaction between steel and concrete under possible corrosion and transversal redistribution of forces at the onset of plastic behaviour. As a result, it is unclear whether the occurrence of damage to the support platform has an effect on the acquired measurement data that is distinguishable from the effect of other phenomena.

The early warning system that is active on the monitoring system of the Naardertrekvaart contains a static and a dynamic component, which are described in Section 3.3. This system functions well in finding anomalies in the measurement data. However, after an alarm has been raised, it is difficult to use the measurement data to deduce whether damage has occurred. As sudden deformation of the nibs is often caused by a simultaneous temperature change, warnings could be attributed with a likeliness to be caused by thermal influences, based on the temperature jump that occurred in the past hour.

In addition to the dynamic component of the presently active early warning system, it could be adapted to monitor not only the mean of the rotation measurements, but also other statistical properties like standard deviation and maximum and minimum. To increase accuracy of these statistical properties, the measurement system might benefit from a higher measurement frequency. Due to the fibre-optic nature of the SHM system, enhancement of the measurement frequency only requires adaptation of the interrogation setup. Additionally, the system could store high-frequency measurement data of a time period within which an extreme measurement has been captured.

7

Conclusions

This research aimed to use the structural health monitoring (SHM) system on the Naardertrekvaart bridge to assess the structural integrity of its half-joints, and use it as an early warning system, capturing the occurrence of damage before it becomes critical. This study took a hybrid approach, combining data analysis with the inference of damage using numerical models. The SHM system consists of 44 inclinometers, 16 displacement sensors, and 24 temperature sensors, taking measurement below the lower half-joint nibs of four half-joints in the southern bridge.

A review of existing literature revealed that degradation of the half-joints often occurs in the re-entrant corner of the lower half-joint nib. This degradation consists of the formation of a diagonal crack, which, in combination with seepage of water into the half-joint gap, can cause corrosion of the reinforcement steel. Multiple inspections of the half-joints of the Naardertrekvaart bridge indicated water leakage, indicating that the same degradation mechanism is occurring. The measurement data of the SHM system were analysed to quantify this damage.

Analysis of two years of low-frequency measurement data established the presence of a downward linear trend in most of the inclinometers. Additionally, a dependence of the deformation of the lower half-joint nibs on a yearly cycle was found, rotating upwards during periods of high temperature and downwards during periods of low temperature. Analysis of the correlation between sensors indicated some measurement sensors to behave in an inversed manner. Several hypothesised causes of this behaviour were proposed, and their effect on the behaviour of the lower half-joint nibs was predicted using several custom-built numerical models or manual calculations. The investigations revealed that the yearly fluctuations of the deformation of the lower half-joint nibs are likely caused by friction force development between the nib and the transversal beams, preventing free thermal contraction. Analysis of the low-frequency measurement data provided insufficient possibility to accurately assess the state of the half-joints.

Analysis of 24 hours of high-frequency, $10\mathrm{Hz}$, measurement data of the bridge revealed the clear effect of traffic loads on bridge deformation. A significant portion of the rotation of the nibs under traffic loads originates from rotation of the platforms of the supports as a whole, which could be caused by the combined effect of bending of the support column and rotational elasticity of the underlying foundation. Another portion of the nib rotation originates from torsional rotation of the support platforms, causing a variable rotation of the platform over its width. The remaining portion of the rotation of the nib is its rotation relative to the support platform, which is the portion of the measurement data that gives information about the structural integrity of the connection between the nib and the support platform. The rotation of the lower half-joint nib relative to the support platform of one day of high-frequency measurement data was analysed to find behavioural differences at different locations along the width of the bridge. A first analysis consisted of combining the amplitudes of the rotational vibrations of the nib with the estimated magnitude of the traffic loads, which enabled calculation of a stiffness parameter at different locations along the width. Reduced stiffness could be an indicator of local occurrence of damage. A compelling variation of this stiffness parameter was observed at different locations on

the platforms of the measured supports. The stiffness parameter indicates varying stiffness of the monitored nibs along their width, with a significantly and consistently low value on the southern side of the eastern nib of support 6. A second analysis consisted of comparing the observed response of the lower half-joint nib due to extreme traffic loads with its undamaged behaviour, predicted with a numerical model of a support. This analysis indicated that a crack is likely to exist in the connection between the lower half-joint nibs and the support platforms. An estimation of the width of this crack is highly uncertain, but should be smaller than $0.4\mathrm{mm}$.

This research demonstrated the difficulty of using the current structural health monitoring system on the Naardertrekvaart bridge to identify the structural integrity of its half-joints, due to the complex impact of damage on half-joint nib behaviour and the significant influence of thermal effects on deformation.. This difficulty could be diminished with knowledge of the magnitude of traffic loads on the bridge, or through estimation of the effect of damage on the behaviour of the bridge using a comprehensive solid element model of the support platform. Additionally, it would benefit from accurate measurement of the rotation of the lower half-joint nib relative to the support platform, which contains most information about the state of the connection between the nib and the platform. The monitoring system could also be adapted to take measurements at a higher frequency, which enables analysis of oscillatory behaviour like amplitudes or frequency response. This adaptation does raise the need for cloud storage saving techniques, such as periodic storage of statistical parameters, possibly in combination with occasional storage of the measurement data in the case of an exceptional event.

Monitoring systems on other half-joint bridges could monitor changes in oscillatory response, such as shifts in natural frequency and increased oscillation amplitudes. This approach provides a practical way to detect damage without needing detailed structural understanding or a digital twin. The SHM system could contain multiple sensors at the locations of expected damage. The use of inclinometers provides additional insight into the magnitude of the width of a possible crack. A data-driven approach regarding analysis of the data, improves repeatability of the measurement approach across bridges. The challenge of high-frequency data storage can be addressed by selectively storing key statistical data and exceptional event records, potentially linked to traffic conditions.

8

Discussion and Recommendations

This research aimed to explain the measurement data of the SHM system on the Naardertrekvaart bridge using multiple tools, such as manual calculations, numerical models and traffic simulations. With a very limited amount of publications about the assessment of concrete half-joints using sensor data, this study can be regarded as a preliminary study into an uncharted subject. It gave insight into the behaviour of half-joint bridges due to the seasonal meteorological cycle, as well as the response of half-joint bridges to traffic loads. Moreover, the tools that were developed to give estimations of the damage to the half-joint can provide guidance into the decision making regarding monitoring of other half-joint bridges.

The outcome of this study was a clear indication that damage has occurred to the half-joints in the form of a crack close to the re-entrant corner. The developed tools raised the need for multiple assumptions, causing the results of the analyses to serve only as indications of the cause of the actual behaviour of the bridge. Might there be a need for gaining certainty on the physical behaviour of the bridge that causes the observed deformation behaviour of the bridge, the indications should be followed up with additional measurements of the bridge. To obtain certainty of the accuracy of the proposed indicator of damage to the half-joint nib, damage predictions could be verified using destructive tests at multiple locations along the monitored part of the bridge, intended to find the local degree of damage. Another approach could be to monitor the deformation behaviour of the bridge when subjected to loads of a known magnitude.

Bibliography

[1] Ministerie van Infrastructuur en Waterstaat. Snelweg A1 - Informatie en werkzaamheden. URL http://www.rijkswaterstaat.nl/wegen/wegenoverzicht/a1. Last Modified: 2022-12-27T15:33:28.

[2] Fabrizio Palmisano, Rebecca Asso, Bernardino Chiaia, Giuseppe Carlo Marano, and Carlo Pellegrino. Structural assessment of existing R.C. half-joint bridges according to the new Italian guidelines. *Journal of Civil Structural Health Monitoring*, 13(8):1551–1575, December 2023. ISSN 2190-5452, 2190-5479. doi: 10.1007/s13349-022-00652-7. URL https://link.springer.com/10.1007/s13349-022-00652-7.

[3] Michele Fabio Granata, Davide Messina, Piero Colajanni, Lidia La Mendola, and Elio Lo Giudice. Performance of a historical cantilever reinforced concrete bridge with half-joint degradation. *Structures*, 37:561–575, March 2022. ISSN 23520124. doi: 10.1016/j.istruc.2022.01.039. URL https://linkinghub.elsevier.com/retrieve/pii/S235201242200039X.

[4] Marco Martino Rosso, Rebecca Asso, Angelo Aloisio, Marilisa Di Benedetto, Raffaele Cucuzza, and Rita Greco. Corrosion effects on the capacity and ductility of concrete half-joint bridges. *Construction and Building Materials*, 360:129555, December 2022. ISSN 09500618. doi: 10.1016/j.conbuildmat.2022.129555. URL https://linkinghub.elsevier.com/retrieve/pii/S0950061822032111.

[5] Nobuhiro Chijiwa, Benny Suryanto, and Ryota Kurihara. Forensic analysis of reinforced concrete half-joints. *Technology*, 6(1):216–226, September 2020.

[6] Pieter Desnerck, Janet M. Lees, and Chris T. Morley. Impact of the reinforcement layout on the load capacity of reinforced concrete half-joints. *Engineering Structures*, 127:227–239, November 2016. ISSN 01410296. doi: 10.1016/j.engstruct.2016.08.061. URL https://linkinghub.elsevier.com/retrieve/pii/S0141029616304783.

[7] M Sargious and G Tadros. Stresses in prestressed concrete stepped cantilevers under concentrated loads. Prague, Czech Republic, 1970.

[8] M. P. Werner. Shear Design of Prestressed Concrete Stepped Beams. *PCI Journal*, 18(4):37–49, July 1973. ISSN 08879672. doi: 10.15554/pcij.07011973.37.49. URL https://www.pci.org/PCI/Publications/PCI_Journal/Issues/1973/July-August/SHEAR_DESIGN_OF_PRESTRESSED_CONCRETE_STEPPED_BEAMS.aspx.

[9] A A Hamoudi, M K Phang, and R A Bierweiler. Diagonal Shear in Prestressed Concrete Dapped-Beams. *ACI Journal Proceedings*, 72(7), 1975. ISSN 0002-8061. doi: 10.14359/11140. URL http://www.concrete.org/Publications/ACIMaterialsJournal/ACIJournalSearch.aspx?m=details&ID=11140.

[10] Alan H. Mattock and Timothy C. Chan. Design and Behavior of Dapped-End Beams. *PCI Journal*, 24(6):28–45, November 1979. ISSN 08879672. doi: 10.15554/pcij.11011979.28.45. URL https://www.pci.org/PCI/Publications/PCI_Journal/Issues/1979/November-December/Design_and_Behavior_of_Dapped-End_Beams.aspx.

[11] Denis Mitchell, Jacques Marchand, Paul Croteau, and William D. Cook. Concorde Overpass Collapse: Structural Aspects. *Journal of Performance of Constructed Facilities*, 25(6):545–553, December 2011. ISSN 0887-3828, 1943-5509. doi: 10.1061/(ASCE)CF.1943-5509.0000183. URL https://ascelibrary.org/doi/10.1061/%28ASCE%29CF.1943-5509.0000183.

[12] Marco Di Prisco, Matteo Colombo, and Paolo Martinelli. Structural Aspects of the Collapse of a RC Half-Joint Bridge: Case of the Annone Overpass. *Journal of Bridge Engineering*, 28(11): 05023007, November 2023. ISSN 1084-0702, 1943-5592. doi: 10.1061/JBENF2.BEENG-6063. URL https://ascelibrary.org/doi/10.1061/JBENF2.BEENG-6063.

[13] C S Kleinman. Nokken met die Tanden! *Cement*, 2006-7:56–59, 2006.

[14] C S Kleinman. Nokken met die Tanden! (2). *Cement*, 2007-2:78–80, 2007.

[15] C S Kleinman. Nokken met die Tanden! (3). *Cement*, 2007-3:70–73, 2007.

[16] C S Kleinman. Nokken met die tanden! (4). *Cement*, 2009-1:6–9, 2009.

[17] J. B. Ruijgrok. Load bearing capacity of existing concrete half-joints, February 2023.

[18] D. A. Smith. Refurbishment of the old Medway bridge, UK. *Proceedings of the Institution of Civil Engineers - Bridge Engineering*, 158(3):129–139, September 2005. ISSN 1478-4637, 1751-7664. doi: 10.1680/bren.2005.158.3.129. URL https://www.icevirtuallibrary.com/doi/10.1680/bren.2005.158.3.129.

[19] Sander Pasterkamp. Schade Nelson Mandelabrug: Onderzoeken naar scheurvorming aanleiding tot sluiten van brug over A12 bij Zoetermeer. *Cement: vakblad voor de betonwereld*, 2022, 2022. ISSN 0008-8811. URL https://www-cementonline-nl.tudelft.idm.oclc.org/schade-nelson-mandelabrug.

[20] Yas Gunawardena, Farhad Aslani, Jun Li, and Hong Hao. In Situ Data Analysis for Condition Assessment of an Existing Prestressed Concrete Bridge. *Journal of Aerospace Engineering*, 31(6): 04018106, November 2018. ISSN 0893-1321, 1943-5525. doi: 10.1061/(ASCE)AS.1943-5525.0000935. URL https://ascelibrary.org/doi/10.1061/%28ASCE%29AS.1943-5525.0000935.

[21] Francesco Basone, Alfredo Cigada, Paola Darò, Giulia Lastrico, Monica Longo, and Giuseppe Mancini. Concrete Bridges Continuous SHM Using MEMS Sensors: Anomaly Detection for Preventive Maintenance. In Piervincenzo Rizzo and Alberto Milazzo, editors, *European Workshop on Structural Health Monitoring*, pages 464–473, Cham, 2023. Springer International Publishing. ISBN 978-3-031-07254-3. doi: 10.1007/978-3-031-07254-3_47.

[22] Paola Daró, Isabella Alovisi, Giuseppe Mancini, Monica Longo, Dario La Mazza, and Alfredo Cigada. Dense Sensing on Road Bridges Network: New Approach to Data-informed Assessment. *ce/papers*, 6(5):544–552, September 2023. ISSN 2509-7075, 2509-7075. doi: 10.1002/cepa.2024. URL https://onlinelibrary.wiley.com/doi/10.1002/cepa.2024.

[23] I. Alovisi, A. Cigada, D. La Mazza, and M. Longo. Bridges continuous dense monitoring network: A framework to support the infrastructures assessment and management process. In *Bridge Safety, Maintenance, Management, Life-Cycle, Resilience and Sustainability*. CRC Press, 2022. ISBN 978-1-00-332264-1. Num Pages: 9.

[24] Silvia Bianchi, Fabio Biondini, Gianpaolo Rosati, Mattia Anghileri, Luca Capacci, Gabriele Cazzulani, and Lorenzo Benedetti. Structural Health Monitoring of Two Road Bridges in Como, Italy. In Carlo Pellegrino, Flora Faleschini, Mariano Angelo Zanini, José C. Matos, Joan R. Casas, and Alfred Strauss, editors, *Proceedings of the 1st Conference of the European Association on Quality Control of Bridges and Structures*, Lecture Notes in Civil Engineering, pages 390–399, Cham, December 2021. Springer International Publishing. ISBN 978-3-030-91877-4. doi: 10.1007/978-3-030-91877-4_45.

[25] Jorg Schlaich and Kurt Schafer. Design and detailing of structural concrete using strut-and-tie models. *Structural Engineer*, 69(6):113–125, 1991. URL http://www.pgmec.ime.eb.br/~webde2/prof/ethomaz/bloco_sobre_estacas/biela_tirante.pdf.

[26] W. Don, B. Suryanto, A. Tambusay, and P. Suprobo. Forensic assessments of the influence of reinforcement detailing in reinforced concrete half-joints: A nonlinear finite element study. *Structures*, 38:689–703, April 2022. ISSN 23520124. doi: 10.1016/j.istruc.2022.02.029. URL https://linkinghub.elsevier.com/retrieve/pii/S2352012422001205.

[27] M di Prisco, M Colombo, P Martinelli, and D Coronelli. The technical causes of the collapse of Annone overpass on SS.36. *Il Calcestruzzo Strutturale Oggi: Teoria Impieghi Materiali Tecniche*, 150:1–16, 2018. ISSN 9788899916114. URL https://re.public.polimi.it/retrieve/e0c31c0c-4127-4599-e053-1705fe0aef77/150_MDPLEC_ITA_FIN.pdf.

[28] Pieter Desnerck, Janet M Lees, and Chris Morley. Assessment of reinforced concrete half-joint structures: dealing with deterioration. *Proceedings of the 2014 PCI Convention and National Bridge Conference*, page 16, 2014.

[29] Wagemaker. Constructieve analyse tandopleggingen Nelson Mandelabrug. Technical report, November 2022.

[30] Hans Böhni. *Corrosion in reinforced concrete structures*. 2005.

[31] Y G Du, L A Clark, and A H C Chan. Residual capacity of corroded reinforcing bars. *Magazine of Concrete Research*, (3), 2005.

[32] H. Cai and X. Liu. Freeze-thaw durability of concrete: ice formation process in pores. *Cement and Concrete Research*, 28(9):1281–1287, September 1998. ISSN 00088846. doi: 10.1016/S0008-8846(98)00103-3. URL https://linkinghub.elsevier.com/retrieve/pii/S0008884698001033.

[33] Dan F. Adkins and Vance T. Christiansen. Freeze-Thaw Deterioration of Concrete Pavements. *Journal of Materials in Civil Engineering*, 1(2):97–104, May 1989. ISSN 0899-1561, 1943-5533. doi: 10.1061/(ASCE)0899-1561(1989)1:2(97). URL https://ascelibrary.org/doi/10.1061/%28ASCE%290899-1561%281989%291%3A2%2897%29.

[34] Ruijun Wang, Qingjun Zhang, and Yang Li. Deterioration of concrete under the coupling effects of freeze–thaw cycles and other actions: A review. *Construction and Building Materials*, 319: 126045, February 2022. ISSN 09500618. doi: 10.1016/j.conbuildmat.2021.126045. URL https://linkinghub.elsevier.com/retrieve/pii/S0950061821037776.

[35] William H. Paulsen. Eigenfrequencies of the three dimensional euler-bernoulli beam system with dissipative joints. *Applied Mathematics and Mechanics*, 16(8):723–746, August 1995. ISSN 0253-4827, 1573-2754. doi: 10.1007/BF02453398. URL http://link.springer.com/10.1007/BF02453398.

[36] Bernard Enright. Simulation of Traffic Loading on Highway Bridges, PhD Thesis, 2010.

[37] Hannes Ludescher and Eugen Brühwiler. Dynamic Amplification of Traffic Loads on Road Bridges. *Structural Engineering International*, 19(2):190–197, May 2009. ISSN 1016-8664, 1683-0350. doi: 10.2749/101686609788220231. URL https://www.tandfonline.com/doi/full/10.2749/101686609788220231.

[38] NEN. Eurocode 1: Belastingen op constructies – Deel 2: Verkeersbelasting op bruggen, 2015.

[39] Jan Kalin, Aleš Žnidarič, Andrej Anžlin, and Maja Kreslin. Measurements of bridge dynamic amplification factor using bridge weigh-in-motion data. *Structure and Infrastructure Engineering*, 18(8): 1164–1176, August 2022. ISSN 1573-2479, 1744-8980. doi: 10.1080/15732479.2021.1887291. URL https://www.tandfonline.com/doi/full/10.1080/15732479.2021.1887291.

[40] Sushmita Borah, Amin Al-Habaibeh, and Rolands Kromanis. The Effect of Temperature Variation on Bridges—A Literature Review. In Iosif Mporas, Pandelis Kourtessis, Amin Al-Habaibeh, Abhishek Asthana, Vladimir Vukovic, and John Senior, editors, *Energy and Sustainable Futures*, pages 207–212. Springer International Publishing, Cham, 2021. ISBN 978-3-030-63915-0 978-3-030-63916-7. doi: 10.1007/978-3-030-63916-7_26. URL https://link.springer.com/10.1007/978-3-030-63916-7_26. Series Title: Springer Proceedings in Energy.

[41] Emanuel Sousa Tomé, Mário Pimentel, and Joaquim Figueiras. Structural response of a concrete cable-stayed bridge under thermal loads. *Engineering Structures*, 176:652–672, December 2018. ISSN 0141-0296. doi: 10.1016/j.engstruct.2018.09.029. URL https://www.sciencedirect.com/science/article/pii/S0141029618311763.

[42] Rolands Kromanis and Prakash Kripakaran. Predicting thermal response of bridges using regression models derived from measurement histories. *Computers & Structures*, 136:64–77, May 2014. ISSN 0045-7949. doi: 10.1016/j.compstruc.2014.01.026. URL https://www.sciencedirect.com/science/article/pii/S0045794914000376.

[43] Qi Xia, Liming Zhou, and Jian Zhang. Thermal performance analysis of a long-span suspension bridge with long-term monitoring data. *Journal of Civil Structural Health Monitoring*, 8(4):543–553, September 2018. ISSN 2190-5479. doi: 10.1007/s13349-018-0299-y. URL https://doi.org/10.1007/s13349-018-0299-y.

[44] Shuzhen Yang, Baodong Liu, and Fang Li. Estimations of the elastic moduli of concrete at different temperatures and humidities by mesomechanics methods. *Case Studies in Construction Materials*, 17:e01254, December 2022. ISSN 2214-5095. doi: 10.1016/j.cscm.2022.e01254. URL https://www.sciencedirect.com/science/article/pii/S2214509522003862.

[45] Paola Darò, Isabella Alovisi, Giuseppe Mancini, Serena Negri, Agnieszka Bigaj-van Vliet, and Hendrik Meerveld. Lessons Learned from Proactive Maintenance Practices for Concrete Bridges. June 2022. ISBN 978-2-940643-15-8.

[46] Alejandro Moreno-Gomez, Carlos A. Perez-Ramirez, Aurelio Dominguez-Gonzalez, Martin Valtierra-Rodriguez, Omar Chavez-Alegria, and Juan P. Amezquita-Sanchez. Sensors Used in Structural Health Monitoring. *Archives of Computational Methods in Engineering*, 25(4):901–918, November 2018. ISSN 1134-3060, 1886-1784. doi: 10.1007/s11831-017-9217-4. URL http://link.springer.com/10.1007/s11831-017-9217-4.

[47] Paola Darò. Background Materials for implementation of decision-making regarding maintenance strategies. 2020.

[48] Robert James Barthorpe. Model- and Data-based Approaches to Structural Health Monitoring, January 2011. URL https://etheses.whiterose.ac.uk/1175/2/Barthorpe,_R.pdf.

[49] Keith Worden and Graeme Manson. The application of machine learning to structural health monitoring. *Philosophical Transactions of the Royal Society A: Mathematical, Physical and Engineering Sciences*, 365(1851):515–537, February 2007. ISSN 1364-503X, 1471-2962. doi: 10.1098/rsta.2006.1938. URL https://royalsocietypublishing.org/doi/10.1098/rsta.2006.1938.

[50] Y Gunawardena, F Aslani, and Jun Li. Exploratory investigation of monitoring data obtained from an in-service pre- stressed concrete bridge incorporating a distinct half-joint layout. Brisbane, December 2017.

[51] Michael V. Gangone, Matthew J. Whelan, and Kerop D. Janoyan. Wireless Monitoring of a Multispan Bridge Superstructure for Diagnostic Load Testing and System Identification: Wireless monitoring of a multispan bridge. *Computer-Aided Civil and Infrastructure Engineering*, 26 (7):560–579, October 2011. ISSN 10939687. doi: 10.1111/j.1467-8667.2010.00711.x. URL https://onlinelibrary.wiley.com/doi/10.1111/j.1467-8667.2010.00711.x.

[52] A.J. Cardini and J.T. DeWolf. Long-term Structural Health Monitoring of a Multi-girder Steel Composite Bridge Using Strain Data. *Structural Health Monitoring*, 8(1):47–58, January 2009. ISSN 1475-9217, 1741-3168. doi: 10.1177/1475921708094789. URL http://journals.sagepub.com/doi/10.1177/1475921708094789.

[53] Maria Pina Limongelli, Carmelo Gentile, Fabio Biondini, Marco Di Prisco, Francesco Ballio, Giacomo Zonno, Paolo Borlenghi, Silvia Bianchi, Luca Capacci, Mattia Anghileri, Giulio Zani, Agnese Scalbi, Katherina Flores Ferreira, Manuel D'Angelo, Gabriele Cazzulani, Lorenzo Benedetti, Claudio Somaschini, Lorenzo Bernardini, Marco Belloli, Ferruccio Resta, Paola Vigo, and Aldo Colombo. Bridge structural monitoring: the Lombardia regional guidelines. *Structure and Infrastructure Engineering*, 20(4):461–484, April 2024. ISSN 1573-2479, 1744-8980. doi: 10.1080/15732479.2022.2107023. URL https://www.tandfonline.com/doi/full/10.1080/15732479.2022.2107023.

[54] A Arun Solomon and G Hemalatha. Characteristics of expanded polystyrene (EPS) and its impact on mechanical and thermal performance of insulated concrete form (ICF) system. *Structures*, 23:204–213, February 2020. ISSN 23520124. doi: 10.1016/j.istruc.2019.10.019. URL https://linkinghub.elsevier.com/retrieve/pii/S2352012419301900.

[55] Wensu Chen, Hong Hao, Dylan Hughes, Yanchao Shi, Jian Cui, and Zhong-Xian Li. Static and dynamic mechanical properties of expanded polystyrene. *Materials & Design*, 69:170–180, March 2015. ISSN 02613069. doi: 10.1016/j.matdes.2014.12.024. URL https://linkinghub.elsevier.com/retrieve/pii/S0261306914010085.

[56] Ninghan Tang, Dong Lei, Dianwu Huang, and Rui Xiao. Mechanical performance of polystyrene foam (EPS): Experimental and numerical analysis. *Polymer Testing*, 73:359–365, February 2019. ISSN 01429418. doi: 10.1016/j.polymertesting.2018.12.001. URL https://linkinghub.elsevier.com/retrieve/pii/S0142941818315046.

[57] CT deBoer. Opleverdossier montage - monitoring zuidelijke brug over de Naardertrekvaart. Technical Report 6818-OD-001, January 2022.

[58] Ingenieursbureau Kok & Van den Heuvel. Rapportage Naardertrekvaart. Technical Report 2054-NOT-01, January 2021.

[59] NEN. Eurocode 2: Ontwerp en berekening van betonconstructies - Deel 1-1: Algemene regels en regels voor gebouwen, 2011.

[60] M. E. Mohamad, I. S. Ibrahim, R. Abdullah, A. B. Abd. Rahman, A. B. H. Kueh, and J. Usman. Friction and cohesion coefficients of composite concrete-to-concrete bond. *Cement and Concrete Composites*, 56:1–14, February 2015. ISSN 0958-9465. doi: 10.1016/j.cemconcomp.2014.10.003. URL https://www.sciencedirect.com/science/article/pii/S0958946514001954.

[61] NEN. Nationale bijlage bij NEN-EN 1992-1-1+C2 Eurocode 2: Ontwerp en berekening van betonconstructies - Deel 1- 1: Algemene regels en regels voor gebouwen, 2020.

[62] PVENO. 4.2.3 Gewapende rubber opleggingen. URL https://www.pveno.nl/handboek-opleggingen/handboek/4-vervormingen-en-bewegingen/4-2-rubber-opleggingen/4-2-3-gewapende-rubber-opleggingen/.

[63] IV-Infra. Nader onderzoek 25H-300-01+02 - Fase 2b - Herberekening HIP-ligger met tand. Technical report, January 2016.

[64] IV-Infra. Nader onderzoek 25H-300-01+02 - Fase 2d - Herberekening Preflex-ligger met tand. Technical report, September 2017.

A

Relevant Design Drawings of the Naardertrekvaart Bridge

This appendix contains the design drawings of the Naardertrekvaart bridge that have been consulted for this research. Table A.1 gives a description of these drawings.

Table A.1: Description and page of the design drawings consulted for this research

Description	Page
Overview of the northern and southern bridge	61
Dimensions of support 6 of the southern bridge	62
Dimensions of the plates welded to the flanges of the IPE profile of the Preflex girders	63
Dimensions of the plates welded to the webs of the IPE profile of the Preflex girders	64

BOVENAANZICHT.

PEILMATEN. WEGDEK = BOVENKANT AFWERKLAAG.

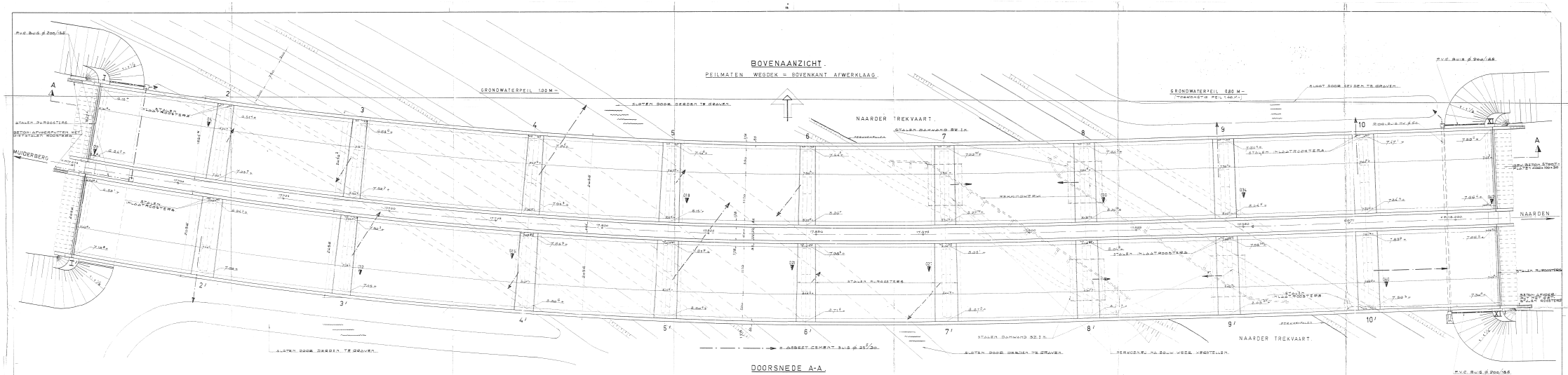

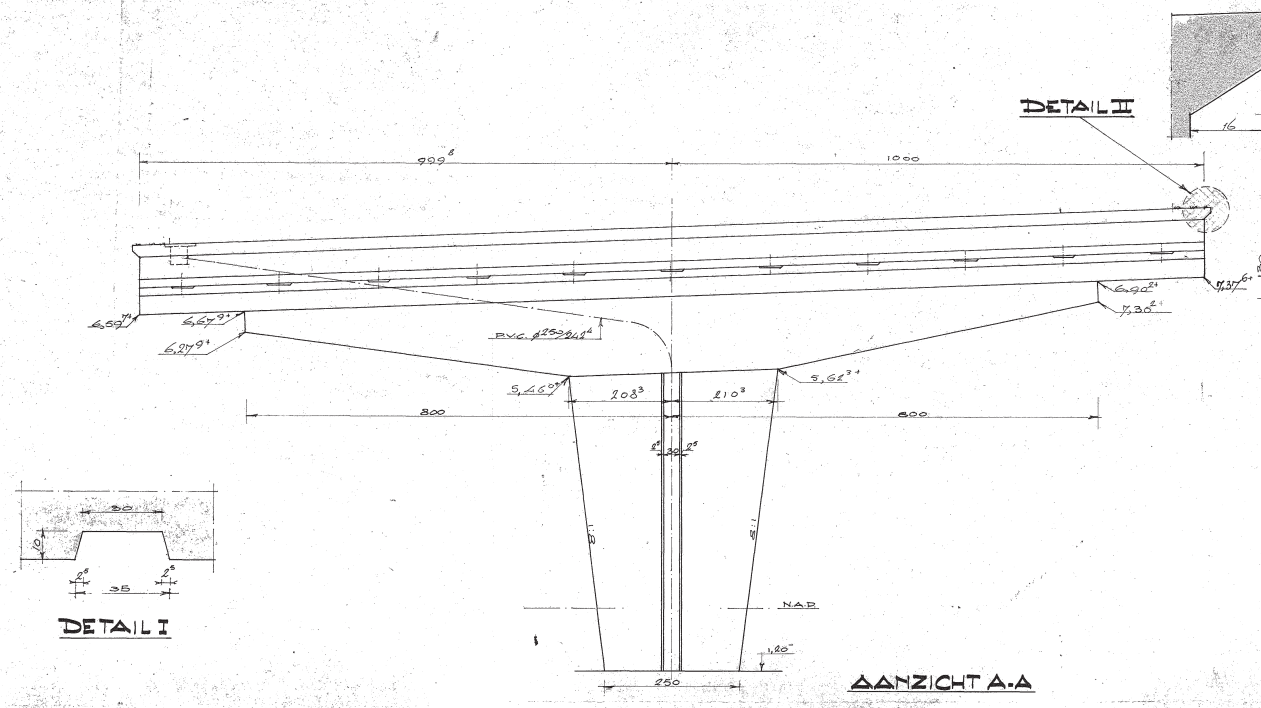

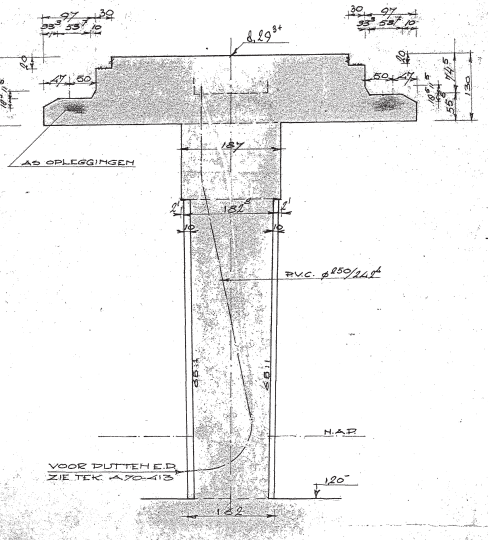

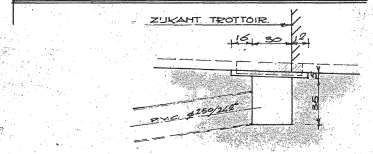

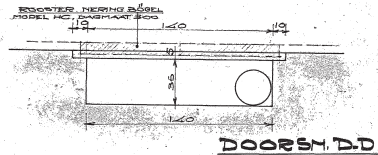

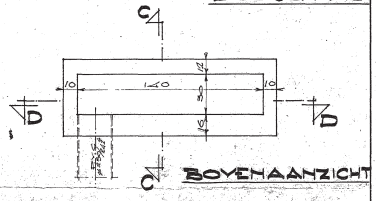

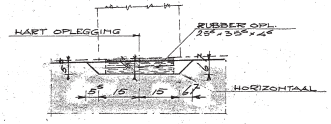

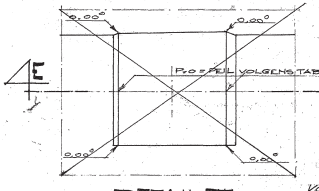

VOORGEWIJZIGDE DETAILS III EN IV ZIE TEK. A70-424

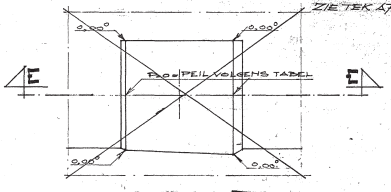

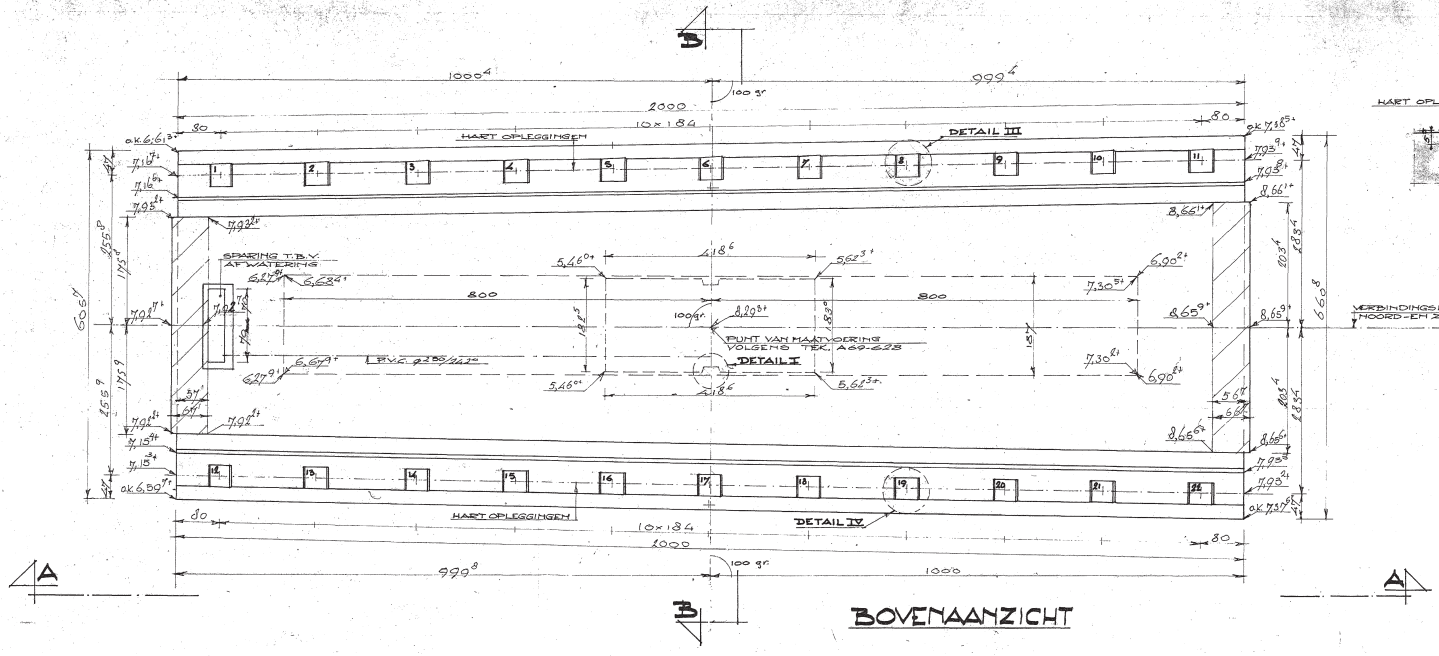

PEILMATEN VAN INKASSINGEN																					
1	2	3	4	5	6	7	8	9	10	11	12	13	14	15	16	17	18	19	20	21	22
7,13	7,10	7,07	7,05	7,02	7,00	6,98	6,95	6,93	6,91	6,89	6,87	6,85	6,84	6,83	6,82	6,81	6,80	6,79	6,78	6,77	6,76

OPM:

MATEN IN CM ; PEILMATEN IN M T.O.V. N.A.P.
VELLINGHOEKEN 2:2 CM.
MATENTEK. FUNDERINGS PLATEN ; ZIE TEK. A69-698.
VOOR PVC BUIS ø250/12,5 T.B.V. AFWATERING, ZIE TEK A70-394
VOOR IN TE STORTEN BEVESTIGINGEN ALUMINIUM BEKLEDING ZIE TEK. A70-412.

A WIJZIGING INKASSINGEN T.P.V. RUBBEROPL.

RIJKSWATERSTAAT DIRECTIE SLUIZEN EN STUWEN

R.W. 1

OPGEMAAKT TE UTRECHT:
DE HFD. ING. V.B.D.:
DE HFD. INGENIEUR:
DE T.H.A. V.B.D.:

GET.: -4-'70
GEZ.: 16-5-'70

GEWIJZIGD

K.W.A.

MATENTEK. PIJLER 6z

SCHAAL: 1:50 1:20 1:10 1:5

FORMAAT: A1

TEK. A70-425

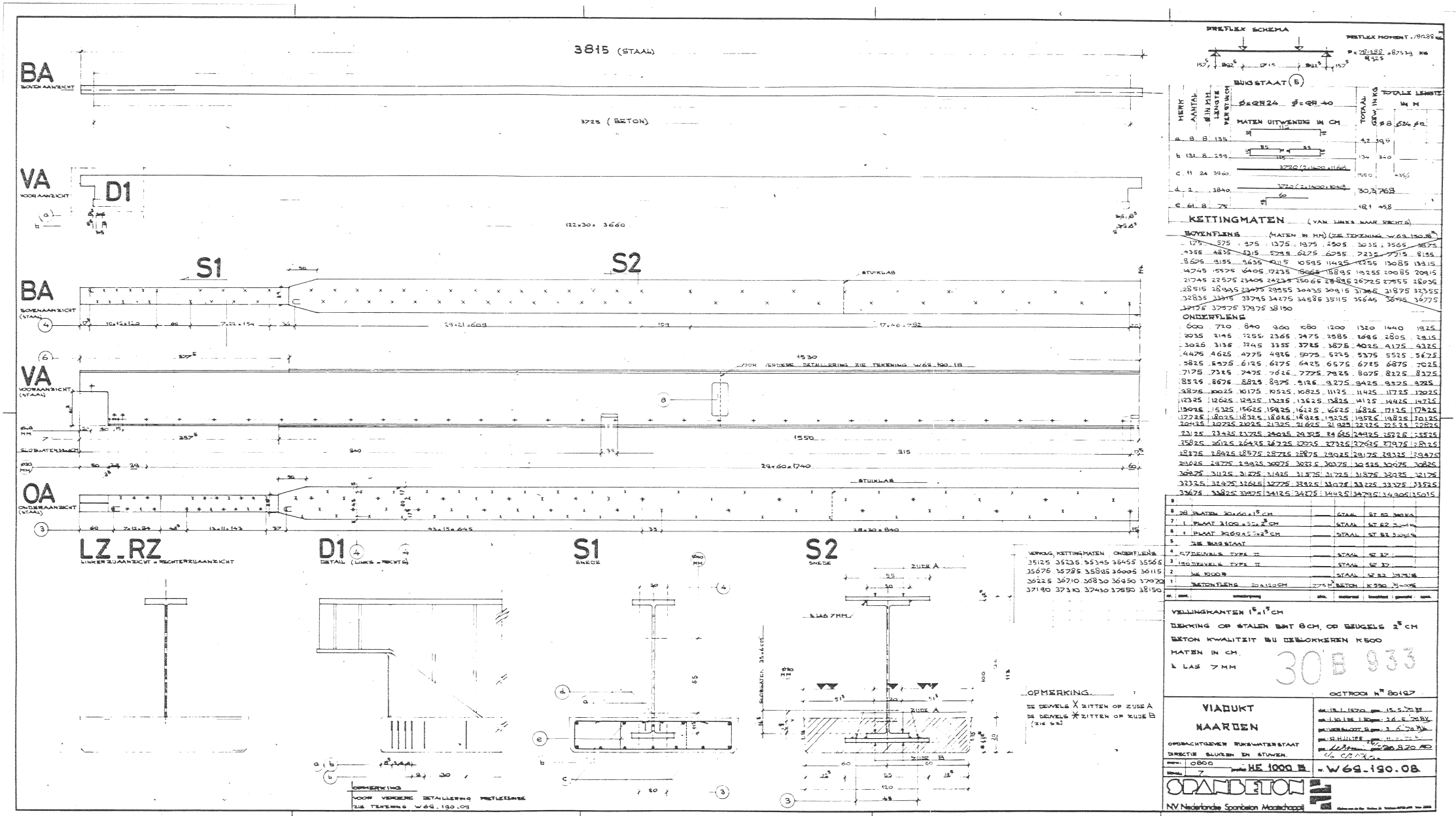

PREFLEX SCHEMA

PREFLEX MOMENT : 1849.98 tm

P = 2x1380 = 2760 KN = 276 ton

BUIGSTAAT (5)

MERK	AANTAL	Ø IN MM LENGTE PER STUK CM	MATEN UITWENDIG IN CM	TOTAAL GEW. IN KG	TOTALE LENGTE IN M
			Ø=Ø24 Ø=Ø40	TOTAAL GEW. 8856 KG	
a	8	8 135	115	42 39,9	
b	131	8 259	85 85 115	134 340	
c	11	24 3960	3720 (2x1800+120+120)	1550 4356	
d	2	3840	3720 (2x1800+120+120)	30,3768	
e	61	8 75	60	18,1 458	

KETTINGMATEN (VAN LINKS NAAR RECHTS)

BOVENFLENS (MATEN IN MM) (ZIE TEKENING W69.190.18)

1275	525	1375	1375	1975	2505	3035	3565	3875
4385	4835	5315	5795	6275	6755	7235	7715	8195
8675	9155	9635	10115	10595	11435	12155	13085	13915
14745	15575	16405	17235	18065	18895	19255	20085	20915
21745	22575	23405	24235	25066	25896	26725	27555	28235
28915	29595	29975	30435	30915	31395	31875	32355	
32835	33315	33795	34275	34585	35115	35645	36175	
36706	37575	37975	38150					

ONDERFLENS

600	720	840	960	1080	1200	1320	1440	1925
2035	2145	2255	2365	2475	2585	1695	2805	2915
3026	3136	3245	3355	3785	3875	4025	4125	4325
4425	4625	4775	4925	5075	5225	5375	5525	5675
5825	5975	6125	6275	6425	6575	6725	6875	7025
7175	7325	7475	7625	7775	7925	8075	8225	8375
8525	8675	8825	8975	9126	9275	9425	9575	9725
9876	10025	10175	10525	10825	11125	11425	11725	12025
12325	12625	12925	13225	13525	13825	14125	14425	14725
15026	15325	15625	15925	16225	16525	16825	17125	17425
17725	18025	18325	18625	18925	19225	19525	19825	20125
20425	20725	21025	21325	21625	21925	22225	22525	22825
23125	23425	23725	24025	24325	24625	24925	25225	25525
25825	26125	26425	26725	27025	27325	27625	27975	28125
28425	28725	29025	29325	29625	29925	30225	30525	30825
31125	31425	31725	32025	32325	32625	32925	33225	33525
33825	34125	34425	34725	35025	35325	35625	35925

S2
SNEDE

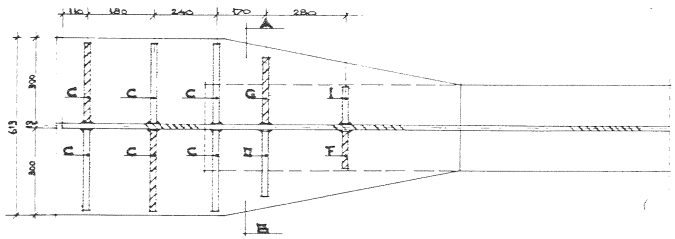

MERK A

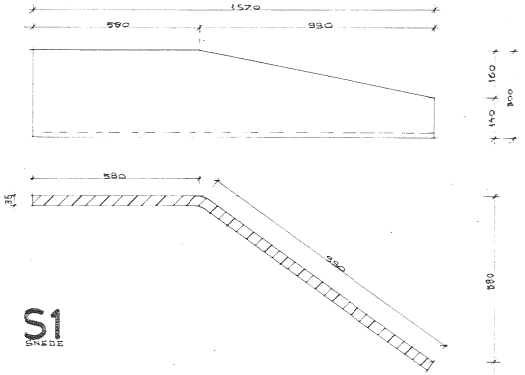

MERK B

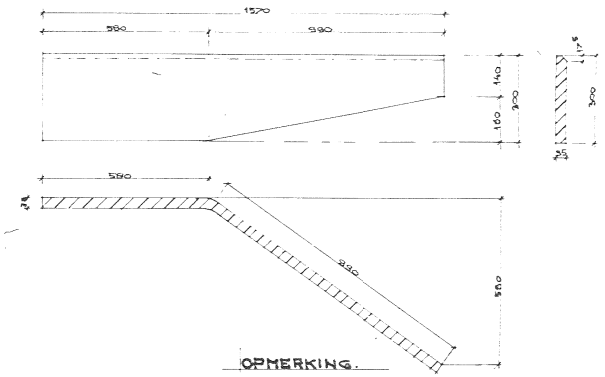

VA
VOORAANZICHT (LINKS GELUK RECHTS)

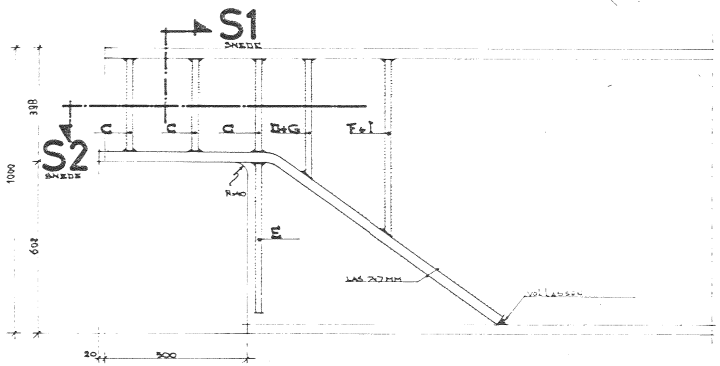

S1
SNEDE

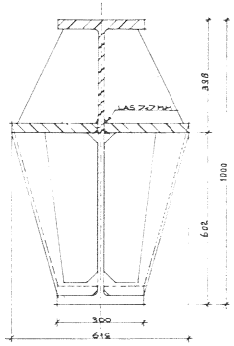

OPMERKING.

MATEN IN MM

LASSEN 5x5 MM TENZY ALLERZIJDS AANGEBRACHT

31

EB 933

MERK C

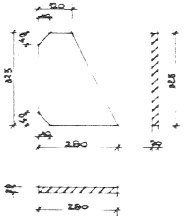

MERK D

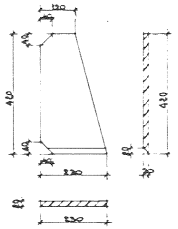

MERK E

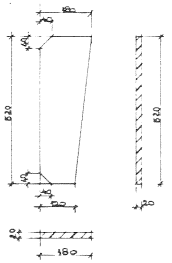

MERK F

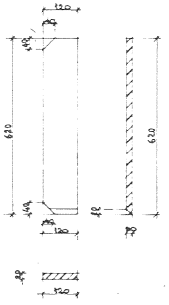

MERK G

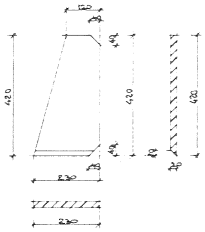

MERK I

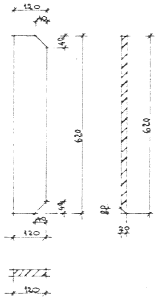

GELDT VOOR PRETLEK BALKEN MERK 0300 T/M 0322

aantal	profiel	merk	lengte / cm	gew. / kg	beschrijving	tek.
264	—	C	DIK 2 CM	—	VERSTIJVINGSPLATEN (ST 52)	
44	—	D	DIK 2 CM	—	" "	
88	—	E	DIK 2 CM	—	" "	
44	—	F	DIK 2 CM	—	" "	
44	—	G	DIK 2 CM	—	" "	
44	—	I	DIK 2 CM	—	" "	
44	—	A	DIK 3⅝ CM	—	FLENSPLATEN (ST 52)	
44	—	B	DIK 3⅝ CM	—	" "	

Door Spanbeton te leveren

VIADUKT
NAARDEN

OPDRACHTGEVER RIJKSWATERSTAAT
DIRECTIE SLUIZEN EN STUWEN

gem. A 6-1970	gew.
gem. 1:25	gew.
gem. VERSLOOT 8	gew.
gem. E	gew.
gem.	gew.

DETAILTEKENING — W 69-130-09

SPANBETON

N.V. Nederlandse Spanbeton Maatschappij

B

Overview of Previously Conducted Inspections and Reparations

Table B.1 gives an overview of previously conducted inspections and reparations to the Naardertrekvaart bridge.

Table B.1: Overview of the previously conducted inspections and reparations to the Naardertrekvaart bridge

Year	Description
1969	Completion of construction.
1988	First observation of damage resulting from leakage of the expansion joints.
1994	Metal grids above the half-joint gaps replaced by bituminous expansion joints. Vertical surfaces of the concrete inside the half-joint gaps instrumented with a Latexfalt layer, with the goal of conservation.
1998	Additional damage as a result of leakage of the expansion joints was observed.
?	Addition of concrete to the support platform, with the goal of increasing the concrete cover. Concrete instrumented with a protective coating at multiple locations.
2007	Concrete compression layer covered with a strengthening layer of HSC.
2014/2015	Leakage of the expansion joints was observed in the northern bridge, but there were no signs of leakage of the southern bridge.
2015	Replacement of all bituminous expansion joints.
2016	Inspection indicated no leakage of the expansion joints, but did indicate inadequate precipitation drainage capability.
2017/2018	Inspection indicated new complications inside of the half-joints.
2019	Measurements of reinforcement bar potential indicated a high variance of possibility of corrosion along the bridge, with several bars exhibiting a high chance of corrosion.
2020/2021	Removal and replacement of a large area of loosened concrete of the lower half-joint nibs of multiple supports.
2022	Installation and activation of the structural health monitoring system.

C

Supplementary Information about the Data Analysis

C.1. Data Preparation

This section contains the steps taken to prepare the different types of measurement data for analysis.

C.1.1. Preparation of the Historical Data of the Naardertrekvaart Bridge Monitoring System

The preparation of the historical data of the monitoring system on the Naardertrekvaart bridge consisted of the following steps.

1. Converting the optical reflection measurements to measurements of the physical parameters using predefined formulas and constants.
2. Removing measurements before the last correction to the sensor setup.
3. Downcasting the dataset to save memory.
4. Dropping the measurement data from sensor T107, measuring the outside temperature, as it takes unrealistic measurements.
5. Adding temperature measurements by the KNMI (Dutch Meteorological Institute) at the meteorological station in De Bilt.

C.1.2. Preparation of the High-Frequency Data of the Naardertrekvaart Bridge Monitoring System

The preparation of the high-frequency data of the monitoring system of the Naardertrekvaart bridge consisted of the following steps.

1. Converting the optical reflection measurements to measurements of the physical parameters using predefined formulas and constants.
2. Applying an offset to shift the measurement data of the inclinometers and displacement sensors. The offset value is taken as the mean measured value between 3:00 and 4:00 on 26-07-2024.
3. Downcasting the dataset to save memory.
4. Dropping the measurement data from sensor T107, measuring the outside temperature, as it takes unrealistic measurements.

C.1.3. Preparation of the Measurement Data of the Bridge WIM System on the Moerdijkbrug

The preparation of the measurement data of the Bridge WIM system on the Moerdijkbrug consisted of the following steps.

1. Removing observed vehicles of which no license plate could be registered.
2. Removing observed vehicles with a gross vehicle weight of $0\mathrm{kN}$.
3. Removing observed vehicles with an axle weight below $6\mathrm{kN}$.
4. Removing observed vehicles with an axle-to-axle distance greater than $7\mathrm{m}$.

The significant effect of this filtering method is visible in a scatter plot of the outer axle distance of the vehicles and their gross vehicle weight, which is shown in Figure C.1.

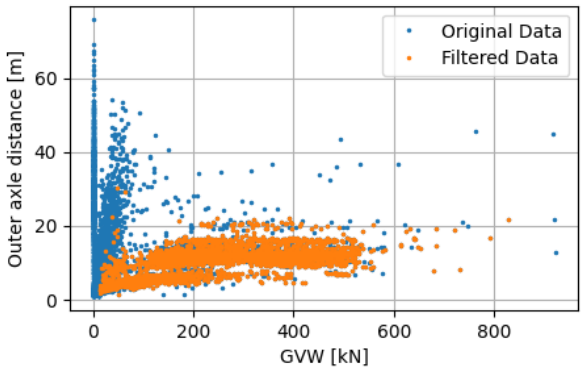

Figure C.1: Scatter plot of the vehicle outer axle distance and the gross vehicle weight, for the original and filtered data.

C.2. Histograms of Historical and High-Frequency Measurement Data

Figure C.2 contains histograms of the historical and high-frequency measurement data of every inclinometer, highlighting the behavioural differences between the datasets.

C.3. Power Spectral Density Plots

Figure C.3 contains PSD plots of all inclinometers.

C.4. Correlation Matrices

This section contains the full correlation matrices used for the analysis of bridge behaviour. Figure C.4 shows the correlation matrix of the sensors' full dataset, while Figure C.5 shows the correlation matrix of the $10\mathrm{Hz}$ data of the sensors.

C.5. Estimated Load versus Normalised Amplitude Plots

Figure C.6 contains the plots of the relationship between the estimated vertical load on the lower half-joint nib and the amplitude of the rotation measurements.

Figure C.2: Histograms of the historical and high-frequency measurement data of every inclinometer

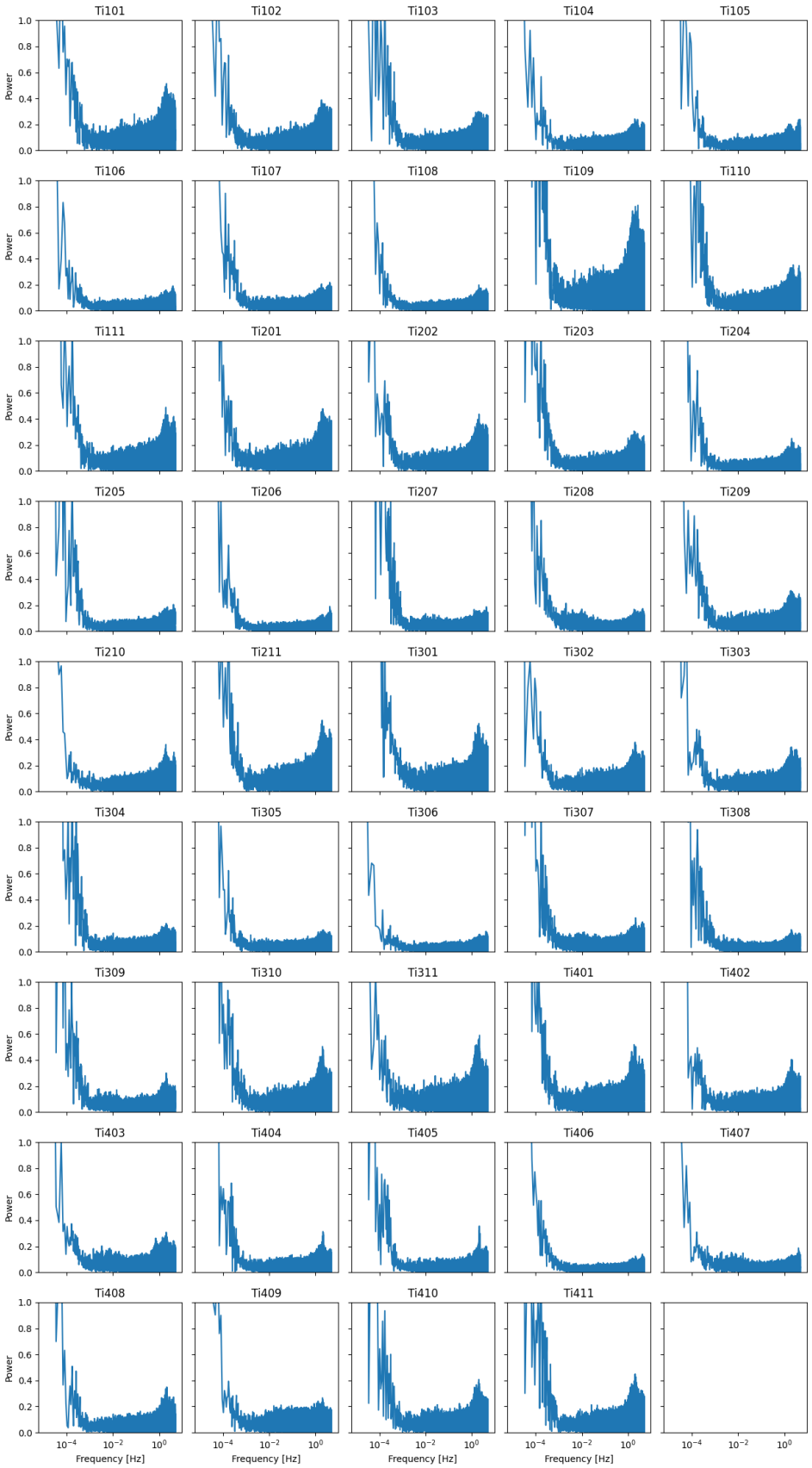

Figure C.3: Power spectral density plots of all inclinometers

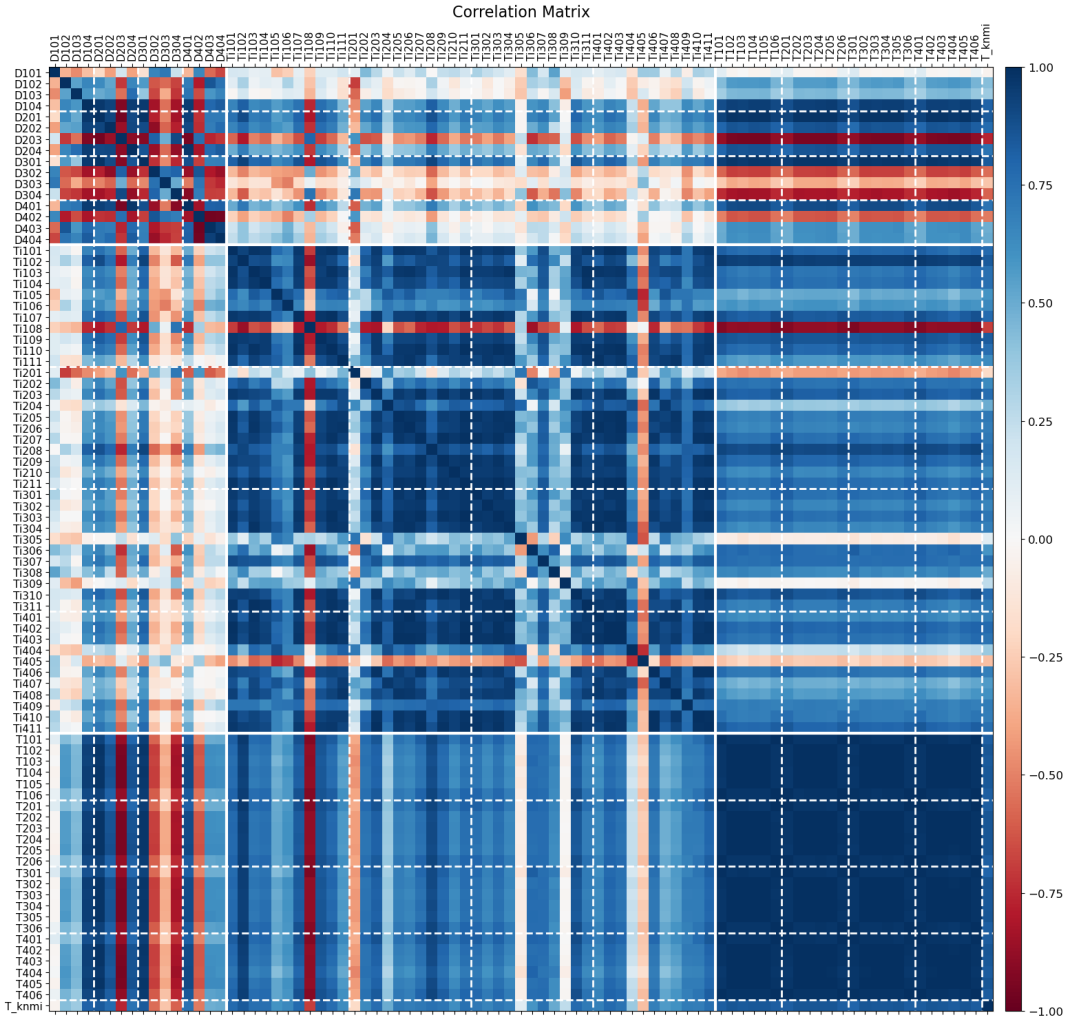

Figure C.4: Correlation matrix, a visualisation of the degree of correlation between the sensors

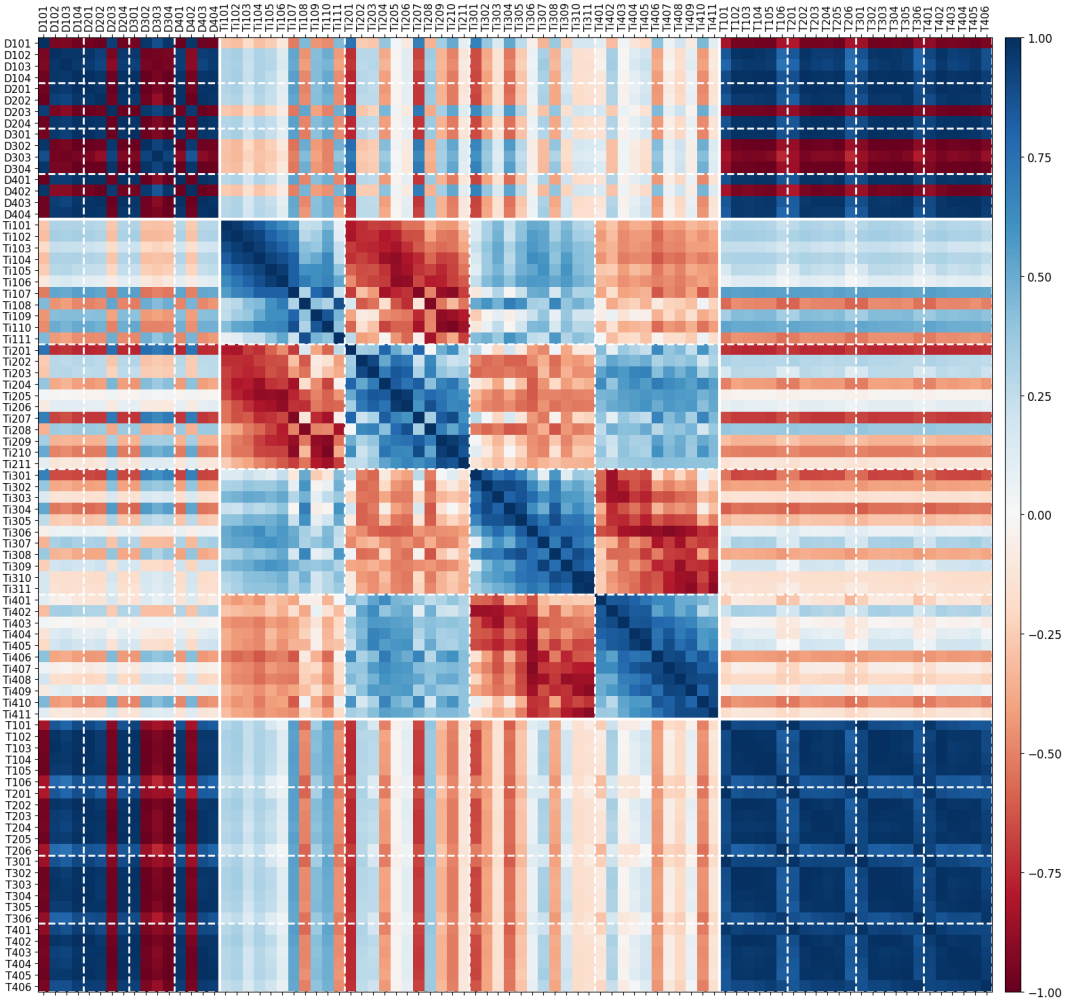

Figure C.5: Correlation matrix of the sensors' deviation from a rolling average

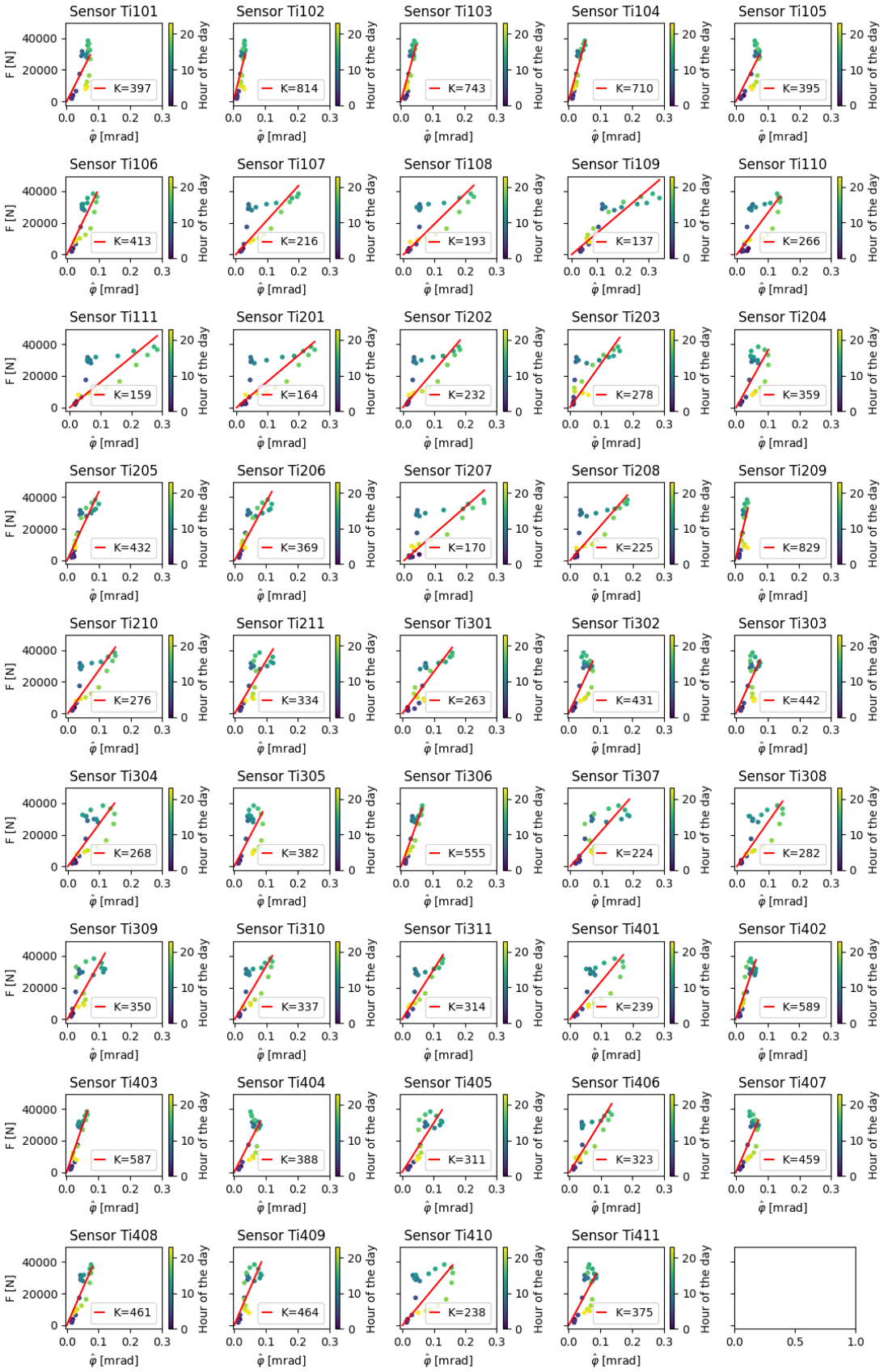

Figure C.6: Plots of the relationship between the estimated vertical load on the lower half-joint nib and the amplitude of the rotation measurements

D

Numerical Models

Three numerical models are used to investigate the effect of local stiffness variation on the behaviour of the Naardertrekvaart bridge. This chapter describes the numerical models used for this investigation. Considering the relative nature of the measurements performed by the sensors, all computational models exclude the influence of the self-weight of the structural elements, as its impact on the observed deformation is deemed negligible.

D.1. 2D Plane Stress Model of Half a Standard Span

A 2D plane stress model of half a standard span of the Naardertrekvaart bridge is developed to investigate the local effect of thermal expansion. The magnitude of this effect depends on the stiffness of the material in the half-joint gap. The model is shown in Figure D.1. The geometrical components of the model are discussed in Section D.1.1, its supports in Section D.1.2, and its mesh in Section D.1.3. The ability of the model to simulate the behaviour of the physical structure, and thereby the validity of the assumptions taken in the model, is confirmed in Appendix E.1.

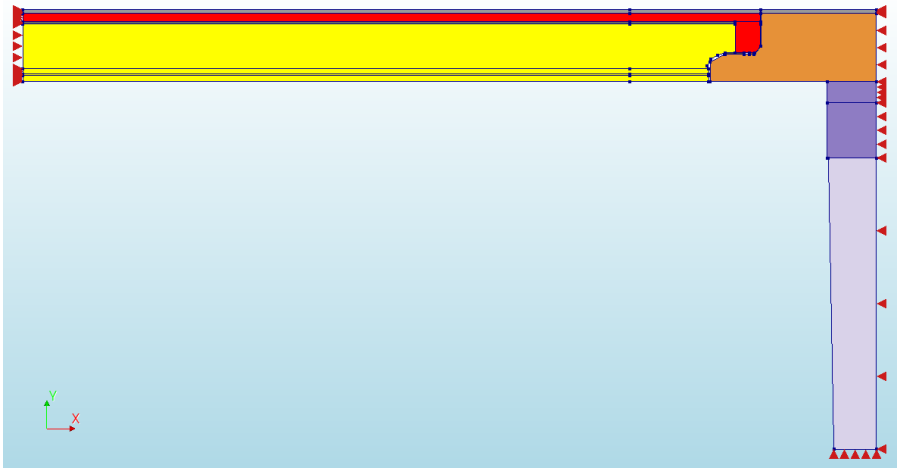

Figure D.1: 2D model of half a standard span of the Naardertrekvaart bridge

D.1.1. Geometrical Components

The numerical model consists only of plane stress elements that represent the entire width of the bridge. Consequently, the thickness of the longitudinal girder components is adapted to account for all eleven girders along the width of the bridge. This modelling decision presumes that the girders act together as a unified member. Additionally, modelling of the bridge with 2D plane stress elements neglects the additional stiffness that is generated through restrained transverse expansion resulting from the Poisson effect.

The thickness of several elements of the support column and the HIP girder varies with their height. In the numerical model, these elements are modelled by their average thickness.

The bearing plate is modelled with a plane stress element, rigidly connected to the lower half-joint nib and connected to the span using an interface element. The plane stress element keeps the distance between the girder and the lower half-joint nib present in the physical structure, while the interface element simulates the elastic behaviour of the bearing plates under vertical and horizontal loading. The elastic stiffness used for the interface element is calculated using approximation formula's developed by a dutch collaboration of civil engineering companies [62]. The prescribed equations can be rewritten in a horizontal and vertical stiffness equation, K_h and K_v respectively, as can be found in Equation D.1 and D.2. The resulting values for the horizontal and vertical stiffnesses can be found in Table D.2

$$K_h = \frac{A' \cdot G}{\sum_i t_i} \tag{D.1}$$

$$K_v = \sum_i \frac{t_i}{A'} \left(\frac{1}{5GS^2} + \frac{1}{2000} \right) \tag{D.2}$$

t_i : thickness of rubber layer i [mm],
G : shear modulus of rubber, taken as $1\mathrm{N}/\mathrm{mm}^2$ according to PVENO [62]
S : correction factor, calculated with $\frac{A'}{2(a'+b') \cdot t_i}$ [-],
a', b' : width and height of the steel plates [mm^2].

The dimensions of the geometrical components of the model can be found in Figure D.2. The properties of the geometrical components of the model can be found in Table D.1.

D.1.2. Supports

The supports of the model restrict displacement of the model at the base of the columns in y-direction (vertical), and at the location of the symmetry lines in x-direction (horizontal). The location and direction of the supports are visible in Figure D.1.

D.1.3. Mesh

The mesh of the model uses small elements near possible stress concentration locations and larger elements at locations where the model is expected to behave undisturbed. The mesh of the spanning elements is achieved with a mesh seeding method based on element size, with a desired element size of $1\mathrm{m}$ and a size transition smoothness of 0.06. The mesh of the platform and transition elements is achieved with the same seeding method, but with a desired element size of $200\mathrm{mm}$ and a size transition smoothness of 0.5. No desired element size was specified for the column of the support column. The resulting mesh can be found in Figure D.3.

D.2. 2D Plane Stress Model of the Full Bridge

To investigate the effect of thermal expansion of the entire bridge, a 2D plane stress model of the full bridge is developed. The model is shown in Figure D.4.

D.2.1. Geometrical Components

Similar to the 2D plane stress model of half a span of the bridge, the elements in this model represent the full width of the bridge, and the thickness of the elements is adapted to account for this. As a result, the longitudinal girder elements have a thickness that is 11 times higher than their actual thickness, which assumes full composite action between the longitudinal girders. Furthermore, the additional stiffness resulting from restrained transverse expansion is neglected by the use of plane stress elements.

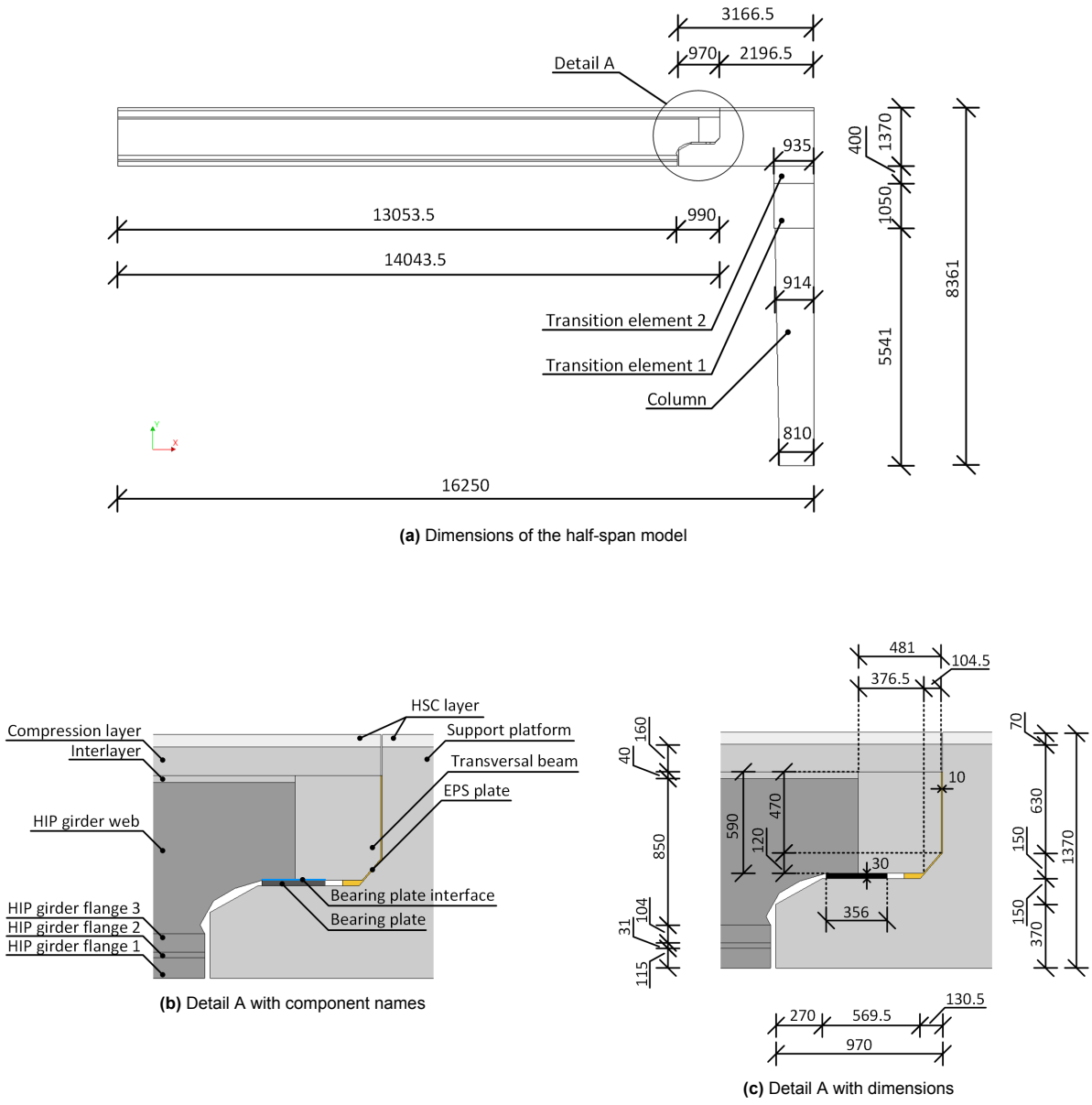

(a) Dimensions of the half-span model

(b) Detail A with component names

(c) Detail A with dimensions

Figure D.2: Dimensions of the geometrical components of the 2D model of half a standard span

Table D.1: Element properties of the 2D model of half a span. E-modulus values have been extracted from [63].

Member	Type	E $[\mathrm{N/mm^2}]$	G $[\mathrm{N/mm^2}]$	ν [-]	α $[\mathrm{K^{-1}}]$	t $[\mathrm{mm}]$
Support						
Column	Plane stress	25788	-	0.15	1e-5	3343
Transition element 1	Plane stress	25788	-	0.15	1e-5	10093
Transition element 2	Plane stress	25788	-	0.15	1e-5	16000
Support platform	Plane stress	25788	-	0.15	1e-5	20000
HSC layer	Plane stress	37452	-	0.15	1e-5	20000
Span						
HIP girder flange part 1	Plane stress	32971	-	0.15	1e-5	12980 (11x1180)
HIP girder flange part 2	Plane stress	32971	-	0.15	1e-5	9592 (11x872)
HIP girder flange part 3	Plane stress	32971	-	0.15	1e-5	4752 (11x432)
HIP girder web	Plane stress	32971	-	0.15	1e-5	3300 (11x300)
Interlayer	Plane stress	25788	-	0.15	1e-5	3300 (11x300)
Compression layer	Plane stress	25788	-	0.15	1e-5	20000
HSC layer	Plane stress	37452	-	0.15	1e-5	20000
Transversal beam	Plane stress	25788	-	0.15	1e-5	20000
EPS plate	Plane stress	5.5	3	0.05	-	20000
Bearing plate (stiff element)	Plane stress	200000	-	0.30	-	2816 (11x256)

Table D.2: Properties of the bearing plate interface element of the 2D model of half a span

Member	σ_y/u_y (normal) $[\mathrm{N/mm^3}]$	σ_x/u_x (shear) $[\mathrm{N/mm^3}]$	t $[\mathrm{mm}]$
Bearing plate interface	4.536	0.02941	2816 (11x256)

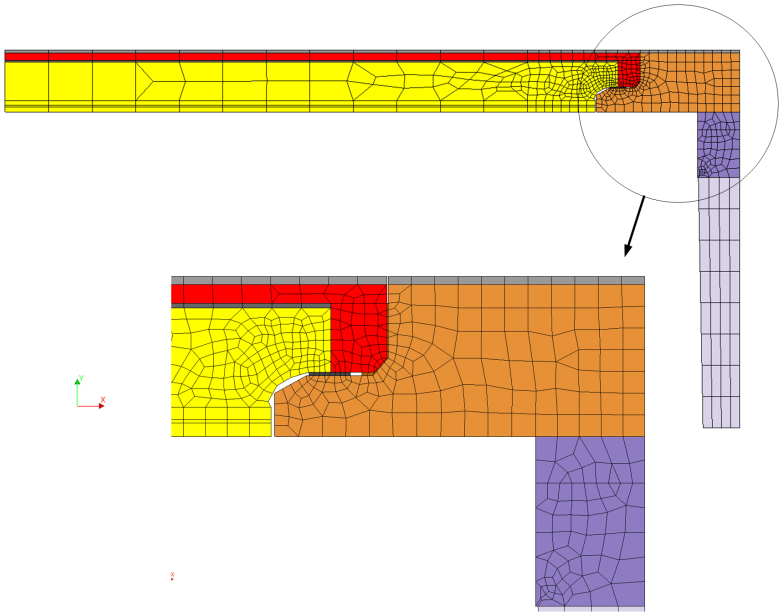

Figure D.3: Mesh of the 2D model of half a standard span

To facilitate the support of the columns through a rotational spring, a beam with high relative stiffness is located at the bottom of every column. This is further explained in Section D.2.3.

The dimensions of the components of the 2D model of the full bridge can be found in Figure D.5. As the model uses mainly elements with the same dimensions as the 2D model of half a standard span, the half-joint detail belonging to a standard span can be found in Figures D.2c and D.2b. The elements of the standard spans have the same properties as the elements of the 2D plane stress model of half a standard span, and can be found in Table D.1. The properties of the elements of the divergent span between support 3 and 4 can be found in Table D.3.

For simplicity, the bearing plates of the 2D model of the full bridge uses the same bearing plate stiffness as the 2D model of half a standard span. The properties of the interface elements of bearing plates are depicted in D.4.

D.2.2. Supports

To simulate the abutments of the bridge, the EPS elements at both ends of the bridge are constrained in x-direction, and the bottom edge of the corresponding bearing plate elements are constrained in both x- and y-direction.

The supports of the bridge are anchored using pile foundations. These pile foundations are considered to have high resistance against translation, but have finite stiffness against rotation. A design drawing of the foundation of a regular support is shown in Figure D.6.

The stiffness of the foundation can be estimated using a manual calculation based on the schematic in Figure D.7. The normal stiffness of a pile can be calculated using equation D.3.

$$K_{N,i} = \frac{EA}{L_i} \tag{D.3}$$

As a result of a rotation in the foundation plate $d\alpha$, the normal force in the foundation piles can be calculated using equation D.4.

$$F_i = K_{N,i} \cdot du_i = \frac{EA}{L_i} \cdot d\alpha \cdot e_i \tag{D.4}$$

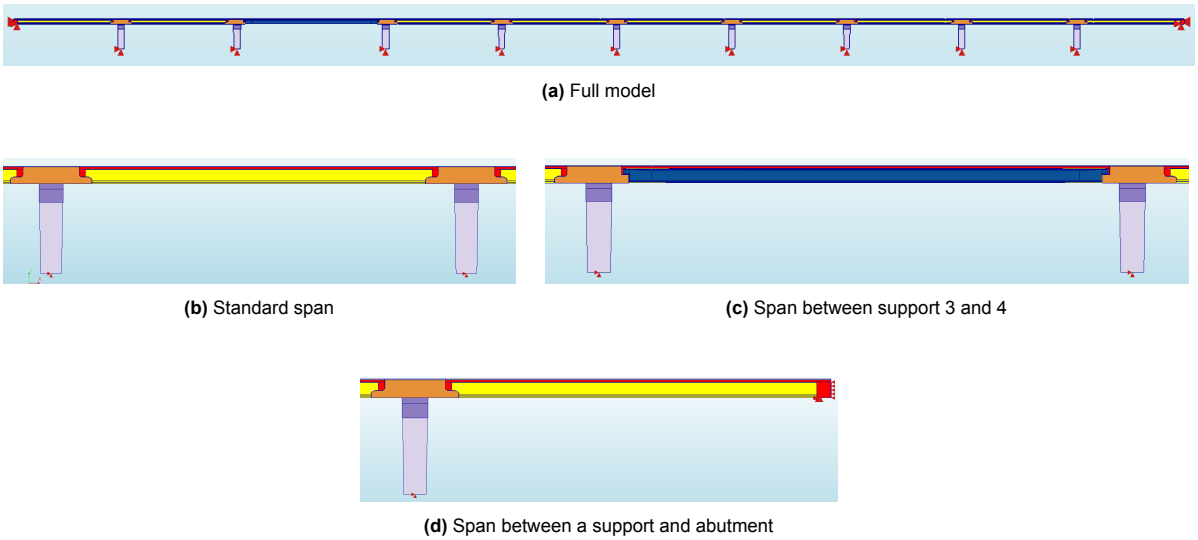

(a) Full model

(b) Standard span

(c) Span between support 3 and 4

(d) Span between a support and abutment

Figure D.4: 2D plane stress model of the full Naardertrekvaart bridge

Thus, the rotational stiffness of the support foundation can be calculated with equation D.5.

$$K_{rot} = \frac{M}{d\alpha} = \frac{\sum_i F_i \cdot e_i}{d\alpha} = EA \cdot \sum_i \frac{e_i^2}{L_i} \tag{D.5}$$

where:

$$E = 35000 \text{ N/mm}^2,$$
$$A = 400 \cdot 400 = 160000 \text{ mm}^2.$$

The longest foundation pile has a length of 12.5m. The resulting minimal rotational stiffness is equal to $5.91 \cdot 10^{13}$ Nmm/rad. This rotational stiffness is applied to the structure in the middle of the column support beam, in combination with a constraint of displacement in both x- and y-direction.

D.2.3. Mesh

The mesh of the first 2.5 spans of the model contains all information about the mesh of the complete model, containing a span connecting to the abutment, a standard span, and a divergent span. The remaining portion of the bridge is meshed using the same mesh settings, which are the same settings described in Section D.1.3. The mesh of the first 2.5 spans is shown in Figure D.8. The model uses a finer mesh at locations near connections between elements and a coarser mesh where the structure is expected to behave undisturbed.

D.3. 3D Solid Element Model of One Support

To investigate the behaviour of the support in both the transversal and longitudinal directions, a 3D model of a single support is developed. The model is shown in Figure D.9. Section D.3.1 describes the geometrical components of the model, Section D.3.2 describes the supports of the model, and Section D.3.3 describes the mesh of the model.

D.3.1. Geometrical Components

The dimensions of the 3D model of one support are based on the same design drawing of support 6 on which the other models are based, which can be found in Appendix A. The model consists of a column, two transition elements, the platform, and a high-strength concrete layer. The dimensions of the elements can be found in Figure D.10. The shape of the platform element at the location of the half-joint is the same as in the previously developed models and can be found in Figure D.2c. The properties of the geometrical components can be found in Table D.5.

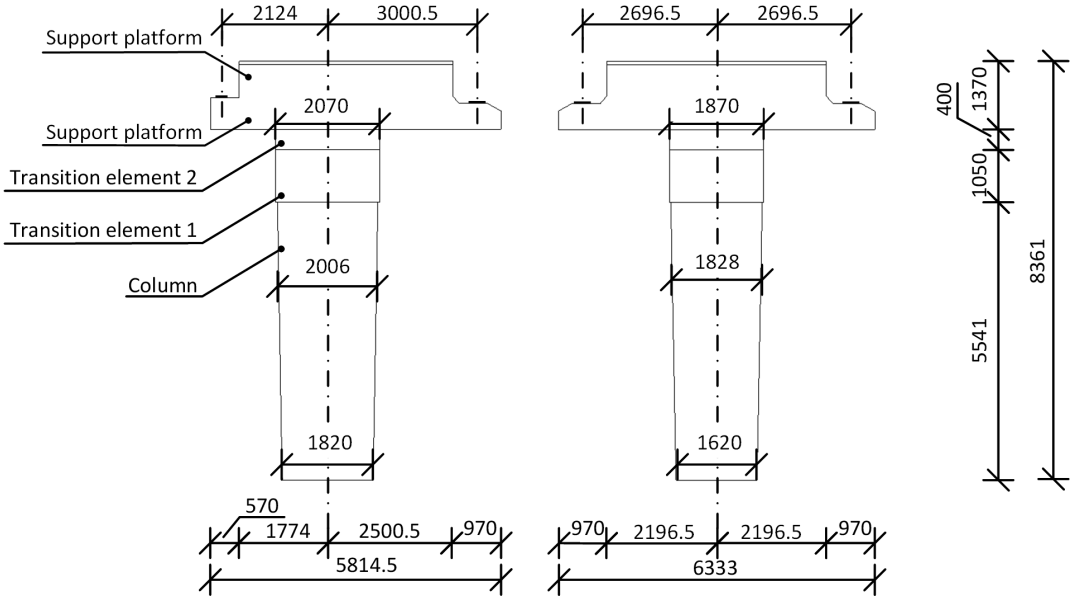

(a) Dimensions of the two column types of the model

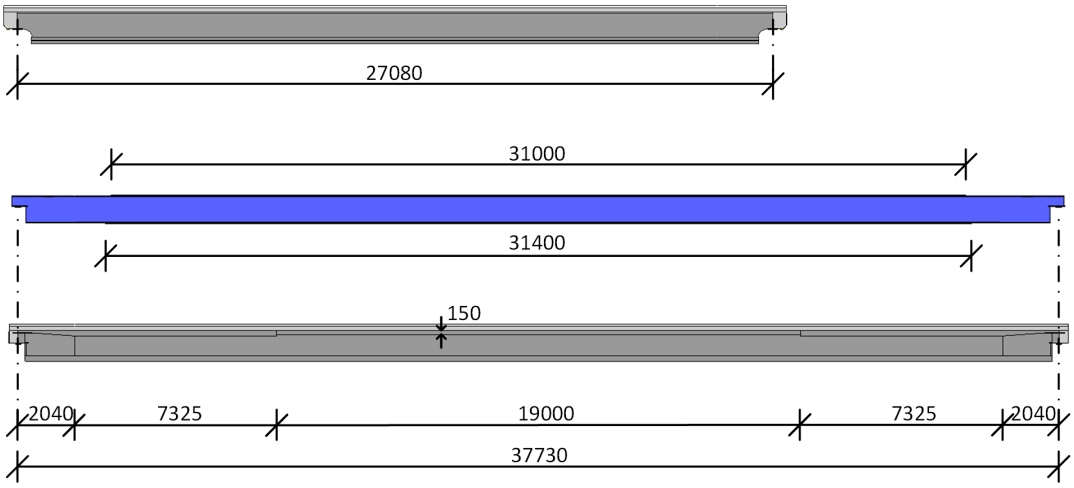

(b) Dimensions of the longitudinal girders of the model. From top to bottom: the HIP girder, the steel profile of the Preflex girder, and the concrete part of the Preflex girder.

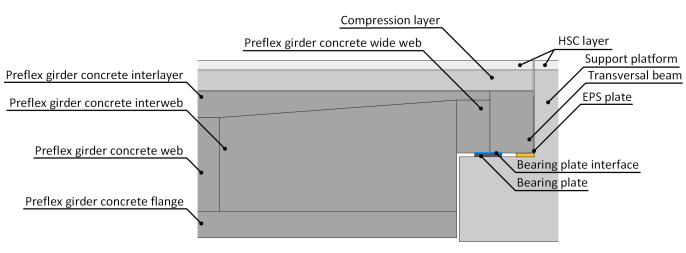

(c) Detail of a half-joint of a divergent span with component names

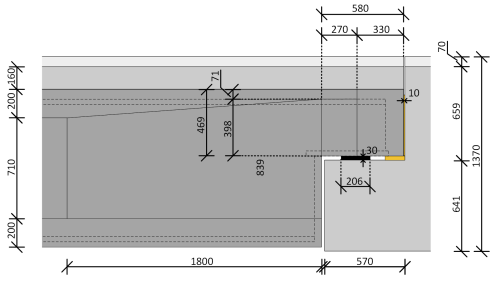

(d) Detail of a half-joint of a divergent span with dimensions. The internal HEB1000 is shown with a dotted line.

Figure D.5: Dimensions of the geometrical components of the 2D model of the full bridge

Table D.3: Element properties of the divergent span of the 2D model of the full bridge. E-modulus values have been extracted from [64].

Member	Type	E $[\mathrm{N/mm^2}]$	G $[\mathrm{N/mm^2}]$	ν [-]	α $[\mathrm{K^{-1}}]$	t $[\mathrm{mm}]$
Preflex girder concrete flange	Plane stress	34429	-	0.15	1e-5	13200 (11x1200)
Preflex girder concrete web	Plane stress	25788	-	0.15	1e-5	1991 (11x181)
Preflex girder concrete inter-layer	Plane stress	25788	-	0.15	1e-5	4009.5 (11x364.5)
Preflex girder concrete inter-web	Plane stress	25788	-	0.15	1e-5	4741 (11x431)
Preflex girder concrete wide web	Plane stress	25788	-	0.15	1e-5	7491 (11x681)
Preflex girder steel bottom welded plate	Plane stress	210000	-	0.3	1e-5	6050 (11x550)
Preflex girder steel lower flange	Plane stress	210000	-	0.3	1e-5	3300 (11x300)
Preflex girder steel web	Plane stress	210000	-	0.3	1e-5	209 (11x19)
Preflex girder steel upper flange	Plane stress	210000	-	0.3	1e-5	3300 (11x300)
Preflex girder steel top welded plate	Plane stress	210000	-	0.3	1e-5	6050 (11x550)
Preflex girder steel joint welded plate	Plane stress	210000	-	0.3	1e-5	6600 (11x600)
Compression layer	Plane stress	25788	-	0.15	1e-5	20000
HSC layer	Plane stress	37452	-	0.15	1e-5	20000
Transversal beam	Plane stress	25788	-	0.15	1e-5	20000
EPS plate	Plane stress	5.5	3	0.05	-	20000
Bearing plate (stiff element)	Plane stress	200000	-	0.30	-	6732 (22x306)
Column support beam	C-III beam	25788	-	0.15	1e-5	H=10000 W=10000

D.3.2. Supports

The bottom face of the support column is constrained in x-, y- and z-direction. No additional constraints are given to the model.

D.3.3. Mesh

The mesh of the 3D solid element model of one support is shown in Figure D.11. This mesh is achieved with the default mesher type of Diana 10.8 using a seeding method based on element size, with a desired size of $200\mathrm{mm}$ and a size transition smoothness of 0.15. While running the model, Diana gives seven warnings about elements at several locations in the support with internal angles less than 10 °. These small angles could cause inaccuracy in the finite element calculation. To ensure that these elements do not have a significant influence on the results of the calculation, a mesh sensitivity analysis is performed in Appendix E.2.

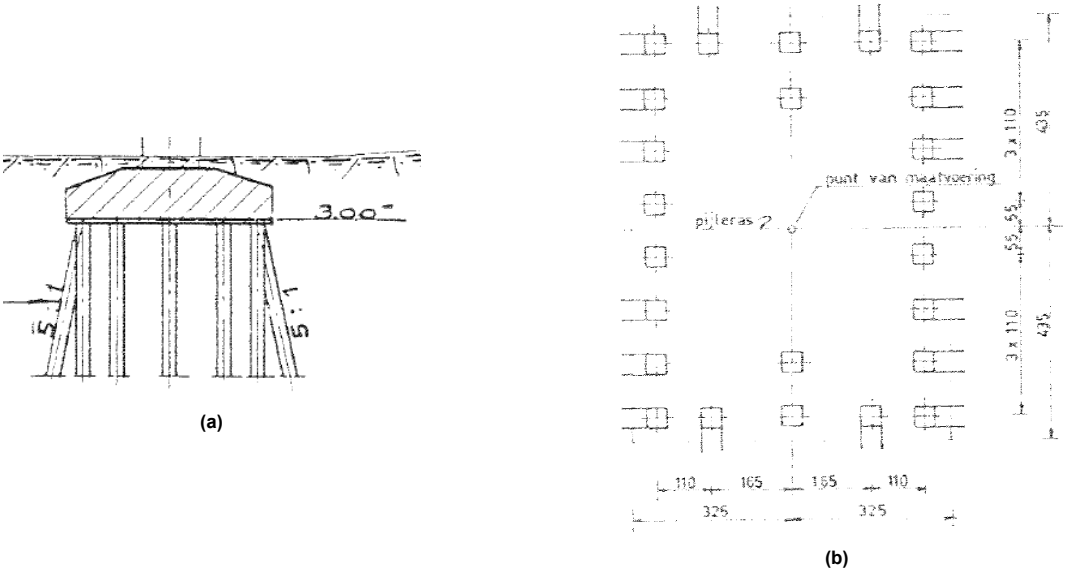

Figure D.6: Drawings of the foundation of a regular support

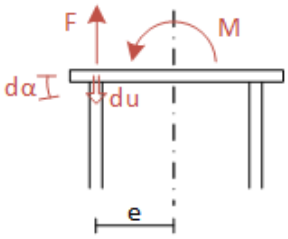

Figure D.7: Schematic of the calculation of the rotational stiffness of the support foundation

Table D.4: Properties of the bearing plate interface element of the 2D model of the full bridge

Member	σ_y/u_y (normal) [$\mathrm{N/mm^3}$]	σ_x/u_x (shear) [$\mathrm{N/mm^3}$]	t [mm]
Bearing plate interface standard span	4.536	0.02941	2816 (11x256)
Bearing plate interface divergent span	4.536	0.02941	6732 (22x306)

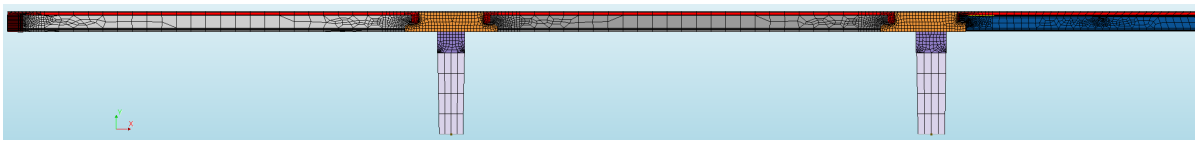

Figure D.8: Relevant portion of the mesh of the 2D model of the full bridge

Table D.5: Element properties of the 3D solid model of one support. E-modulus values have been extracted from [63].

Member	Type	E [$\mathrm{N/mm^2}$]	ν [-]
Column	Structural solid	25788	0.15
Transition element 1	Structural solid	25788	0.15
Transition element 2	Structural solid	25788	0.15
Support platform	Structural solid	25788	0.15
HSC layer	Structural solid	37452	0.15

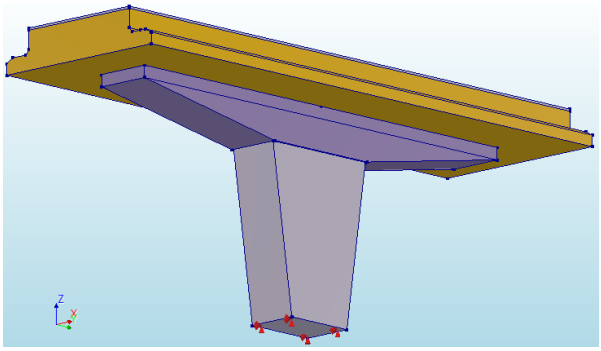

Figure D.9: 3D solid element model of one support

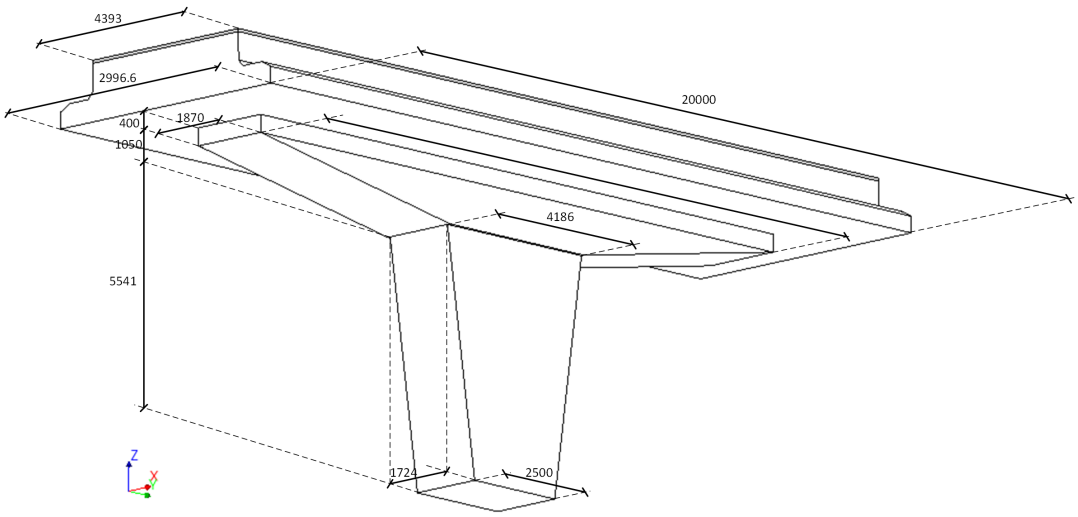

Figure D.10: Dimensions of the geometrical components of the 3D solid element model of one support

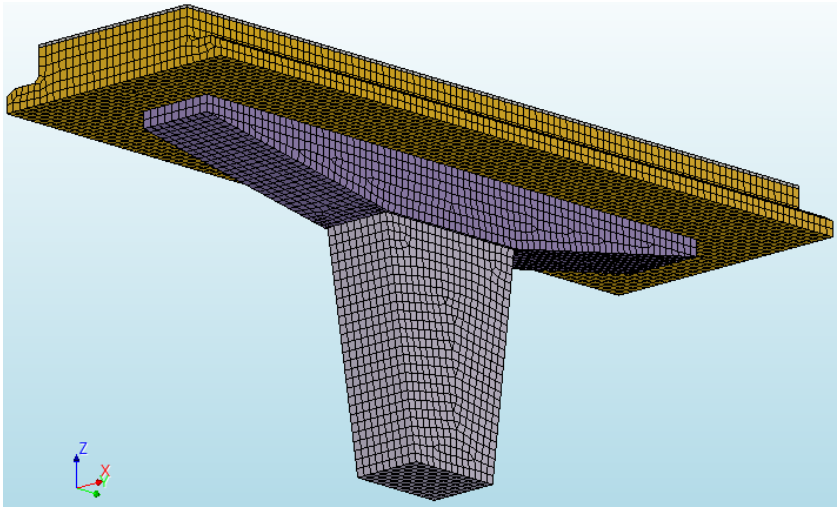

Figure D.11: Mesh of the 3D solid element model of one support

E

Verification of the Numerical Models

This chapter contains the verification of the numerical model. Based on manual calculations, the ability of the numerical models to simulate the physical behaviour of the bridge is confirmed. Section E.1 contains a verification of the behaviour of the support columns and the spans of the 2D plane stress models of the Naardertrekvaart bridge, and Section E.2 contains a verification of the mesh insensitivity of the 3D solid element model of the Naardertrekvaart bridge.

E.1. Verification of the 2D Plane Stress Models

The 2D models of the Naardertrekvaart bridge make use of elements with the same geometry. As a result, the verifications in this section hold for both of the models.

E.1.1. Verification of the Bending Stiffness of the Support Column

The bending stiffness of the support columns can be verified with a solid element model of the support. The horizontal displacement resulting from a horizontal distributed load is compared to that of the 2D plane stress model. The solid element model and its displacement resulting from a horizontal distributed load of 50000 N/m at the location of the centre line of the bearing plates is shown in Figure E.1.

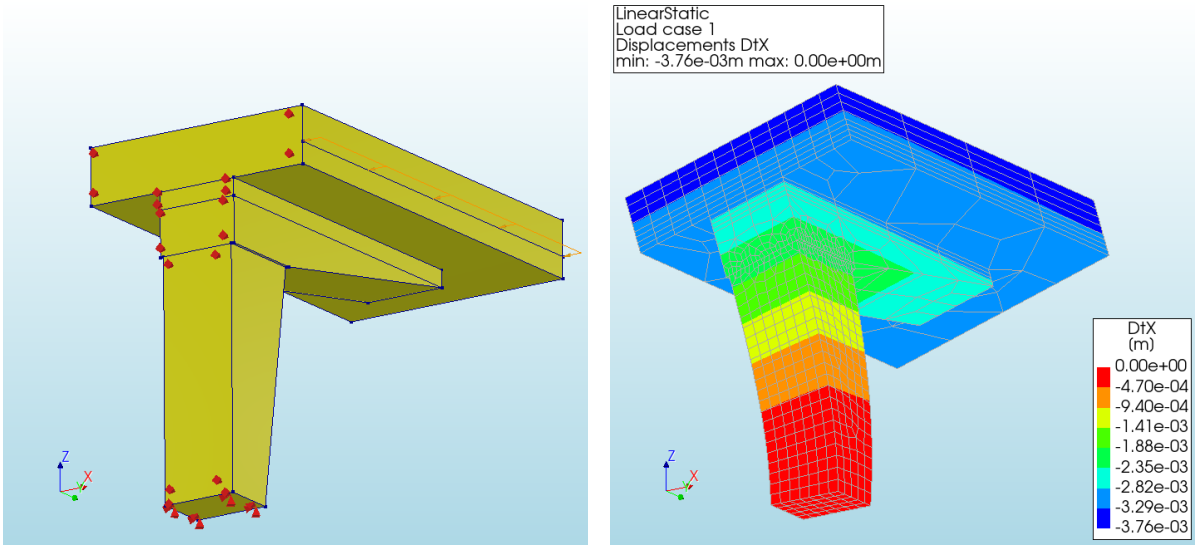

(a) Solid element model. The foundation support constrains the bottom face of the column in both x, y and z direction. The vertical face of the elements are constrained in y direction to simulate symmetry in the y-z plane.

(b) Result of the linear static analysis resulting from distributed load of $50,000\mathrm{N/m}$ exerted at the location of the bearing plates. The deformation scaling factor is equal to 500.

Figure E.1: Verification of the bending stiffness of the support columns

Table E.1: Comparison of Estimated EI_y Values of the Support Column

$u_{x,solidmodel}$	$u_{x,framemodel}$	Difference
$-4.93mm$	$-4.82mm$	2.2%

E.1.2. Verification of the Bending Stiffness of the Spans

The 2D plane stress models of the Naardertrekvaart bridge are composed of two types of spans. The behaviour of these spans can be verified by comparing a hand calculation of the bending stiffness of the span with the bending stiffness resulting from a numerical calculation of the response of a 2D plane stress model of the spans to a certain load. The bending stiffness can be estimated with Equation E.1.

$$EI = \sum_{i=1}^{n} E_i \cdot \left(\frac{1}{12} b_i h_i^3 + A_i d_i^2 \right) \tag{E.1}$$

The bending stiffness of the span in the models is obtained by exerting a vertical distributed load of $50000\mathrm{N/m}$ to the span, as depicted in Figure E.2a, and extracting its rotation around the y-axis φ_y at the location of the support. Following from the formula for φ from the forget-me-not depicted in Figure E.2b, the rotational stiffness EI_y can be calculated with equation E.3.

$$\varphi = \frac{1}{24} \frac{ql^3}{EI} \tag{E.2}$$

$$EI_y = \frac{1}{24} \frac{ql^3}{\varphi_y} \tag{E.3}$$

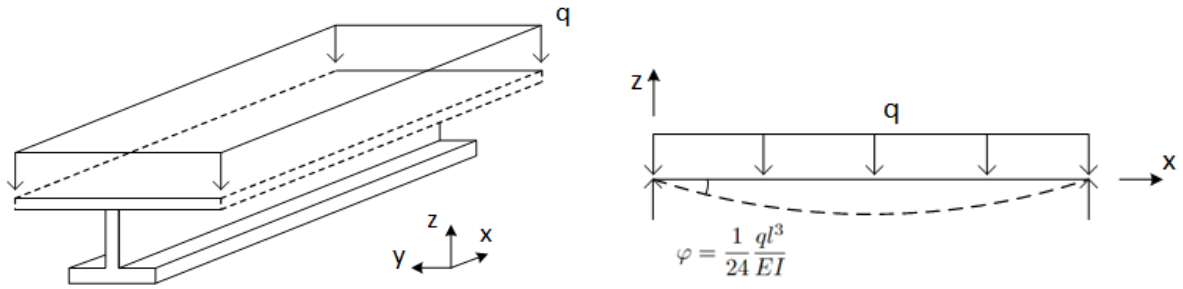

(a) Loading of the span **(b)** Forget-me-not

Figure E.2: Verification of the bending stiffness of the span

The comparison of bending stiffness according to the manual calculation and the numerical model can be found in Table E.2.

Table E.2: Comparison of Hand Calculated and Model Estimated EI_y Values of the Spans

	$EI_{y,hand}$	$EI_{y,model}$	Difference
Standard span	$7.328 \cdot 10^{15}\mathrm{N\,mm^2}$	$6.821 \cdot 10^{15}\mathrm{N\,mm^2}$	6.9%
Divergent span (3-4)	$9.811 \cdot 10^{15}\mathrm{N\,mm^2}$	$11.094 \cdot 10^{15}\mathrm{N\,mm^2}$	13%

E.2. Verification of the 3D solid element model of one support

To ensure that the results of the 3D solid element model of one support are insensitive to changes in mesh size, the mesh size reduced by 50% and the results are compared. The rotations on the bottom of the lower half-joint nib, below the bearing plates, due to a vertical load on the corresponding bearing plate are shown in Table E.3 for each mesh size. This concerns the rotation relative to the centre of the platform. The maximum difference in rotation between the two mesh sizes is equal to 4.0%, which is estimated to be sufficiently small for the investigations carried out with this model.

Table E.3: Comparison of the rotation results relative to the centre of the platform of the 3D solid element model for different sizes

Y-coordinate [m]	Rotations [mrad]		Difference
	$s = 200\text{mm}$	$s = 100\text{mm}$	
9.20	−0.0392	−0.0404	2.9%
7.36	−0.0290	−0.0297	2.5%
5.52	−0.0249	−0.0255	2.6%
3.68	−0.0217	−0.0226	4.0%
1.84	−0.0198	−0.0205	3.5%
0.00	−0.0188	−0.0195	3.8%
−1.84	−0.0198	−0.0204	3.3%
−3.68	−0.0219	−0.0226	3.3%
−5.52	−0.0251	−0.0255	1.9%
−7.36	−0.0291	−0.0295	1.4%
−9.20	−0.0392	−0.0403	2.8%
		Max	4.0%